The Gravity of Titan

Analysis of Cassini's Doppler Tracking Data and Solar Radiation Pressure

B. G. van Noort

Delft University of Technology

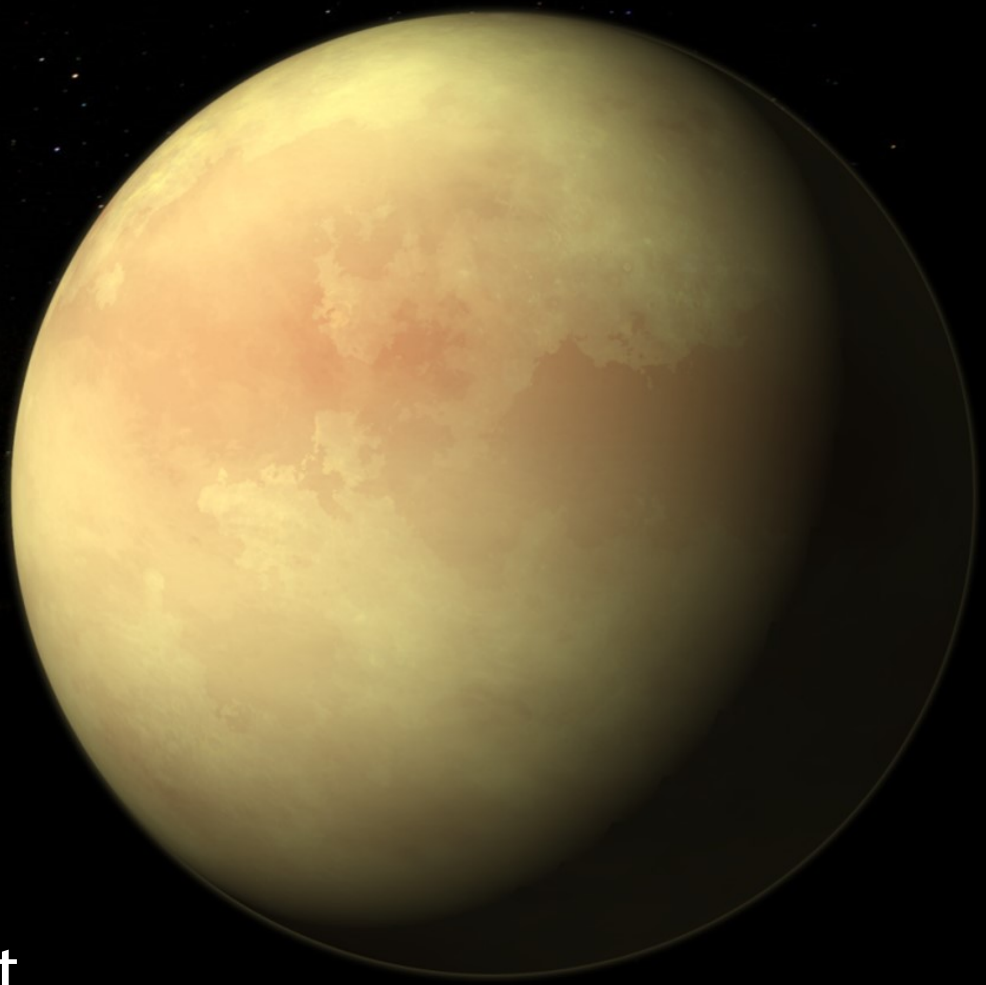

TU Delft

The Gravity of Titan

Analysis of Cassini's Doppler Tracking Data and Solar Radiation Pressure

by

B. G. van Noort

to obtain the degree of Master of Science
at the Delft University of Technology,
to be defended publicly on 26 January 2021.

Student number:	4363973	
Thesis committee:	Prof. dr. ir. P.N.A.M. Visser	TU Delft, committee chair
	Dr. ir. W. van der Wal	TU Delft, thesis supervisor
	Dr. ir. S.J. Goossens	NASA GSFC, internship supervisor
	Dr. P.G. Ditmar	TU Delft

This report is confidential and cannot be made public until 1 July 2021

TU Delft Delft University of Technology

Preface

This study provides an in-depth analysis of the obtained Doppler tracking data from the Cassini-Huygens mission during several Titan flybys. My master studies, and hence my study at the University of Technology Delft as an Aerospace Engineering student in general, has come to an end.

This work is a continuation of the work performed during an internship at NASA Goddard Spaceflight Center, spanning a total of more than a year. Let me start by thanking Wouter van der Wal, Sander Goossens and Erwan Mazarico for giving me the great opportunity to follow an internship at NASA. Besides having gained a tremendous amount of knowledge, it was an incredibly nice and fun experience, where I have met many great new people, tasted the culture of the United States, and seen the theory on planetary sciences put into practice. Without this internship, I would not have this incredibly interesting topic of analysing Doppler tracking data of one of the most prestigious missions in the history of spaceflight so far. Due to the COVID-19 virus, I had to leave the United States earlier than I planned, resulting in cancellation of a vacation I had planned after the internship. The COVID-19 epidemic occasionally made it difficult to find motivation to work on a thesis, especially since there was no possibility to study at the university together with colleague students. Fortunately, weekly gaming sessions with friends from the TU Delft made up for that.

Furthermore, I would like to thank my thesis supervisor Wouter van der Wal and my internship supervisor Sander Goossens for all their support and answering any questions I had during this project. A special thanks goes to Sander Goossens, who has helped me substantially trying to get GEODYN II up and running at the TU Delft, and answering any questions I had on GEODYN II with its occasionally weird errors messages. Anyone with the experience of using GEODYN II can probably acknowledge these frustrations. In addition, I would like to thank Pieter Visser for answering additional GEODYN II related questions, as well as providing analysis tools regarding GEODYN II output, which saved me the time of having to develop those. Subsequently, I want to thank the rest of the people that supported me during this thesis ranging from my parents and friends. A special thanks goes out to my lovely girlfriend Leonie, who always supported me when I was under stress or upset due to any temporary disappointing results.

B. G. van Noort
Delft, January 12, 2021

List of Figures

Abstract

Due to its compelling structure, Saturn's largest moon, Titan, has been of increasing interest. Titan belongs to the subclass of icy moons, and has been found to have a sub-surface water ocean present. Planetary scientists believe that the sub-surface ocean of Titan has been or could be a habitable environment for extra-terrestrial life. Knowledge on the gravity field and tides of Titan yields valuable information on the interior structure and formation of Titan, which aids in determining whether this sub-surface ocean could be habitable for extra-terrestrial life. Cassini had many flybys of Titan; but only a few were dedicated to gravity (i.e. radio tracking). Only one analysis of Titan's gravity field and tides has been performed, with ten flybys containing Doppler tracking data at closest approach included in this analysis. Given that the gravity and tidal Love number k_2 can be used for determining the density of the ocean, and thus deduce a suitable chemical composition, an independent analysis of the gravity and tides of Titan is a relevant addition to the literature. In addition, the dynamic model from previous studies implemented a rough estimation of the solar radiation pressure force. Hence, the dynamic model can be improved by adopting a more accurate solar radiation pressure model.

Previous research estimated the tidal Love number, k_2, and spherical harmonic coefficients of Titan's gravity field up to degree five, with the application of global constraints and non-zero initial conditions on some gravity coefficients. Global constraints are constraints applied to the global parameters, such as the spherical harmonic coefficients, k_2 Love number, and gravitational parameter μ. This study estimates Titan's spherical harmonic expansion of the gravity field up to degree three without the application of global constraints. It is difficult to find a k_2 Love number for Titan with this methodology; significant correlation in the parameter set exists due to, among others, poor coverage and a lack of data, leading to the inability to determine certain parameters uniquely. In addition, we did not obtain a stable solution of the spherical harmonic gravity field up to degrees higher than three with our methodology of not implementing global constraints. These global constraints thus seem to be necessary to resolve correlations between (higher order) gravity coefficients and k_2. Nevertheless, we opt for a solution without application of these constraints as these constraints have a non-physical meaning and there exists no *a priori* information on a correct magnitude of these global constraints.

Nevertheless, the obtained 3x3 gravity field solution from this thesis shows similarities with the 5x5 gravity field solution of Titan from previous research. The estimated ratio of $J_2/C_{22} = 3.674 \pm 0.288$ is found here, being compatible with the theoretical ratio of 10/3 for a celestial body in hydrostatic equilibrium. This also verifies the results from previous research. Additionally, the moment of inertia factor is found to be 0.342 when using the Radau-Darwin relation, similar to the value of 0.341 from previous research. The important coefficient C_{22} was found to differ significantly however, which could be caused by not giving it a global constraint in this work.

The stability of the proposed 5x5 gravity field solution from previous research is investigated. The gravity field was initialised with the gravity coefficients from previous research. After convergence of the arc parameters, the global parameters are re-estimated. The adjustments to the global parameter set were well within the formal uncertainties for degree two and three, as well as the tidal Love number. This suggests a stable gravity field solution for the lower degrees and the tidal Love number k_2.

The solar radiation pressure model implemented in the dynamic force model from previous research lacks precision. Said research used a simple box-wing spacecraft model consisting of a maximum of 11 large panels. This work proposes a new solar radiation pressure model with a more detailed and accurate spacecraft panel model consisting of 1500 panels. Precision of the estimated solar radiation pressure force is expected to increase by at least 10% when adopting this model. Even though the solar radiation pressure can be modeled more accurately, the estimated empirical accelerations are orders of magnitudes larger. To demonstrate the effect of the solar radiation pressure model, these empirical accelerations first need to be reduced.

The implemented dynamic models from this thesis and the most recent previous study on Titan's gravity field are fundamentally different: this thesis implements and estimates empirical accelerations and observation biases, while the other study estimates Titan's trajectory instead. To better compare results with previous research, an identical dynamic model should be implemented. Even after adopting an identical dynamic force model though, it is still expected that global parameter constraints are necessary, due to high correlations between global parameters. The estimated empirical accelerations in the adopted dynamic model of this thesis were orders of magnitudes larger than other forces adopted in the dynamic model. As such, no feasible solutions were obtained without them. Remarkably, previous research does not mention the use of these empirical accelerations.

In essence, this study stresses the importance of global constraints on the estimation of Titan's gravity field and tidal Love number to resolve large correlations between global parameters. Furthermore, a stable solution of Titan's spherical harmonic gravity field up to degree three has been proposed, without constraining these global parameters.

Abbreviations

BOL	Begin of life
C/A	Closest approach
CoM	Center of Mass
DSN	Deep Space Network
EOL	End of life
GEODYN II	Orbit determination program developed and maintained at NASA Goddard Spaceflight Center
GRAM	Global Reference Atmosphere Model
GSFC	Goddard Spaceflight Center
HGA	High Gain Antenna
JPL	(NASA) Jet Propulsion Laboratory
LGA	Low Gain Antenna
MLI	Multi-layer insulation
MOI	Moment of Inertia
NAIF	Navigation and Ancillary Information Facility
PCA	Principal Component Analysis
RMS	Root mean square
RTG	Radioisotope Thermoelectric Generators
SRP	solar radiation pressure
SPICE	Toolkit to analyse and obtain observation geometry information regarding celestial bodies, produced by NASA NAIF
Txxx	Flyby number xxx of Titan

Contents

1 Introduction

After its 13 years of fascinating science experiments, the Cassini spacecraft last orbited Saturn in September 2017, before descending into its atmosphere. Titan, Saturn's largest moon, is a moon of high interest due to its fascinating features: besides belonging to the class of icy moons, it has a sub-surface water ocean beneath its surface [Baland et al., 2011, Rappaport et al., 2008], which is expected to be a habitable environment for extra-terrestrial life [Hendrix et al., 2019]. Titan has been encountered many times during this mission, with multiple objectives dedicated to studying the atmospheric chemistry, cloud physics, and performing flyby maneuvers for tracking data to infer Titan's interior structure [Buffington et al., 2008, Lebreton and Matson, 1992].

The discovery of detailed properties of this possibly habitable sub-surface ocean is enabled by radio tracking of the Cassini spacecraft during close encounters with Titan. These Doppler tracking measurements can be used for analyzing the gravity field of Titan, including its tidal Love number k_2 [Durante et al., 2019, Iess et al., 2010, 2012]. The k_2 Love number is a dimensionless number which relates the change in potential from a celestial body caused by tidal forces from another body (e.g. McCarthy et al. [2015]). This number, as well as gravitational parameters, impose constraints on the interior structure of Titan (e.g. Durante et al. [2019], Sohl et al. [2003]). This allows determination of likely interior models, consisting of several interior layers, predicting the measurements. This led to the conclusion of an existing sub-surface ocean on Titan (e.g. [Iess et al., 2012]), but could also lead to interesting conclusions on the rest of Titan's interior in the future, such as the chemical composition of its sub-surface ocean, which is necessary to evaluate the habitability of this ocean [Hendrix et al., 2019, Raulin and Owen, 2003].

A total of ten Titan flybys contained Doppler tracking data suitable for gravity determination of this moon. Recent studies found a solution of the spherical harmonic expansion of the gravity field up to degree three and five, both with and without tidal Love number k_2 [Durante et al., 2019, Iess et al., 2010, 2012]. A discrepancy exists between these three papers regarding the J_3 zonal coefficient of the gravity field, with the most recent estimation having a formal error larger than its magnitude. Additionally, Anderson and Schubert [2013] did an estimation of Titan's gravity field with Doppler data from six available flybys at the time, but this did not result in a (realistic) k_2 value. Given the importance of an accurate estimation of the gravity field and tides of Titan, obtaining an independent solution of these parameters is extremely valuable, especially since limited data are available to validate the obtained results. Furthermore, previous research applies constraints to all parameters, including the spherical harmonic coefficients as well as the tidal Love number [Durante et al., 2019, Iess et al., 2012]. There exists no available *a priori* information on the gravity field of Titan that would justify applying physical constraints to certain global parameters. These constraints could thus have a significant effect on the solution of the gravity field and tidal Love number k_2 of Titan, though it is claimed that these constraints do not influence (i.e. constrain) the estimate by Durante et al. [2019]. The effect of these applied global constraints is investigated by performing a gravity analysis without them. Lastly, previous research does not mention the use of empirical accelerations in their implemented dynamic force model for the orbit and gravity determination process. We determine whether it is necessary to include these empirical accelerations for the dynamic force model implemented in this gravity analysis.

This work analyses the same X-band Doppler tracking data as Durante et al. [2019] while implementing a different dynamic force model parameterization and applying different analyzing strategies. Our dynamic model contains an improvement with respect to recent previous research, as it models the gravitational attraction of the Saturnian A, B, and C rings. We estimate Titan's spherical harmonic gravity field up to degree and order three

without the application of any global constraints thereby answering the following research questions:

What are the coefficients of the spherical harmonic expansion of the gravity field of Titan up to degree and order three (1σ)?
What is the influence of the applied global constraints on the estimated spherical harmonic gravity coefficients and tidal Love number k_2?

To answer these questions, we performed an independent analysis of Cassini Doppler tracking data, using a different orbit determination program (GEODYN II) which is designed and maintained at the NASA Goddard Spaceflight Center (GSFC). This study initially started as an internship at NASA GSFC, and has been further pursued in this work.

To further improve the quality of the estimated gravity field, a new Cassini solar radiation pressure (SRP) model will be developed. After this, the model will be implemented in the dynamic model of the Cassini spacecraft in the orbit determination software. In previous research, a simple box-wing spacecraft panel model has been adopted, roughly approximating the actual solar radiation pressure force on the spacecraft [Iess et al., 2010]. This thesis adopts a detailed spacecraft model where the SRP model calculates the SRP force on every panel of the spacecraft. This developed SRP model therefore estimates the SRP better than previous research. Hence, adding the detailed spacecraft panel model to the dynamic model of the Cassini satellite, could improve the estimate of the gravity of Titan.

The structure of this thesis is as follows. The main results in this thesis are described in the form of a draft scientific article with the independent estimation of Titan's gravity field, which can be found in Chapter 2. The article significantly adds to the knowledge by investigating the stability of the proposed solution of the gravity field [Durante et al., 2019], having implemented a considerably different dynamic model. The supplementary materials belonging to the article can be found in Chapter 3. Chapter 4 gives insight into said dynamic model by performing a sensitivity analysis to determine the parameters which influence the final least squares solution the most. A small change in these dominant parameters results in a large adjustment of the solution. This analysis was utilized to select appropriate constraints on the parameters. The methodology of our SRP model is explained and verified in Chapter 5, together with its promising results. This work utilizes a handful of programs, several of which were needed to be adapted to the planetary system of Saturn. The TU Delft uses an older version of GEODYN II compared to the version used at NASA GSFC, which led to small adjustments to the program. Hence the main GEODYN II program first had to be installed and verified. The several modifications to the GEODYN II program are discussed in the verification and validation Chapter 6, along with other utilized and modified programs. Finally, conclusions drawn from this research as well as recommendations for further research are proposed in Chapter 7. To assure a smooth transition for future research, Appendix A lists all utilized programs for the entire analysis of Titan's gravity properties, including extensive descriptions.

Background

The main focus of this thesis is to determine an independent solution of the gravity field of Titan. Analyzing radio tracking data of any kind from a satellite allows the determination of the orbit trajectory of the satellite. To determine said trajectory, a dynamic force model should be made with which the trajectory of the satellite can be integrated given an initial condition. Subsequently, the obtained radio tracking data will be compared to the computed trajectory during this orbit integration from an observation model. If the computed radio tracking data are consistent (to the noise level) with the obtained radio tracking data, the orbit trajectory has converged to an optimum solution. During this process, several parameters can be estimated, if they are included in the dynamic force model (for forces) or observation models. This includes the estimation of spherical harmonic coefficients of the gravity field and tidal Love number k_2. The process of estimating these parameters will be explained briefly hereafter. For a further, more detailed explanation, see Tapley et al. [2004] for example, or the GEODYN II documentation [McCarthy et al., 2015].

Equations of Motion

The spacecraft's equations of motion in an inertial, rectangular coordinate frame can be set up as follows [Tapley et al., 2004]:

$$\ddot{\mathbf{r}} = -\frac{\mu \mathbf{r}}{r^3} + \mathbf{a}' \tag{1.1}$$

where $\mathbf{r}$ is the position vector of the satellite with respect to the main body, μ is the gravitational parameter of the body around which the satellite is orbiting, $\ddot{\mathbf{r}}$ is the second derivative of the position with respect to time, and $\mathbf{a}'$ are the accelerations on the satellite caused by other effects. The other effects include, but are not limited to, solar radiation pressure force, atmospheric drag or gravity forces from other celestial bodies or objects. Notice that the first term is merely the gravity contribution of the main body as a point mass.

Conservative forces, such as the gravity field and tidal effects of perturbing bodies (Saturn in the case of Titan), can be expressed in terms of a potential function. The derivative of the potential with respect to the spatial coordinates then results in the acceleration (force) on the spacecraft. Hence, the above equation is usually expressed as [Tapley et al., 2004]:

$$\ddot{\mathbf{r}} = \nabla U + \mathbf{a} \tag{1.2}$$

where U is the sum of all potentials from conservative forces. Notice that $\mathbf{a}$ in this case is different from $\mathbf{a}'$ in Equation 1.1, as $\mathbf{a}$ no longer contains any accelerations due to conservative forces. In the analysis, the tidal and gravitational potentials are considered. After all, they have to be considered if we want to estimate the corresponding tidal Love number k_2 and several of the spherical harmonic gravity coefficients.

The gravitational potential of Titan is expressed in spherical harmonic coefficients as:

$$U(r,\theta,\phi) = -\frac{\mu}{r}\left[1 - \sum_{l=2}^{\infty} J_l P_{l0}(\cos\theta)\left(\frac{R_t}{r}\right)^l - \sum_{l=2}^{\infty}\sum_{m=1}^{l} P_{lm}(\cos\theta)\left(\frac{R_t}{r}\right)^l (C_{lm}\cos m\phi + S_{lm}\sin m\phi)\right] \tag{1.3}$$

where r is the radius at which the potential is evaluated, θ, ϕ are co-latitude and longitude, l, m are the degree and order of the spherical harmonic expansion, R_t is the reference radius of Titan, μ is the gravitational parameter of Titan, P_{lm} are the associated Legendre polynomials, J_l are the zonal spherical harmonic coefficients, and C_{lm}, S_{lm} represent the sectoral and tesseral spherical harmonic coefficients. Note that this spherical harmonic expansion is an approximation of a function on a sphere (gravity), analogous to approximating a (one-dimensional) function using a Fourier series.

Titan's orbit around Saturn causes significant variations in the tidal field as a result of the eccentricity (e=0.03) [Iess et al., 2011]. Saturn is said to raise tides on Titan, similar to the tides raised on Earth by the Moon. The largest contribution of these tides on Titan is to the second degree of the tidal potential [Iess et al., 2011, Iess et al., 2012] as follows:

$$U_T(r) = \frac{k_2}{2}\frac{\mu_s}{R_s^3}\frac{R_t^5}{r^3}\left[3\left(\hat{\mathbf{R}}_s \cdot \hat{\mathbf{r}}\right) - 1\right] \tag{1.4}$$

where k_2 is the second degree Love number, μ_s is the gravitational potential of Saturn, R_s is the distance between Titan and Saturn, R_t is the mean radius of Titan, r is the position of the satellite, $\hat{\mathbf{R}}_s$ is the unit vector from Titan to Saturn, and $\hat{\mathbf{r}}$ is the unit vector from Titan to the satellite [McCarthy et al., 2015]. The tidal Love number is an indication of how much a celestial body (Titan) deforms under the (change of the) gravity force of a perturbing body (Saturn). The k_2 Love number is a dimensionless parameter that describes the ratio between perturbed and perturbing potentials when solid tides raised on one body by another body change the shape and gravity field of the perturbed body. Assuming that the interior model consists of several interior layers (ice-I shell, sub-surface ocean, mantle and metallic core) following a Maxwell rheology [Jara Orué, 2016, Sabadini and Vermeersen, 2016], these interior layers all respond differently to the applied tidal load. The different responses are induced by so-called normal modes. The interior layers respond in both an elastic and anelastic fashion, and the tidal Love number can hence be expressed as an elastic part and an anelastic part as follows:

$$k_2(t) = k_2^E + \sum_{k=1}^{K}\frac{Z_k}{s_k}\left(1 - \exp\left(-s_k t\right)\right) \tag{1.5}$$

where k_2^E is the elastic response of the interior layers to the second degree tidal Love number, K are the number of excited normal modes, Z_k are the amplitudes of the normal modes, s_k is the inverse of the Maxwell time ($1/\tau_M$), and t is the time. Note that the tidal Love number can hence be seen as a function of time. The elastic component of the tidal Love number is a summation of the elastic responses from the normal modes. The anelastic component (also called viscoelastic component) is a summation of the viscoelastic responses of the normal modes.

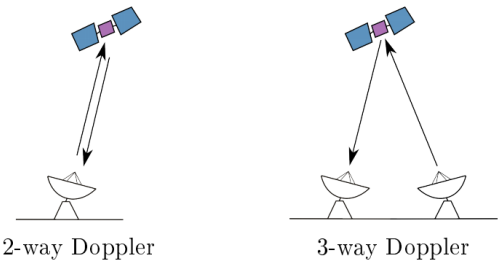

(a) Two-way and three-way Doppler measurements. [Pukhauser, 2015]

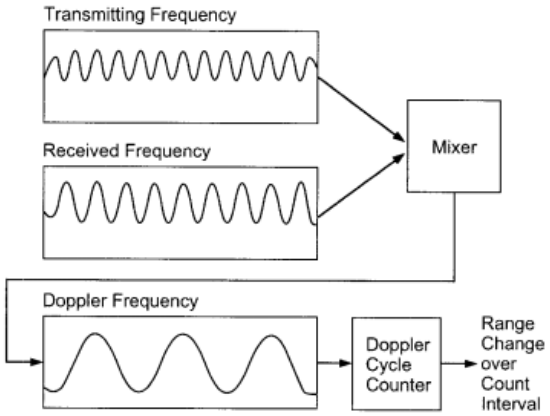

(b) The measurement process of the Doppler count. By subtracting the received frequency from the transmitted frequency, the Doppler frequency is obtained. By measuring the number of cycles of this signal over the count interval, the range change can be calculated. [Thornton and Border, 2003]

Figure 1.1: Illustrations of different types of Doppler data (a) and the radio tracking process for Doppler measurements (b).

The number of normal modes depends on the number of interior layers, as well as discontinuities in density and Maxwell relaxation times across layer boundaries [Jara Orué, 2016, Sabadini and Vermeersen, 2016]. For every discontinuity in one of these properties across layer boundaries, there is one additional normal mode [Jara Orué, 2016]. The Maxwell time τ_M is the ratio of the steady-state viscosity and rigidity of the interior layer. Interior layers with a low Maxwell time need less time to deform anelastically indicating a more fluid-like response. Layers with a high Maxwell time need more time to deform anelastically, which hence do not behave like a fluid on short timescales. From Equation 1.5 it is clear that the different interior layers contribute to the tidal Love numbers, and that their response depends on physical properties of the respective interior layers.

Observation equations

The estimation process combines the equations of motion as well as the observation equations. The observation equations relate the measured quantities to the position of the satellite. This work only analyses two-way and three-way Doppler tracking data. For two-way data, the Deep Space Network (DSN) ground stations transmit a signal (uplink) to the satellite at frequency f_T. The spacecraft receives a frequency f_R' different from f_T as it has shifted slightly due to the Doppler effect. The received signal is multiplied by a factor depending on which frequency band the uplink signal is in, and re-transmitted (downlink) to the same DSN ground station. This received signal frequency at the DSN stations is f_R. Three-way data are obtained when the received DSN station is a different station than the one transmitting the signal (see Figure 1.1a).

The received frequency is related to the range change and transmitted frequency as follows [Thornton and Border, 2003]:

$$f_R = \left(1 - \frac{2\dot{\rho}}{c}\right) f_T \tag{1.6}$$

where $\dot{\rho}$ is the change in range between the ground station and satellite and c is the speed of light. Note that the 2 in the equation comes from the fact that two-way (and three-way) Doppler measurements are used, where the signal has covered twice the distance between satellite and ground station.

The observable corresponding to the Doppler measurements is the Doppler count. The Doppler count is the difference between the number of cycles of the transmitted signal and the received signal measured over a certain count interval [Tapley et al., 2004, Thornton and Border, 2003]. The count interval in this work is 10 seconds. The Doppler count relates to the measured range rate as follows [Tapley et al., 2004]:

$$\frac{N}{\delta t} = \frac{2f_T}{c}\frac{\delta \rho}{\delta t} \tag{1.7}$$

where δt is the difference between two transmit times t_{T2} and t_{T1}, $\frac{\delta \rho}{\delta t}$ is the change in range over this count interval δt, and N is the Doppler count. The measured Doppler count can hence be directly related to the range rate by combining Equations 1.6 and 1.7. This extraction process is summarized in Figure 1.1b.

Estimation process

Both the equations of motion and the observation equations are non-linear. In order to determine the orbit determination parameters, these equations have to be linearized. The orbit determination parameters are all the parameters which we want to estimate, ranging from the spacecraft's position and velocity as well as the gravitational parameters. Linearization will take place at a reference state (i.e. initial conditions) of the to be determined final state. Notice that "state" here refers to the entire set of estimated parameters. Linearlization includes taking the derivative of Equation 1.1 with respect to the estimated parameters, yielding the variational equations. In addition, the derivatives of the observation equations (Equation 1.6) with respect to the estimated parameters have to calculated as well, which depend on the type of data used in the orbit determination analysis (see e.g. McCarthy et al. [2015]). In essence, these linearizations are Taylor expansions of the equations of motion and the observational equations [Tapley et al., 2004].

After linearization, the adjustment to the current reference state can be related to the residuals of the observations. These residuals are computed by taking the difference of the observed (measured) observations with the computed observations at the reference state:

$$y_i = Y_i - G(\mathbf{X}_i^*, t_i) \tag{1.8}$$

Here Y_i is the measured observation at time t_i and $G(\mathbf{X}_i^*, t_i)$ is the computed value of the observation at the reference state $\mathbf{X}_i^*$ [Tapley et al., 2004]. In Equation 1.8, y_i is called the observation residual and all these residuals from all different epochs t_i relate to the adjustments of the state as follows:

$$\mathbf{y} = B\mathbf{x}_k + \boldsymbol{\epsilon} \tag{1.9}$$

where $\mathbf{y}$ are all the observation residuals, B contains the derivatives of the observations with respect to the state parameters and is called the design matrix, $\mathbf{x}_k$ is the state adjustment at iteration k and $\boldsymbol{\epsilon}$ is the total error as a result of amongst others the linearization [Tapley et al., 2004]. A weighted least squares estimation will be used to estimate the necessary state adjustment $\mathbf{x}$, while minimizing the error $\boldsymbol{\epsilon}$. Common in the field of orbit determination is the application of an *a priori* covariance matrix for the estimated state adjustments, usually called a constraint matrix (e.g. Tapley et al. [2004]). The solution will be:

$$\hat{\mathbf{x}}_k = \left(B^T W B + \overline{W}_k\right)^{-1} \left(B^T W \mathbf{y} + \overline{W}_k \overline{\mathbf{x}}_k\right) \tag{1.10}$$

where $\hat{\mathbf{x}}_k$ is the estimate for the state adjustment, W the weight matrix of the observations, $\overline{W}_k$ is the *a priori* covariance matrix, and $\overline{\mathbf{x}}_k$ is the *a priori* condition of $\mathbf{x}_k$ [McCarthy et al., 2015, Tapley et al., 2004]. The term $B^T W B$ is called the normal matrix.

After having obtained $\bar{\mathbf{x}}_k$, the sum of the squares of the errors $\boldsymbol{\epsilon}$ are minimized for the given reference state. Yet, this is not the minimum error that can be achieved: by updating the reference state with the obtained state adjustment, and repeating the process, the error induced by the linearization process will decrease, given that the orbit determination problem with observations is stable (i.e. if no outliers are present). Therefore, the estimate of the state parameters will be obtained through an iterative weighted least squares approach. As noted, the equations of motions are linearized with a Taylor expansion. The least squares solution will converge to a solution if the ignored higher order terms do not have a significant impact.

The estimation process is divided into two parts: arc iteration and global iterations (Figure 1.2). Arc iterations involve the estimation of arc-specific parameters which only influence measurements from one arc (e.g. empirical accelerations, drag coefficients, position and velocity of the satellite), while global iterations solve for the arc parameters and global parameters. Global parameters are the parameters which influence the trajectory of the satellite of every flyby, such as the gravitational parameter μ, the spherical harmonic gravity coefficients, and the tidal Love number k_2. The orbit determination program GEODYN II will be used to perform the arc iterations, meaning it applies Equation 1.10, while keeping all the global parameters equal to a fixed value. The solutions are obtained separately for every arc, as the observations from a specific arc only influence the arc parameters from that particular arc. GEODYN II is software developed and maintained at NASA GSFC written in Fortran IV [McCarthy et al., 2015]. It has been used in the orbit determination of several satellites and gravity field estimations of numerous celestial bodies (e.g. MESSENGER orbiting Mercury [Mazarico et al., 2014], Mars Odyssey orbiting Mars [Mazarico, 2004], and Clementine orbiting the Moon [Lemoine et al., 1997]). Since GEODYN II has been used countless times, it is indirectly verified multiple times.

Afterwards, a separate program is used to perform global iterations. The global iterations are a multi-arc weighted least squares solution, meaning that all the arc-specific matrices are combined into one large matrix:

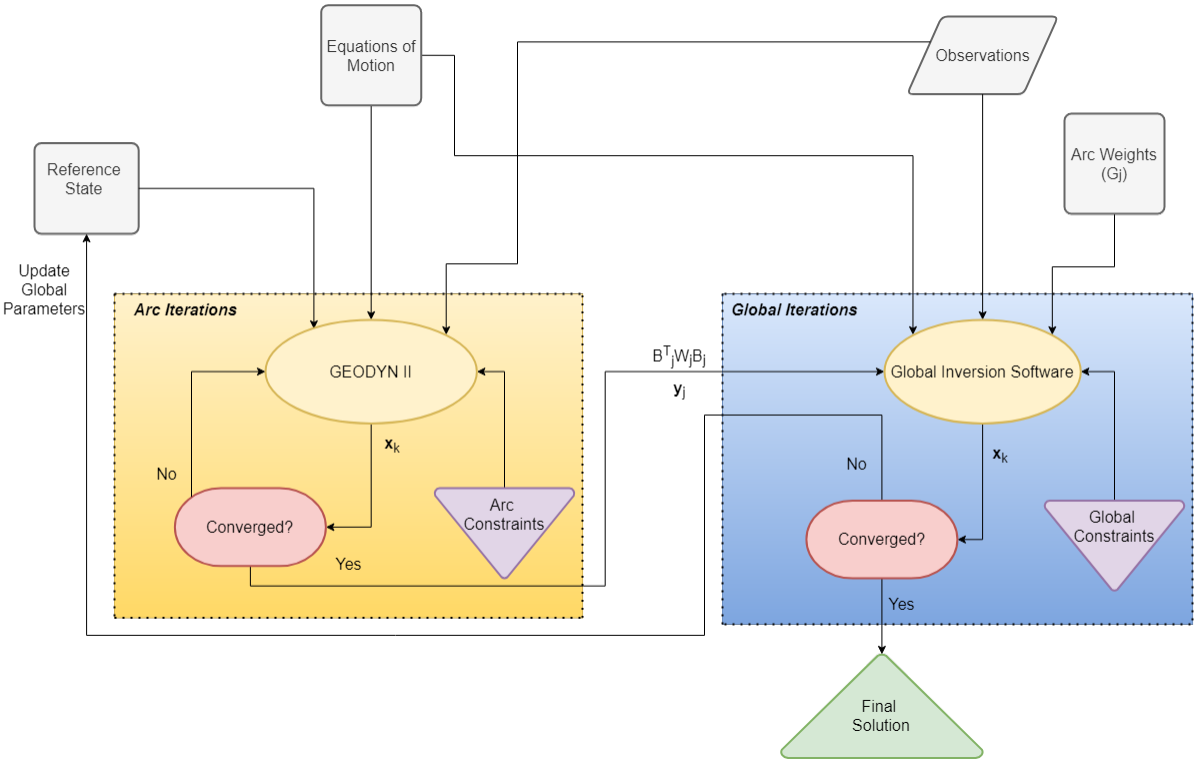

Figure 1.2: Summary of the orbit determination process split up into arc and global iterations. Notice that $\mathbf{x}_k$ in this figure is the estimate of the state at iteration k, equivalent to $\bar{\mathbf{x}}_k$ in Equation 1.10.

$$N_{tot} = \sum_{j}^{n_{arc}} G_j \cdot B_j^T W_j B_j \tag{1.11}$$

$$\mathbf{Y}_{tot} = \sum_{j}^{n_{arc}} G_j \cdot B_j^T W_j \mathbf{y}_j \tag{1.12}$$

where N_{tot} is the combined normal matrix, n_{arc} is the total number of arcs, and G_j is the weight of arc j which is based on the coverage of every flyby, further explained in the article and the supplementary materials (Chapters 2 and 3). $\mathbf{Y}_{tot}$ is the combined residual vector and $\mathbf{y}_j$ is the residual vector of arc j. The constraint matrix is added to the combined normal matrix with weight unity as follows:

$$\left(N_{tot} + \overline{W}_k\right)\hat{\mathbf{x}}_k = \mathbf{Y}_{tot} \tag{1.13}$$

The global iterations are performed by solving for $\hat{\mathbf{x}}_k$ in Equation 1.13, similar to Equation 1.10. Note that the term $\overline{W}_k\bar{\mathbf{x}}_k$ is absent in Equation 1.13. In Chapter 6, it is explained in detail why this term is chosen to be absent. The method of applying arc weights and its justification is explained in Chapter 6 as well. The entire process of arc and global iterations is repeated until the global parameters have converged. Convergence is reached if large, global spherical harmonic coefficients (most degree two spherical harmonic coefficients) do not change by more than 1.0%. The orbit and gravity determination process is summarized in Figure 1.2.

The formal errors on the estimated parameters are calculated as follows:

$$P = \left(N_{tot} + \overline{W}_k\right)^{-1} = \left(\sum_{j}^{n_{arc}} G_j \cdot B_j^T W_j B_j + \overline{W}_k\right)^{-1} \tag{1.14}$$

with the formal error being $\sigma_l = \sqrt{P_{ll}}$. These formal errors are important as they indicate the certainty of the estimated value for a certain parameter.

Lastly, in the field of gravity determination, it is common to apply a Kaula constraint on the gravity coefficients [Kaula, 1966]. This is a totally empirical constraint, verified for the Earth by the use of gravimeters. It is a

strong constraint, as physically it is not possible to know the underlying *a priori* power distribution of the gravity coefficients, but it makes sense intuitively: large features (mass anomalies) in the gravity field usually have a larger power than small features [Mazarico, 2004]. The power (σ) of spherical harmonic degree l by the Kaula rule is:

$$\sigma_l = \frac{K}{l^2} \tag{1.15}$$

where K is called the Kaula factor, equal to 10^{-5} for Earth [Kaula, 1966]. Notice that this power (σ_l) contributes to the constraint matrix ($\overline{W}_k$) by adding $1/\sigma_l^2$ to the diagonals belonging to the spherical harmonic coefficients of degree l. The Kaula rule is usually applied if a large expansion of the gravity field is estimated, or to resolve large correlations between global parameters (due to e.g. poor surface gravity sampling). The value of $K = 10^{-5}$ is valid for Earth, and several scaling factors have been introduced to determine a Kaula factor for other celestial bodies (e.g. [McMahon et al., 2015]). Yet, it remains difficult to determine the right factor K for an icy moon such as Titan, as no verified value of this factor has been obtained for an icy moon yet. In this research, a Kaula constraint is not applied to come up with the results from Chapter 2. However, several solutions have been attempted with said constraint by implementing the power distribution of Titan's gravity coefficients from previous research [Durante et al., 2019]. A more thorough analysis of the Kaula constraint and its application can be found in Chapter 6.

2

Scientific Article

Titan's gravity field from Cassini Doppler Tracking Data

B.G. van Noort[1], et al.[1,2]

[1]Faculty of Aerospace Engineering, University of Technology Delft, the Netherlands
[2]NASA Goddard Space Flight Center, Greenbelt, Maryland, USA

Key Points:

- The spherical harmonic expansion of Titans gravity field can be determined up to degree and order three without applying global constraints on all gravity parameters.
- Constraints on the global parameters seem to affect the estimate on the tidal Love number k_2.
- We found a ratio of J_2/C_{22} of 3.674 ± 0.288 conform the ratio of a body in hydrostatic equilibrium.

Corresponding author: Bob van Noort, bobvannoort@hotmail.com

Abstract

The possibility of a habitable liquid water ocean existing on Titan can be further investigated by determining Titan's gravity field. We perform a stability analysis on the gravity field from previous research. After one global iteration, we find a stable solution insignificantly different from previous research for spherical harmonic degrees two and three, and the k_2 Love number. Additionally, we estimate Titan's gravity field to third degree and order in spherical harmonics using ten flybys from the Cassini mission, through a multi-arc weighted least squares approach. For our estimated gravity field, we find significantly higher uncertainties on the parameters compared to previous research. J_2 and J_3 differ insignificantly with previous research, though significant differences exist for the harmonic gravity parameter C_{22}, from which hydrostatic equilibrium is inferred. The observed ratio of J_2/C_{22} conforms with a theoretical value of 10/3 for a body in hydrostatic equilibrium and does conform with previous research. When applying a theoretically suitable dynamic force model, we do not find a stable solution for the gravity field and tidal Love number by applying appropriate constraints. The discrepancy between C_{22} and the ability to determine k_2 arises from the fact that our problem setup yields significant correlations between gravity and tidal parameters. Additionally, no constraints on global parameters are applied, and a different processing order is adopted compared to previous research.

1 Introduction

Titan, Saturn's largest moon, has long been of interest due to its icy surface, which may cover liquid water oceans habitable by extra-terrestrial life (Hendrix et al., 2019). Determining the interior structure of Titan is valuable to infer properties of said subsurface water ocean. Information on the gravity field and tides of Titan aids in determining likely interior structures of Titan, as its interior should comply with the measured gravity. In addition, the structure can support conclusions on its history and formation.

In September 2017 the Cassini spacecraft descended into Saturn's atmosphere to burn up. This ended a twenty year mission that yielded tremendous amount of data and insights on the Saturnian system. The gravity of Titan is estimated through determining the orbit of Cassini, utilizing Doppler radio tracking data. Previous research determined Titan's gravity field similarly (Table 1), where this paper independently analyzes equivalent data by applying a different dynamic force model and processing strategies.

The Doppler measurements will be used to estimate the spherical harmonic expansion of the gravity field as well as the potential Love number k_2. The k_2 Love number is a dimensionless number indicating how much a celestial body deforms as a result of a tidal attraction induced by another celestial body. It is thus an indication of how deformable its interior is.

The gravitational potential of a celestial body can be expressed in a spherical harmonic expansion:

$$U(r,\theta,\phi) = -\frac{\mu}{r}\left[1 - \sum_{l=2}^{\infty} J_l P_{l0}(\cos\theta)\left(\frac{R_{ref}}{r}\right)^l\right] + \frac{\mu}{r}\left[\sum_{l=2}^{\infty}\sum_{m=1}^{l} P_{lm}(\cos\theta)\left(\frac{R_{ref}}{r}\right)^l (C_{lm}\cos m\phi + S_{lm}\sin m\phi)\right] \tag{1}$$

where l, m are the degree and order of the expansion, and r, θ, and ϕ, are the radius, colatitude, and longitude, respectively, at which the gravitational potential is calculated. R_{ref} is a reference radius (taken to be 2575 km for Titan), μ is the gravitational parameter of Titan, J_l are the zonal spherical harmonic coefficients, C_{lm}, S_{lm} are unnormalized spherical harmonic coefficients (see e.g. Murray and Dermott (1999)). Since sin(0) = 0, all the coefficients S_{lm} are zero and all coefficients of degree one are zero, as the potential function is defined to be about the center of mass of the main body.

The k_2 Love number is a dimensionless parameter that describes the ratio between perturbed and perturbing potentials when solid tides raised on one body by another body change the shape and gravity field of the perturbed body. It is the dominant term in the expansion of the tidal potential, similar to that of the main body potential, with the tidal potential being equal to:

$$U_T(r) = \frac{k_2}{2}\frac{\mu_{sat}}{R_{sat}^3}\frac{R_{ref}^5}{r^3}\left[3\left(\hat{R}_{sat}\cdot\hat{r}\right) - 1\right] \tag{2}$$

where R_{sat} is the distance between the centers of mass of Saturn and Titan, μ_{sat} is the gravitational parameter of Saturn, k_2 is Titans second degree Love number, r is the distance from the point at which we want to know the potential to Titan's center of mass, $\hat{r}$ is the unit vector pointing from the center of Titan to the point at which the potential needs to be known, and $\hat{R}_{sat}$ is the unit vector pointing from Titan to the position

of Saturn (McCarthy et al., 2015). Including this tidal potential in the dynamic model of forces acting on the satellite, this potential Love number k_2 can be estimated.

Table 1 briefly summarizes previous research on Titan's gravity field and tidal Love number k_2. The amount of data used in the analyses differs per research work, as not all data from flyby manoeuvres was available at the time of research. In addition, all papers use Doppler tracking data. Note that previous research does not apply a Kaula constraint on the global gravity coefficients (Kaula, 1966). The most important parameters of the gravity field are J_2, C_{22}, J_3, and k_2 (the J_l coefficients are defined as $-C_{l0}$), as these parameters constrain the interior structure, composition and moment of inertia (MOI) of Titan. The normalized MOI factor $\overline{\mathcal{C}}/(mR^2)$ is the mean MOI ($\overline{\mathcal{C}}$) of Titan divided by the mass of Titan (m), and its radius (R). This factor is related to second degree spherical harmonic gravity coefficients through the Radau-Darwin equation (Darwin, 1879). Furthermore, the potential Love number k_2 gives further information on the interior of a celestial body; it can aid in determining ranges of densities and depths of interior layers of the celestial body (e.g. Sohl et al. (2003); Kramm et al. (2010)).

Table 1. Summary of previous research on Titans gravity field, where the most important unnormalized gravity coefficients and the potential Love number k_2 are shown.

J_2	C_{22}	J_3	k_2	Data (#flybys)	Reference
31.808 ± 0.404	9.983 ± 0.039	-1.879 ± 1.019	-	4	Iess et al. (2010)
33.599 ± 0.332	10.121 ± 0.029	-1.097 ± 0.606	0.589 ± 0.075	6	Iess et al. (2012)
33.089 ± 0.609	10.385 ± 0.084	-0.179 ± 0.720	0.616 ± 0.067	10	Durante et al. (2019)

Several likely interior models have been established with the estimated tidal and gravitational parameters from Table 1 (e.g. Hemmingway et al. (2013); Kronrod et al. (2020)). Assuming ranges of interior parameters, such as depth of the ice shell, or density of the sub-surface ocean, several likely interior models can be predicted by making assumptions about, among others, the heat-flow within the interior of Titan (Sohl et al., 2003). Given the density and rigidity of the several layers of the interior model, the potential Love numbers can be calculated from theory. The estimated k_2 Love number from radio tracking measurements should be consistent with the theoretically calculated Love number corresponding to the interior model of Titan. The interior model should also have a gravity field consistent with the estimated gravity field. Hence, most likely interior struc-

tures can be selected if these values of k_2 and the spherical harmonic coefficients are known, which is why having consensus on the values of these parameters is crucial in determining the interior structure of Titan.

Reviewing previous estimation results of Titan's gravity field (see Table 1), we make one observation. For the determined parameter J_3, the inclusion of more data leads to a smaller magnitude of this parameter (Iess et al., 2012; Durante et al., 2019). The most recent published paper found an estimate for J_3 with a statistically insignificant sign (1σ), which highlights the uncertainty on this parameter (Durante et al., 2019). Additionally, these papers analyzed the Doppler tracking data by (loosely) constraining all estimated parameters, including *all* gravity coefficients and k_2 Love number. Given the importance of these parameters, the influence of the constraints on the gravity coefficients and Love number is indirectly investigated by performing an independent analysis of Cassini Doppler tracking data contributing to the knowledge on Titan's gravity field and tides.

The main goal of this research is thus to obtain an independent estimation of Titan's gravity field and its potential Love number k_2 through the use of a different orbit determination program. The implemented dynamic model will be different from previous research, with the improvement of adding the gravitational attraction of the Saturn A, B, and C rings. We aim to answer the questions: *What are the coefficients of the spherical harmonic expansion of the gravity field of Titan up to degree and order three (1σ)?* and *What is the influence of the applied global constraints on the estimated spherical harmonic gravity coefficients and tidal Love number k_2?*. Answering these questions will increase the affinity on the gravity of Titan. With the use of our estimate for the gravity field, we determine the normalized MOI factor of Titan and the ratio J_2/C_{22} from which hydrostatic equilibrium can be inferred. This would allow future research to better assess likely interior structures for Titan, leading to an accurate evaluation of the habitability of Titan's sub-surface liquid ocean. Section 3.2 tests the robustness of the gravity solution from previous research, which would indirectly verify our implemented dynamic model.

2 Processing

In the entire span of the Cassini-Huyghens mission, the Cassini orbiter performed a total of 124 Titan flybys, ten of which were dedicated to gravity analysis during clos-

est approach (C/A) and thus included tracking data taken during closest approach. For our analysis, we use two-way and three-way ramped Doppler tracking data compressed at ten seconds. Ramped Doppler measurements are obtained from tracking the satellite by transmitting (uplink) a frequency which increases at a known linear rate. Its advantage over unramped Doppler data is that a unique correspondence between time of transmission and frequency is established. Monitoring the time of reception of a signal and its frequency, it can be associated with the time of transmission from which a round-trip distance can be inferred (Liu, 1974). The analyzed Doppler data consist of X-band uplink (7.2 GHz) data and X-band downlink data[1] (8.4 GHz), where previous research also include Ka-band downlink transmission data. X-band data are more sensitive to plasma noise turbulence effects caused by the Sun compared to Ka-band tranmission data (Asmar et al., 2005; Iess et al., 2014). The path of the radio link is monitored by the Sun-Earth-Probe angle, where the angles are all below 20° thus the influence of the Sun plasma noise is minimal (Section 1 in the supplementary materials). For several periods of time during a flyby, both two-way and three-way data are available. Two-way data are preferred over three-way data as less signal noise is introduced in two-way data (Thornton & Border, 2003). Data for which the elevation angle between spacecraft and ground station are below 5° are disregarded, as tropospheric effects can cause a significant error in the measurement (e.g. Tapley et al. (2004)). Observation outliers are removed by hand if the residual is visually different than the neighboring observation residuals. For every flyby, one observation arc is chosen, such that most relevant Doppler data (near C/A) lie within the arc. Arc lengths differ and lie within 1.0 and 2.0 days per flyby, where we use only one arc per flyby. Flybys T022, T045 and T122 had attitude corrections during radio tracking, which have been accounted for by cutting the arc such that these manoeuvres are not inside the arc. Modeling these attitude corrections and desaturations of the momentum wheels by either sets of empirical accelerations, or instantaneous changes to the state vector are not sufficient to completely absorb the Doppler signal caused by these manoeuvres. Shortening of the arc to exclude these events is therefore a better alternative. Radio tracking of the Cassini spacecraft has also lead to two-way and three-way range data. These data, however, do not capture signatures of Titan's gravity field or characteristics from a spherically asymmetrical distribution of mass as accurately as

[1] Data retrieved from `https://atmos.nmsu.edu/data_and_services/atmospheres_data/Cassini/inst-rss.html`

Doppler tracking does (Bertone et al., 2015; Andert, 2010). For this reason, range data will not be included.

When analyzing the observation residuals of flyby T074, two spikes at the start and end of the arc were visible, which look similar to that of an attitude correction. However, no attitude corrections are reported in the archive of attitude corrections during the Cassini mission (NASA PDS, 2020). To avoid this unknown source in the observation residuals, we decided to cut the arc accordingly, thereby only leaving the data near the C/A which excluded this spurious signal.

The GEODYN II orbit determination program (version 1107.3) will be used to process the data (McCarthy et al., 2015). GEODYN II is designed and maintained at NASA Goddard. The transmitted data is affected by physical phenomena altering the data. GEODYN II models the relativistic effects of Saturn and the Sun on the observations. Additionally, atmospheric effects of the Earths atmosphere are modeled. The troposphere refraction corrections are computed based on the Hopfield zenith delay (Hopfield, 1971) with the Niell mapping function (Niell, 1996), implementing meteorological data obtained at every DSN ground station (Lemoine et al., 2013).

The dynamic force model consists of several types of forces. Titans main body potential is included up to third degree and order. In addition, tides generated by Saturn due to Titan's significant eccentricity (e=0.03) cause a change in the gravity potential, called the tidal potential. The corresponding tidal Love number k_2 is not estimated in Section 3.1: it has an initial value of 0.0 during this analysis with a constraint of 10^{-20} and is hence fixed. In Section 3.2, the k_2 Love number is estimated starting with the *a priori* value of 0.616 as found by Durante et al. (2019). The rotational elements of Titan are adopted from Meriggiola et al. (2016), where rotational elements, including precession and nutation, are estimated with SAR images of Titan. All planetary systems, as well as the Sun, are added as third body point mass effects to the dynamic model with their positions taken from the most recent JPL ephemeris DE432. The top seven heaviest moons of Saturn, excluding Titan, are added as third body perturbations as well. Additionally, the gravitational pull of Saturns even zonal harmonics are modeled up to degree eight and taken from Iess et al. (2019). Durante et al. (2019) includes the zonal harmonics of Saturn up to degree ten. The odd and higher degree (>8) zonal harmon-

ics have contributions orders of magnitudes smaller than the remaining lower degree zonal harmonics and are thus neglected.

We modeled the effect of the gravitational attraction of the Saturnian A, B and C rings, with the masses of these rings as found in Iess et al. (2019). The gravitational attraction of the ring masses can be calculated by the superposition of two discs with radii ρ_1 and ρ_2. ρ_1 is then the inner ring radius and ρ_2 is the outer ring radius, where the contribution of the inner disk is subtracted from the contribution of the outer disk. The acceleration due to a ring with a gravitational parameter μ_r on the satellite can be calculated as:[2]

$$\ddot{\mathbf{r}}_b = 2\mu_r \left(\ddot{\mathbf{r}}_d(2) - \ddot{\mathbf{r}}_d(1)\right) / \left(\pi \left(\rho_2^2 - \rho_1^2\right)\right) \tag{3}$$

with

$$\ddot{\mathbf{r}}_d(i) = \begin{bmatrix} \left(-x_b D_i / r^2\right) f_{2i} \\ \left(-y_b D_i / r^2\right) f_{2i} \\ \left(z_b / D_i\right) K\left(k_i\right) + \operatorname{sign}\left(z_b\right)\left(-\pi/2 + \pi/2 \operatorname{sign}\left(r - \rho_i\right) - \operatorname{sign}\left(r - \rho_i\right) f_{3i}\right) \end{bmatrix}$$

where $\mathbf{r}_b$ is the vector from the center of mass (COM) of the planet to the spacecraft in Planet Mean Equator coordinates (similar to Krogh et al. (1982)). $\ddot{\mathbf{r}}_d(i)$ is the contribution to the acceleration from a disk i, where $i = 1$ for the inner disk with radius ρ_1 and $i = 2$ for the outer disk with radius ρ_2. A complete description of the other terms is provided in Section 1 of the supplementary materials.

Cassini has three on-board Radioisotope Thermoelectric Generators (RTG) which exert a significant force on the spacecraft (Benedetto, 2011). This RTG acceleration decreases over time, as the activity of the radioactive source of Cassini's power decreases. The *a priori* values of the RTG acceleration at the start of every arc are calculated from the activity of the radioactive source at the start of the mission and the start time of the arc (Bertotti et al., 2003; Benedetto, 2011). A scale factor multiplying the *a priori* values is estimated, with uncertainties on the RTG accelerations equal to those in Bertotti et al. (2003). A more thorough description of the estimation of the SRP can be found in Section 1 of the supplementary materials. Solar radiation pressure (SRP) is calculated with a simplified spacecraft panel model, where we estimate a solar radiation coefficient.

[2] from the DPTRAJ-ODP User's Reference Manual, Vol. 1

The same panel model is used for calculating the drag force by the atmosphere of Titan, using the Titan-GRAM model as atmosphere model (Duvall et al., 2005). We estimate a drag coefficient to resolve any mismodeling of the drag force, especially important for the low altitude flybys T022 and T068. Finally, empirical accelerations in radial, along- and cross-track direction are estimated. Modeling errors inevitably occur when building the dynamic model. These accelerations are necessary to compensate for mismodeling of forces, leading to a fit of the observation residuals to the RMS of the expected noise level (Section 4 of the supplementary materials provides the residual plots of every arc). The periods of these empirical accelerations is chosen to be eight hours to allow at least three sets of empirical accelerations during one arc. However, occasionally these periods are increased or decreased to increase the fit of the model, which differs per flyby, leading to occasionally longer or shorter acceleration periods (see Figure 1 of the supplementary materials).

One of the most important parameters for the determination of Cassini's orbit, is its *a priori* state vector which consists of Cassini's position and velocity. The *a priori* conditions are taken from the most recent versions of ephemeris files available from the navigation team of NASA JPL. Constraints on Cassini's state vector are taken to be 2 km and 2 cm/s as is done in Durante et al. (2019). Additional non-force related parameters need to be estimated, to increase the fit of the dynamic model. We estimate the position of the center of mass with respect to the antenna transmitter, called the antenna offset. This filters out any signal in the Doppler residuals due to rotations of the satellite. Observation biases are estimated, to absorb any signal in the Doppler residuals due to any mismodeling of the effect of Earth's atmosphere on the observations (Lemoine et al., 1997). These biases are estimated for every uplink-downlink combination between satellite and any of the ground stations of the Deep Space Network. Furthermore, the position of Titan is uncertain: its position in ephemeris files from NASA JPL is based on observations and models. The Saturnian planetary system consists of many uncertainties including among others tidal dissipation and frequency dependent tides (Tyler, 2014; Durante et al., 2019). Hence, there exists a discrepancy between Titan's actual position and its position in the ephemeris files. This discrepancy could cause a constant bias in the observation residuals. These estimated station biases are thus used to mitigate the effect of the uncertainties in Titans position. Section 3.2 sheds light on the necessity of the estimation of these parameters.

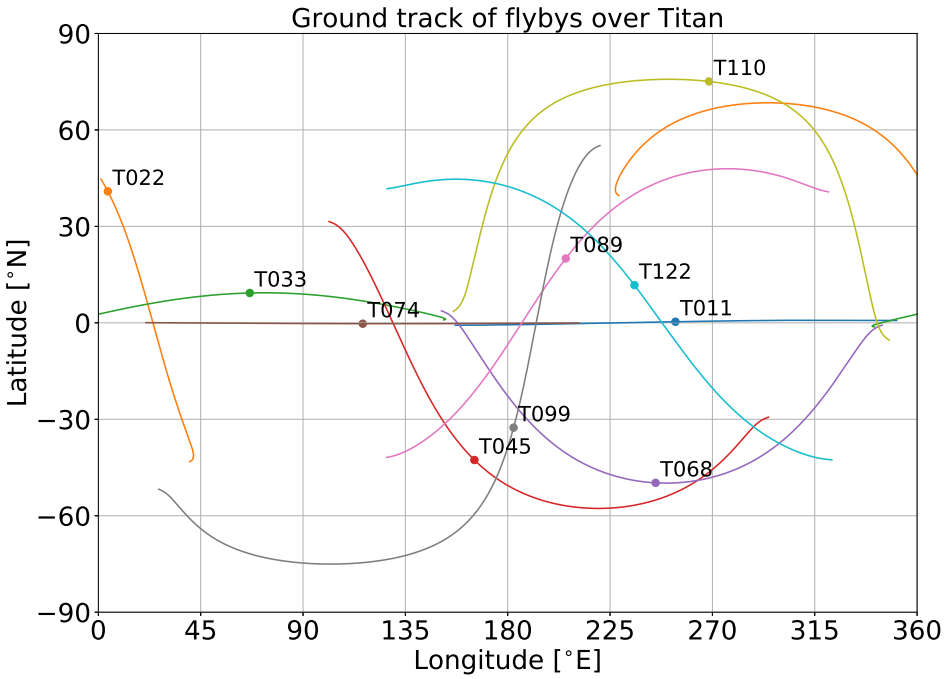

Figure 1. Coverage of all ten flybys six hours before and after the point of C/A. The C/A position is indicated by a point for every arc.

All ten flybys are processed in a multi-arc batch weighted least squares process with one arc per flyby. Several iterations are necessary to reach a converged global solution. The ramped Doppler data is given an *a priori* observation error of 0.028 Hz equivalent to 1 mm/s for X-band transmission frequencies. Individual arcs are weighted according to their ground coverage. Figure 1 displays the ground track of all the considered flybys. Flybys having a ground track in the Eastern Hemisphere of Titan, and spanning higher latitudes are given a relatively larger weight, as data from these flybys contain more relevant information on the zonal coefficients and k_2. This methodology of applying weights to flybys is different from previous research (Durante et al., 2019; Iess et al., 2012), which bases weights on the RMS of the residuals. Adopting the same methodology would result in several important flybys (i.e. covering high latitudes) being given a significantly lower weight than flybys which only fly over the equator. The applied weights of the flybys can be found in Table 3 of the supplementary materials. Section 3 of the supplementary materials provides a robustness analysis of these arc weights, illustrat-

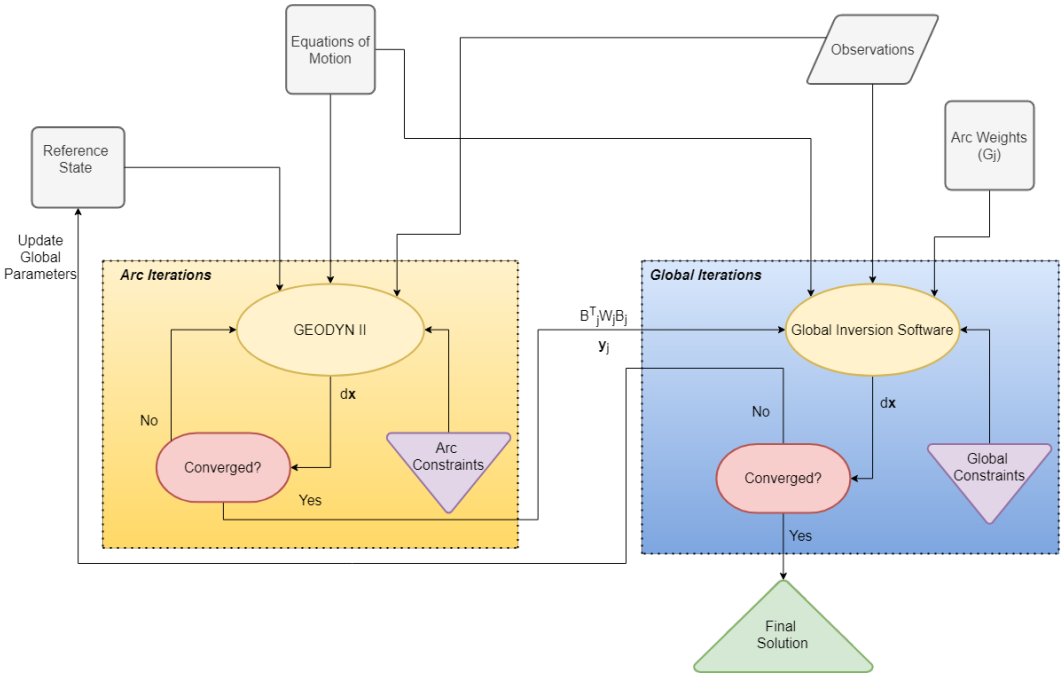

Figure 2. Flow diagram of the gravity determination split up into arc and global iterations. $d\mathbf{x}$ are the adjustments of the parameters. After convergence of arc iterations, GEODYN II outputs the normal matrices $B_j^T W_j B_j$ and residual vector $\mathbf{y}_j$. Together with the arc weights G_j, the normal matrices and residual vectors are combined after which a global iteration takes place. Note that during the global iterations, also all arc parameters are adjusted.

ing that a statistically insignificant result is obtained if the weights are applied as inversely proportional to the residual RMS, similar to Durante et al. (2019).

Figure 1 also immediately illustrates one of the problems with the dataset: Titan's surface is quite richly sampled in the Western Hemisphere, whereas sampling is poor in the Eastern Hemisphere. There is no data in the North Eastern region ($30°-90°E$, $>15°N$). This results in a high correlation between global gravity parameters defining the gravity in those regions. Since no physical constraints on the parameters can be set, we opt for a solution without constraining these parameters to reduce any undesirable bias, further discussed in Section 3.1.

The orbit determination and gravity analysis is split up in two parts, similar to the procedure in Mazarico et al. (2014) (Figure 2). GEODYN II is utilized for the orbit determinations where only arc-specific parameters are adjusted until convergence. During these arc iterations, the global parameters are constrained tightly. Afterwards, the nor-

mal matrices of all arcs are combined into a weighted multi-arc normal matrix, with different weights per arc as follows:

$$N_{tot} = \sum_{j}^{n_{arc}} G_j \cdot B_j^T W_j B_j \qquad (4) \qquad\qquad \mathbf{y}_{tot} = \sum_{j}^{n_{arc}} G_j \cdot B_j^T W_j \mathbf{y}_j \qquad (5)$$

where N_{tot} is the combined normal matrix, G_j is the weight of arc j based on the coverage of every flyby (see Table 3 in the supplementary materials), B_i is the design matrix of arc j (and B_j^T its transpose), W_j is the observation weight matrix, $\mathbf{y}_{tot}$ is the total residual vector of the observations and $\mathbf{y}_j$ are the residuals of the observations of arc j. The constraint matrix will be added to N_{tot} with a weight of 1.0. In other words, every constraint is weighted equally heavy, even if the weights of the arcs are different. We want to constrain a certain parameter by allowing a certain adjustment, independent of the applied weight of the arc which the parameter belongs to. Hence, we perform a global iteration by solving for $d\mathbf{x}$ in the following equation:

$$(N_{tot} + W_{constraint})\, d\mathbf{x} = \mathbf{y}_{tot} \qquad (6)$$

where $d\mathbf{x}$ are the adjustments of the state vector $\mathbf{x}$ consisting of all the estimated parameters. The values of $\mathbf{x}$ will be updated through $\mathbf{x} = \mathbf{x} + d\mathbf{x}$, after which the whole process is repeated (including new arc iterations) until convergence of the global parameters (see Figure 2). Commonly, convergence is reached if the adjustments of the parameters are within 1.0% of the magnitude of the parameters (McCarthy et al., 2015). This approach is undesirable and will not work here, as several global parameters with small magnitudes have adjustments larger than one percent for all iterations due to among others strong correlation with other global parameters. This problem does not arrise for gravity coefficients larger in magnitude, such as C_{22} and J_2. Hence, convergence is defined to be reached if most large parameters do not change with adjustments larger than 1%. The formal errors on the smaller gravity coefficients are generally larger than its magnitude which makes it hard to draw any solid conclusion on these smaller parameters and justifies this convergence method. The formal errors of the parameters are calculated as follows:

$$P = (N_{tot} + W_{constraint})^{-1} = \left(\sum_{j}^{n_{arc}} G_j \cdot B_j^T W_j B_j + W_{constraint} \right)^{-1} \qquad (7)$$

with the formal error of parameter l being $\sigma_l = \sqrt{P_{ll}}$. Immediately, we observe that if N_{tot} becomes larger, the formal error decreases. Given that the arc weights are different and much smaller compared to previous research (Durante et al., 2019), the formal errors will also be different, discussed in detail in Section 3.1.

Table 2. Short summary of the several flybys taken into consideration in the gravity analysis. The RMS of the residuals shows that the dynamic model fits the data well within the expected noise level. Note that an observation residual of 1.0 mHz in the X-band translates to ∼0.038 mm/s.

Flyby	C/A date (UTC) (yy-mm-dd hh:MM)	Observations (at 10 s sampling)	RMS of the residuals (mHz)
T011	06-02-27 08:25	3233	5.462
T022	06-12-28 10:05	4858	4.682
T033	07-06-29 17:00	4075	5.676
T045	08-07-31 02:13	12736	4.104
T068	10-05-20 03:24	8674	3.801
T074	11-02-18 16:04	9162	9.952
T089	13-02-17 01:56	13245	1.833
T099	14-03-06 16:27	10064	5.117
T110	15-03-16 14:30	7244	4.296
T122	16-08-10 08:31	10163	5.237

In summary, we solve for Titan's global spherical harmonic gravity field coefficients up to degree and order three and the gravitational parameter of Titan, μ. The tidal Love number k_2 is given an *a priori* value of 0.0 in Section 3.1 and is not estimated during our independent estimation process. It is, however, included in the estimation process in Section 3.2, as that is necessary to check the robustness of the solution from Durante et al. (2019) with our dynamic force model. The estimated arc parameters are: drag and solar radiation coefficients C_R and C_D, RTG forces in the form of scale factors applied to a certain *a priori* force, antenna positions, observation biases, Cassini state parameters, and empirical accelerations. A short summary on the several flybys taken into consideration as well as the number of Doppler measurements (at 10 s) and their correspond-

ing residual RMS can be found in Table 2. Section 1 of the supplementary materials provide information on among others the altitude and arc length of the ten flybys, as well as how every parameter is initialized and constrained.

In order to improve the convergence and stability of the adjustments, we first estimate a gravity field of degree and order two by applying the methodology outlined above and summarized in Figure 2. After a converged 2x2 gravity field has been obtained, the methodology is applied to determine the spherical harmonic gravity field of Titan up to degree three (Section 3.1). Instead, the *a priori* values of the second degree coefficients are initialized with the values determined in the 2x2 gravity analysis, explained in Section 3.1.

3 Gravity solutions

This section discusses and interprets the results of the 3x3 gravity field obtained by an independent analysis of the GEODYN II orbit determination software. The analysis is based on a different dynamic model without global constraints, in contrast to Durante et al. (2019). In Section 3.1, we propose a 3x3 gravity solution excluding the estimation of a tidal Love number. We discuss correlations in the global parameter set as well as important geophysical parameters, such as C_{22}, J_2, the J_2/C_{22} ratio and their interpretation. Subsequently, we test the robustness of the solution from Durante et al. (2019) with our dynamic model. This simultaneously verifies our dynamic model as well as the gravity solution from Durante et al. (2019).

3.1 Zero initial gravity field

The estimation of a gravity field was first initialized using a 2x2 gravity field, starting with an initial gravity field with coefficients all equal to zero. Along with this 2x2 gravity field, no k_2 is estimated to first deduce a more stable 2x2 gravity field. After three iterations, the 2x2 gravity field converged. We added the degree and order three terms, while initializing the degree two terms with the converged values, leading to the estimated 3x3 gravity field in Table 3 after four additional global iterations (hereafter referred to as baseline solution). For this solution, no k_2 Love number is estimated. Including said Love number results in infeasible and unstable solutions with our implemented dynamic model and applied constraints, elaborated upon below. We estimated the gravity field

Table 3. Estimated unnormalized gravity field coefficients of the 3x3 gravity field and gravitational parameter, μ, including estimated 1σ uncertainties.

μ	8977.9810 ± 0.0130	km^3/s^2	
J_2 ($\times 10^6$)	30.607 ± 1.536		
C_{21} ($\times 10^6$)	-4.411 ± 0.798	S_{21} ($\times 10^6$)	12.042 ± 1.23
C_{22} ($\times 10^6$)	8.331 ± 0.502	S_{22} ($\times 10^6$)	-2.258 ± 0.459
J_3 ($\times 10^6$)	1.143 ± 2.207		
C_{31} ($\times 10^6$)	1.419 ± 0.631	S_{31} ($\times 10^6$)	6.16 ± 1.108
C_{32} ($\times 10^6$)	-1.251 ± 0.37	S_{32} ($\times 10^6$)	-0.139 ± 0.261
C_{33} ($\times 10^6$)	0.018 ± 0.09	S_{33} ($\times 10^6$)	-0.611 ± 0.09

up to degree three, as the data do not seem to contain sufficient information on the higher degree coefficients, investigated in Section 3 of the supplementary materials.

The power of the spherical harmonic degrees is plotted and compared to a Kaula power law K/l^2 with $K = 10^{-5}$ in Figure 3 (Kaula, 1966). The power of degree two and three is larger than the Kaula law, our estimate of the gravity thus predicts a higher empirical power law for the gravity coefficients. An important observation is that the power for the third degree is lower than the power of degree two: something we expect to happen as smaller features of the gravity field, represented by higher degree coefficients, are expected to have a lower power. The power of the uncertainties is a little higher for degree three compared to degree two, among others due to a relatively high formal error for J_3 (Table 3).

In Figure 4, the anomalies of the determined gravity field from Table 3 have been plotted on a sphere with reference radius $R_{ref} = 2575$ km. Besides the expected large positive anomalies near 0°E and 180°E of Titan's surface pointing towards and away from Saturn, respectively, we observe an additional large positive anomaly between 60−150°E and 20−60°N. This field is thereby substantially different from the one obtained in Durante et al. (2019) and Iess et al. (2010), directly resulting from the large differences between the determined values for C_{21} and S_{21}. These differences arise from a different methodology of determining these global parameters, as elaborated upon below. Differences of more than twice the formal error between the obtained values for C_{21} from Iess et al. (2012)

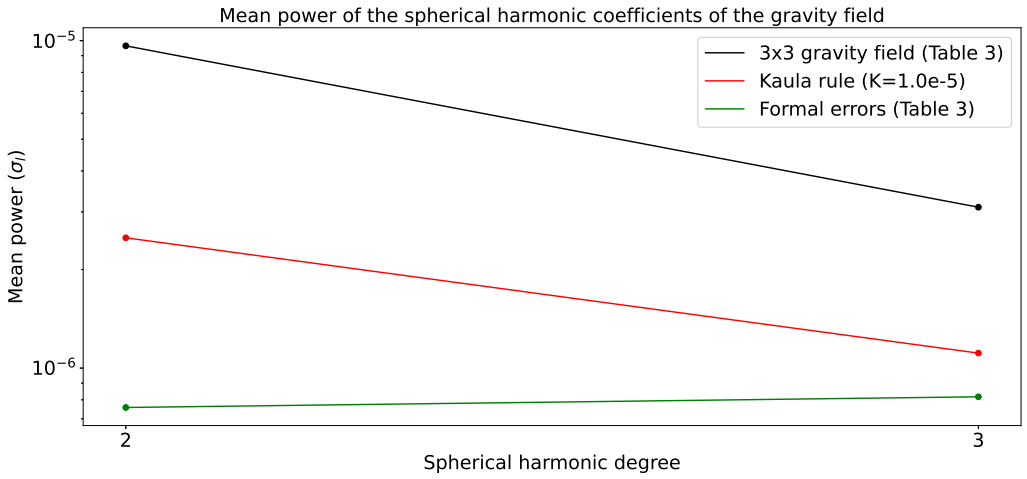

Figure 3. The mean power (σ_l) of the second and third spherical harmonic degrees, including formal errors, compared to a Kaula constraint of $\sigma_l = \frac{10^{-5}}{l^2}$. The mean power of the normalized gravity coefficients is calculated as $\sigma_l = \sqrt{\frac{\sum_m (\bar{C}^2_{lm} + \bar{S}^2_{lm})}{2l+1}}$.

and Durante et al. (2019) exist as well, though they are an order of magnitude smaller than the values found in this research.

The methodology of the gravity determination process is fundamentally different from the one implemented in Durante et al. (2019). First of all, the *a priori* uncertainty on the global parameters is infinitely large; no constraints are applied on the global parameters. Durante et al. (2019) gives bounded *a priori* variances (constraints) to the global parameters. It is not possible to impose constraints on the global parameters with a physical meaning in this case, hence we opt for a solution without global constraints. Secondly, in Iess et al. (2012), the initial conditions of J_2 and C_{22} were set to $3.33 \cdot 10^{-5}$ and $1.0 \cdot 10^{-5}$, respectively: a value close to those found in earlier research (Iess et al., 2010). If the same procedure as in Iess et al. (2012) is applied, then this means they started with an initial condition unequal to zero for these two coefficients. Yet, a total of four radio tracking flybys have been performed since, which could have a significant impact on the estimated value for C_{22}, especially considering the large visible differences between other parameters from previous research (J_3 for example, see Table 1). This could lead to a sub-optimum solution as the conditions for the gravity field are initialized from a potential local minimum. This is difficult to prove however, but we try to prevent getting stuck in a local minimum by starting from a zero initialized gravity field and iter-

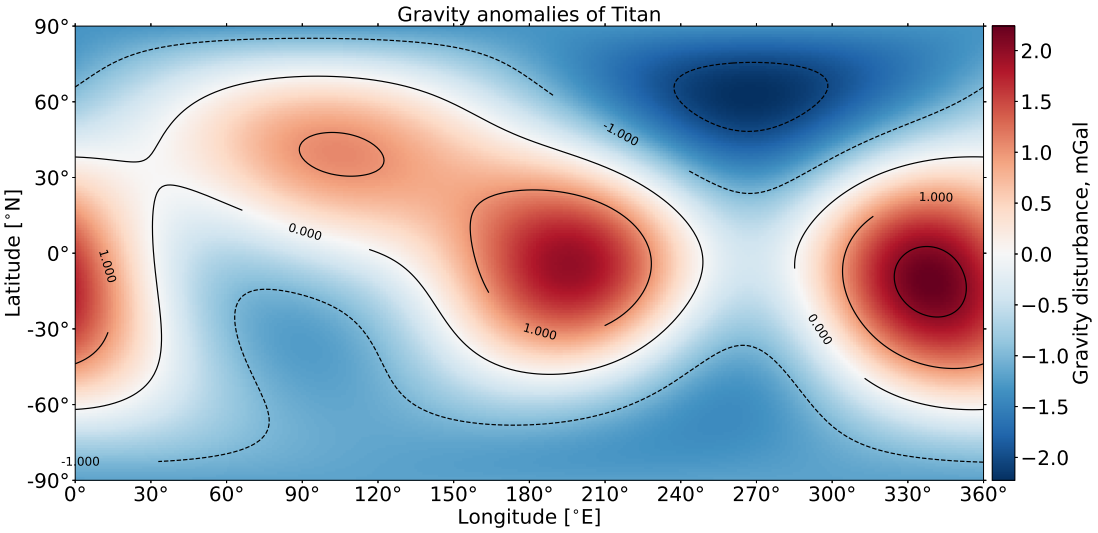

Figure 4. Titan's gravity anomalies in mGal with a reference radius of $R_{ref} = 2575$ km. The minimum and maximum anomalies are -2.225 mGal and 2.241 mGal, respectively. Contour lines are drawn for increments of 1.0 mGal.

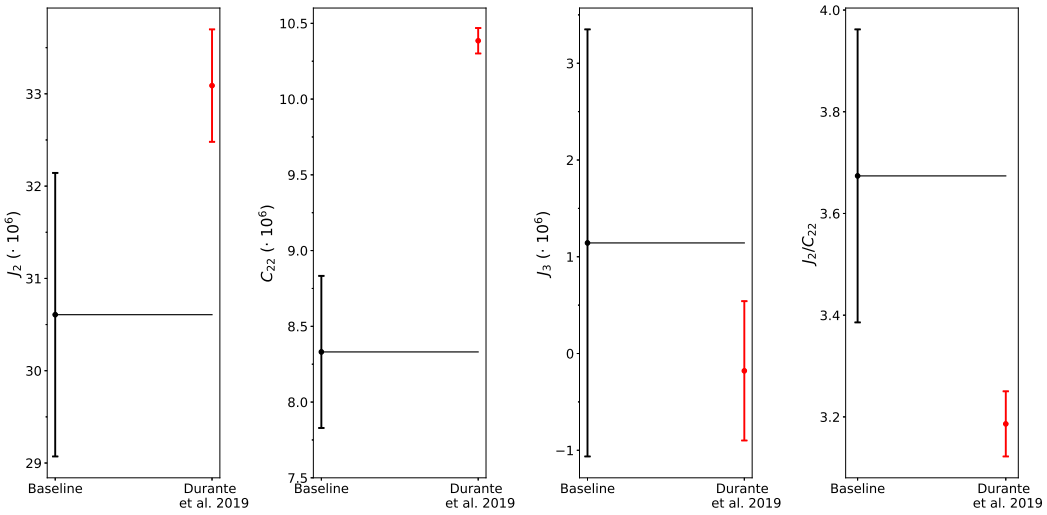

Figure 5. Comparison between our proposed baseline solution (Table 3) and the 5x5 gravity field solution from Durante et al. (2019), with 1σ formal errors.

ating the global solution several times. In addition, differences between the implemented dynamic models also exist, explained in Section 2. We compare our proposed baseline solution (Table 3) with the 5x5 gravity field solution including the estimation of a k_2 Love number (Durante et al., 2019), see Figure 5. This plot immediately demonstrates several differences and similarities in solutions for the crucial parameters J_2, C_{22}, and J_3,

important for inferring interior and inertia properties of Titan. The formal errors are significantly larger in this research: a direct consequence of the higher *a priori* variances and the applied arc weights (see Equation 7). A second difference lies in the obtained value for C_{22}, as this is a statistically different value (beyond 3σ), caused by the different methodology.

Unlike Durante et al. (2019), we do not estimate a tidal Love number k_2 with our implemented dynamic model. Including said Love number resulted in infeasible solutions of the Love number; either negative values or values larger than one. A possible explanation is the high correlation of several global parameters with the Love number. Poor coverage of the surface of Titan leads to large correlations of the coefficients and parameters that we want to estimate. Figure 6 shows the correlation between several lower degree gravity parameters with k_2 and μ. Certain parameters correlate significantly, which means they cannot be determined uniquely with a high certainty, if this correlation is left unresolved. Recent research has found a robust solution (Section 3.2) of the 5x5 gravity field of Titan including the tidal k_2 Love number. The fact that we have not estimated a feasible solution for the tidal Love number has two possible reasons.

First of all, in earlier research (Iess et al., 2012), initial conditions of the two largest spherical harmonic coefficients J_2 and C_{22} were set to earlier determined values, as noted.[3] Secondly, Durante et al. (2019) applies *a priori* uncertainties on the global parameters as well, where it is claimed these constraints are loose and do not constrain the solution. These differences in methodology seem to contribute to the solution. We found solutions of Titan's gravity field while not implementing any constraints on the global parameters. Solutions with a global constraint on k_2 were attempted but yielded infeasible negative Love numbers, possibly caused by the remaining substantial correlations with other global parameters. No solutions were attempted where (loose) constraints are applied to gravity coefficients as these applied constraints are not physical, thus leading to undesirable solutions since we cannot properly evaluate the validity of the applied constraints. The estimation of the 3x3 gravity field was performed by starting from a stable 2x2 gravity field as explained above, obtaining the solution proposed in Table 3. These fundamental differences may explain why previous research was able to determine the 5x5 grav-

[3] this is further explained in the supplementary materials of Iess et al. (2012), which can be found at `https://science.sciencemag.org/content/337/6093/457/tab-figures-data`

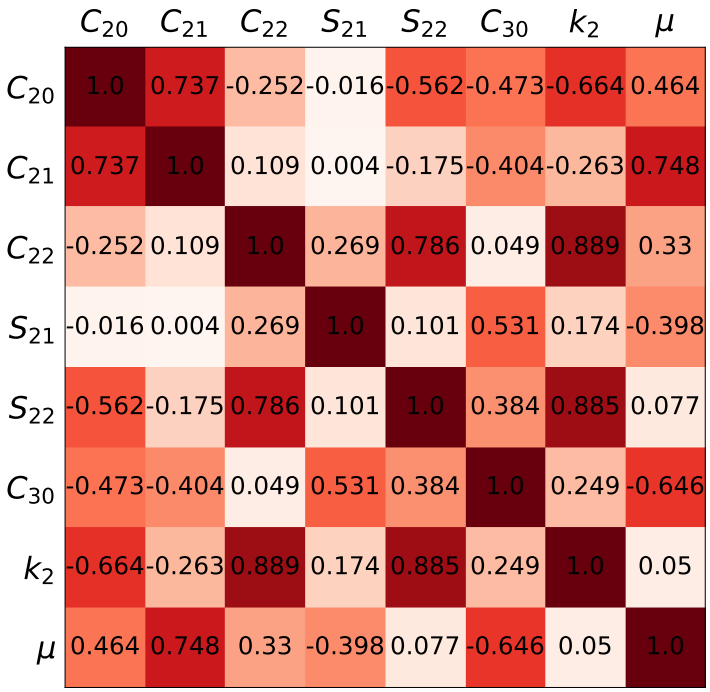

Figure 6. Correlation matrix of several parameters having implemented the baseline model, with a 5x5 gravity field and tidal Love number k_2. The more red an entry in the matrix is, the more correlated the parameters are. Note that this matrix shows the correlation coefficients (ρ) of the parameters.

ity field and tidal Love number. One could argue that giving initial conditions to any of the estimated gravity coefficients as well as applying global constraints, could add undesired bias to the solution.

A possibility to overcome the correlation of global parameters is by applying global constraints. Common in the field of gravity determination, is the application of a Kaula constraint, which gives an *a priori* power distribution of the spherical harmonic gravity coefficients (Kaula, 1966). Durante et al. (2019) correctly points out that applying a Kaula constraint is undesirable as there exists no *a priori* information on the power distribution of the spherical harmonic gravity coefficients of Titan or icy moons in general. Yet, they apply (loose) constraints on the gravity coefficients and other global parameters. The application of these non-physical constraints is generally to be avoided, as they could introduce undesired bias in the solution. Since constraints on spherical harmonic coefficients are indeed non-physical in nature in this case, we refrain from its application and therefore opt for a solution without them.

Significant similarities between the studies are visible as well. Reviewing Figure 5, we see that both J_2 and J_3 lie within two times the formal error. For J_2 this is more significant: the formal error is not too large compared to its magnitude. The magnitude and sign of J_3 are less certain; this is shown in the uncertainties on J_3 by both this research and Durante et al. (2019). Poor sampling of Titan's surface, especially higher latitudes, leads to the large uncertainty of this parameter.

In addition to the spherical harmonic gravity coefficients and tidal Love number k_2, the normalized moment of inertia factor (MOI) constraints the interior model of a celestial bodies similarly, supporting the interior determination of Titan (Murray & Dermott, 1999). For a body in hydrostatic equilibrium, the Radau-Darwin equation relates the polar flattening f and the gravity coefficient J_2 to the normalized MOI factor as follows (Darwin, 1879; Murray & Dermott, 1999):

$$\frac{J_2}{f} = -\frac{3}{10} + \frac{5}{2}\overline{\mathcal{C}} - \frac{15}{8}\overline{\mathcal{C}}^2 \tag{8}$$

This assumes that the interior of Titan consists of a core surrounded by an infinitely small ocean (Murray & Dermott, 1999).

To estimate the moment of inertia factor, an expression needs to be found for the polar flattening f. For that, a reference ellipsoid is calculated. Including contributions of the tidal potential due to Saturn, the gravitational potential, and the rotation of Titan, we find the ellipsoidal radii to be (a, b, c) = (2575.219, 2574.937, 2574.844) km, with a reference radius of 2575 km and a rotational parameter q of $3.9555{\cdot}10^{-5}$ (see Murray and Dermott (1999) and Iess et al. (2010)). Here, c is the polar ellipsoidal radius. To obtain an estimate for the polar flattening, the average of a and b is taken as equatorial radius. Applying Equation 8 then results in a MOI factor of 0.342, very close to the earlier determined value of this factor (Durante et al., 2019; Iess et al., 2012). Still, this is with the assumption that the body mainly consists of a large core and infinitely thin ocean (Murray & Dermott, 1999). The opposite scenario (a point core and an ocean equal to the radius of Titan) would give an inertia factor of 0.336, given our value for J_2 in Table 3. The Radau-Darwin relation assumes an interior model consisting of a core surrounded by an infinitely small ocean as noted. The MOI value will likely be close to 0.342, as Titan is likely to consist of an inner core with a surrounding (sub-surface) ocean with

finite thickness, confirmed by the previously determined k_2 Love number in Durante et al. (2019).

The ratio J_2/C_{22} can be used to infer hydrostatic equilibrium within a celestial body, although it is not possible to confirm hydrostatic equilibrium on this condition alone. Celestial bodies in hydrostatic equilibrium have a fully differentiated interior, which consequently can support the determination of their interior. A theoretical value of $J_2/C_{22} = 10/3$ to first order would apply to bodies in hydrostatic equilibrium (Murray & Dermott, 1999). The baseline solution predicts $J_2/C_{22} = 3.674 \pm 0.288$, compatible with a body of hydrostatic equilibrium within two times the formal error. Figure 5 contains the plot of J_2/C_{22} and compares this ratio to the one obtained in Durante et al. (2019), where our solution is also compatible to 2-σ with their solution. Additionally, the ratio of $(b-c)/(a-c)$ is equal to 0.25 (using a, b, and c as calculated above), as expected for a synchronous rotating body in hydrostatic equilibrium bearing tidal and rotational deformations (Murray & Dermott, 1999). It is thus likely that Titan is in hydrostatic equilibrium, and it's interior is therefore likely to be fully differentiated.

We should keep in mind that including a k_2 Love number in our estimate (Table 3) will inevitably yield different solutions, where we expect that most of the coefficients (including C_{22}) would have estimates closer to those from previous research, given the strong correlation between k_2 and other gravity coefficients in Figure 6. Excluding a k_2 estimation leads to absorption of signal originating from k_2 by the gravity parameters, yet the observed estimate of the Love number would be negative if k_2 is included in the estimation. As noted, this is caused by the strong correlation between global parameters, in combination with not applying global constraints. Note that strictly $k_2 > 0.0$, hence negative Love numbers are infeasible.

3.2 Stability of solutions previous research

We analyzed the robustness of the solution from Durante et al. (2019) and simultaneously verified several of our dynamic models. We perform one global iteration with the gravity field from Durante et al. (2019) as *a priori* conditions. During this iteration, only global parameters are unconstrained: arc parameters are fixed to their arc iterated converged values obtained in a similar fashion through arc iterations (Figure 2). The solution did not converge to a feasible one if the arc parameters are constrained similar to

the baseline solution (Table 3.2 of the supplementary materials), with the estimation of the spherical harmonic gravity field up to degree five and Love number k_2. This is caused by a combination of severe correlation between global parameters as well as not constraining the global parameters, elaborated upon hereafter.

Figure 7 demonstrates the result of several dynamic models compared to that of Durante et al. (2019), after one global iteration. We compare the results of the *baseline* model from Section 2 and two slight alterations, to the results of Durante et al. (2019). To compare, we implement a 5x5 gravity field instead of the 3x3 gravity field. The model *No COM* (Figure 7) does not estimate COM positions with respect to the position of the antenna. The *No obs. bias* solution does not estimate observation biases. For different models, we see that the obtained parameters k_2 and J_2 remain within the vicinity of the previously determined values after one global iteration. We also observe, however, significant shrinkage of the coefficient C_{22}. Hence, our models predict a lower C_{22} coefficient.

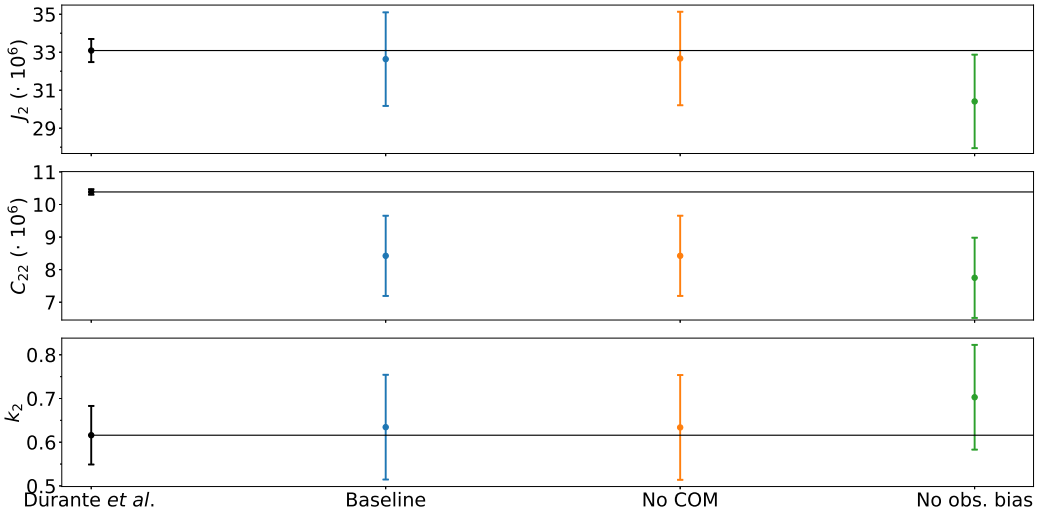

Figure 7. Estimated unnormalized J_2, C_{22} and k_2 parameters for several different models after one global iteration, including 1σ formal errors, starting from an initial gravity field of Durante et al. (2019). The baseline model is the dynamic model which is extensively described in Section 2. The *No COM* and *No obs. bias* solutions have implemented models which deviate from the baseline solution by excluding COM estimations and observation bias estimations, respectively.

In addition, not estimating observation biases leads to a significantly different J_2 compared to the other models and previous research. The estimation of observation biases on the Doppler measurements was already believed to be necessary (e.g. Lemoine et al. (1997); Goossens and Matsumoto (2008), and shown in Section 1 of the supplementary materials), and the results from Figure 7 support this conclusion. Aside from filtering out errors on the influence of the Earths atmosphere on the observations, these biases can also mitigate the effect of the uncertainty on Titan's position, which in previous research is solved by estimating Titan's position directly (Durante et al., 2019) . The employed version of GEODYN II does not have the ability to estimate Titan's state vector.

Performing another global iteration of the newly determined gravity field does result in significantly different results. Usually, k_2 is observed to increase as J_2 increases due to their positive correlation (Figure 6). Hence, this behaviour does not come as a surprise; it only indicates that certain parameters have to be constrained, albeit loosely, to avoid them from growing too large. This includes global parameters as well, which has been done in previous research (Iess et al., 2012; Durante et al., 2019). The downside of these constraints is that they cannot be linked with physical properties of the parameters, which could introduce bias in the solution; an important reason for not applying them in this work.

Lastly, estimating a gravity field larger than 3x3 could result in more instabilities as it is possible that several higher degree and order parameters of the gravity field cannot be determined accurately (Section 3 of the supplementary materials). This is already confirmed by the solution proposed in Durante et al. (2019), as there are several gravity parameters with uncertainties larger than their magnitudes. We found no feasible solution of the k_2 Love number with our methodology from Section 3.1. The difficulty of obtaining the tidal Love number is also experienced by Anderson and Schubert (2013), who were unable to estimate a Love number from six gravity flybys. Results from Anderson and Schubert (2013) were preliminary at the time of publishing, though no subsequent article is found. An empirical power law, such as the Kaula rule, can be applied to force a more feasible solution (Kaula, 1966). Yet, the underlying power law of the gravity coefficients of Titan remains unknown as Durante et al. (2019) also states. Scaling the Kaula constraint might be an alternative (McMahon et al., 2015; Ermakov et al., 2018), though there is not sufficient available data on gravity fields of icy moons to find a scaling law

for the Kaula constraint applicable for this class of celestial bodies. In addition to this empirical Kaula constraint, separate constraints on global parameters, non-physical in nature, are avoided in this research. With that implementation, the degree two and three coefficients, and tidal Love number k_2 from previous research, are verified with a different implemented dynamic model. It should still be investigated what minimum global constraints are necessary, to allow for a feasible solution of the k_2 Love number.

4 Conclusion

In this work, we have shown that it is possible to obtain a stable solution of the gravity field up to degree and order three by first obtaining a stable 2x2 field without the estimation of the k_2 Love number. After convergence, the degree three spherical harmonics are included, while initializing the degree two spherical harmonic coefficients to their converged value. In order to obtain solutions of the gravity field, empirical accelerations and observation biases have been constrained tightly, while leaving global parameters unconstrained during global iterations. The estimation of these empirical accelerations are necessary as other parameters, specific for the flybys, converge to infeasible values otherwise. No feasible estimation was found for the k_2 Love number yet, due to remaining high correlations between this and other global parameters. Attempts at higher order gravity field solutions with this adopted approach have not yielded realistic gravity field solutions, with our implemented dynamic model.

The 5x5 gravity field solution proposed in earlier studies (Durante et al., 2019) is a robust solution. After one global iteration, with several of our implemented models without implementing global constraints, the solution of the gravity field and Love number is not significantly different from the initial solution. For the robustness analysis, only the lower degree coefficients were used to define the robustness of the solution. Spherical harmonic coefficients beyond degree three changed substantially however, which, amongst others, is due to significant correlation and not applying global constraints in our analysis.

Even though in previous research no Kaula constraint has been applied when solving for the gravity coefficients, constraints on global parameters were applied. We are unable to obtain feasible solutions of a 3x3 (or higher) gravity field including tidal Love number with unconstrained global parameters, whilst initializing the gravity coefficients

and tidal Love number at zero. Alternatively, it is possible that in previous research a more gradual approach to the problem is adopted, given earlier analyses done on this topic: more data are added to the gravity determination process after already having obtained a - stable - gravity solution from a previous subset of data and determinations of the gravity field. This could lead to initialization of the problem around a (local) minimum already, which would not allow the final solution to be fully unbiased. If the initial conditions belong to a local minimum, the solution will most likely remain in this local minimum, especially since additional global constraints are applied. For these reasons, we opted for a solution from an initial gravity field solution of zero while not implementing any non-physical constraints on all global parameters. As a result, we were unable to estimate a k_2 Love number uniquely, due to the inevitably high correlations between global parameters caused by severe lack of data and poor sampling of Titan's surface.

The obtained results for J_2, moment of inertia factor (from the Radau-Darwin equation) and the ratio of J_2/C_{22} comply with previous research. The ratio of J_2/C_{22} also complies with the ratio for a body in hydrostatic equilibrium, suggesting a fully differentiated interior structure for Titan. The estimated parameters in this research still have considerable formal errors, much larger than previous research, making it harder to draw solid conclusions regarding these parameters.

This research led to an independent analysis of Doppler measurements yielding an estimation of the gravity field up to degree three of spherical harmonics. Constraints in the multi-arc weighted least squares analysis are only applied to the arc specific parameters. Large correlations between certain global parameters make it difficult to estimate them uniquely. Previous research has implemented loose constraints on global parameters to resolve the correlation; a method not applied here as there exists little information on what constraints are valid, due to their non-physical nature. More research has to be done in the application of these non-physical global constraints and its direct influence on the gravity solution. In addition, the downlink Ka-band transmission data should be added to the analysis, as this is less sensitive to disturbances caused by the solar plasma turbulence.

References

Anderson, J., & Schubert, G. (2013). Titan's gravitational field inferred from six Cassini flybys. *American Geophysical Union*.

Andert, T. P. (2010). *Masses of small bodies: Mass estimation of small solar system bodies using radio science data from close flybys* (Doctoral dissertation, Universität zu Köln). Retrieved from `https://kups.ub.uni-koeln.de/3050/`

Asmar, S. W., Armstrong, J. W., Iess, L., & Tortora, P. (2005). Spacecraft Doppler tracking: Noise budget and accuracy achievable in precision radio science observations. *Radio Science*, *40*(2). Retrieved from `https://agupubs.onlinelibrary.wiley.com/doi/abs/10.1029/2004RS003101` doi: https://doi.org/10.1029/2004RS003101

Benedetto, M. D. (2011). *The non-gravitational accelerations of the Cassini spacecraft and the nature of the "Pioneer anomaly"* (Unpublished doctoral dissertation). University of Rome.

Bertone, S., Jäggi, A., Arnold, D., Beutler, G., & Mervart, L. (2015). Doppler orbit determination of deep space probes by the Bernese GNSS software.

Bertotti, B., Iess, L., & Tortora, P. . (2003). A test of general relativity using radio links with the Cassini spacecraft. *Nature*, *425*, 374-376.

Darwin, G. (1879). I. On the bodily tides of viscous and semi-elastic spheroids, and on the ocean tides upon a yielding nucleus. *Philos. Trans. R. Soc. London*, *170*(1). doi: 10.1098/rstl.1879.0061

Durante, D., Hemingway, D., Racioppa, P., Iess, L., & Stevenson, D. (2019). Titan's gravity field and interior structure after Cassini. *Icarus*, *326*, 123-132. doi: https://doi.org/10.1016/j.icarus.2019.03.003

Duvall, A., Justus, C., & Keller, V. (2005). Global reference atmospheric model (GRAM) series for aeroassist applications. In *43rd aiaa aerospace sciences meeting and exhibit.* Retrieved from `https://arc.aiaa.org/doi/abs/10.2514/6.2005-1239` doi: 10.2514/6.2005-1239

Ermakov, A. I., Park, R. S., & Bills, B. G. (2018). Power laws of topography and gravity spectra of the solar system bodies. *Journal of Geophysical Research: Planets*, *123*(8), 2038-2064. Retrieved from `https://agupubs.onlinelibrary.wiley.com/doi/abs/10.1029/2018JE005562` doi: https://doi.org/10.1029/2018JE005562

Goossens, S., & Matsumoto, K. (2008). Lunar degree 2 potential Love number determination from satellite tracking data. *Geophysical Research Letters*, *35*(2). Retrieved from https://agupubs.onlinelibrary.wiley.com/doi/abs/10.1029/2007GL031960 doi: https://doi.org/10.1029/2007GL031960

Hemmingway, D., Nimmo, F., Zebker, H., & Iess, L. (2013). A rigid and weathered ice shell on Titan. *Nature*, *500*, 550-552. doi: https://doi.org/10.1038/nature12400

Hendrix, A. R., Hurford, T. A., Barge, L. M., Bland, M. T., Bowman, J. S., Brinckerhoff, W., ... Vance, S. D. (2019). The NASA roadmap to ocean worlds. *Astrobiology*, *19*(1), 1-27. Retrieved from https://doi.org/10.1089/ast.2018.1955 (PMID: 30346215) doi: 10.1089/ast.2018.1955

Hopfield, H. S. (1971). Tropospheric effect on electromagnetically measured range: Prediction from surface weather data. *Radio Science*, *6*(3), 357-367. Retrieved from https://agupubs.onlinelibrary.wiley.com/doi/abs/10.1029/RS006i003p00357 doi: https://doi.org/10.1029/RS006i003p00357

Iess, L., Di Benedetto, M., James, N., Mercolino, M., Simone, L., & Tortora, P. (2014). Astra: Interdisciplinary study on enhancement of the end-to-end accuracy for spacecraft tracking techniques. *Acta Astronautica*, *94*(2), 699 - 707. Retrieved from http://www.sciencedirect.com/science/article/pii/S0094576513002014 doi: https://doi.org/10.1016/j.actaastro.2013.06.011

Iess, L., Jacobson, R., Ducci, M., Stevenson, D., Lunine, J., Armstrong, J., ... Tortora, P. (2012). The tides of Titan. *Science*, *337*(6093), 457-459. doi: 10.1126/science.1219631

Iess, L., Militzer, B., Kaspi, Y., Nicholson, P., Durante, D., Racioppa, P., ... Zannoni, M. (2019). Measurement and implications of Saturn's gravity field and ring mass. *Science*, *364*(6445). doi: 10.1126/science.aat2965

Iess, L., Rappaport, N., Jacobson, R., Racioppa, P., Stevenson, D., Tortora, P., ... Asmar, S. (2010). Gravity field, shape, and moment of inertia of Titan. *Science*, *327*, 1367-1369. doi: 10.1126/science.1182583

Kaula, W. (1966). *Theory of satellite geodesy.* A: Blaisdell Publishing Company. (Waltham, MA, US)

Kramm, U., Nettelmann, N., Redmer, R., & Stevenson, D. (2010). On the degeneracy of the tidal Love number k_2 in multi-layer planetary models: application to

Saturn and GJ 436b. *Astronomy & Astrophysics*, *528*(A18), 7.

Krogh, F. T., NG, E. W., & Snyder, W. V. (1982). The gravity field of a disk. *Celestial Mechanics*, *26*, 395-405.

Kronrod, V., Dunaeva, A., Gudkova, T., & Kuskov, O. (2020). Matching of models of the internal structure and thermal regime of partially differentiated Titan with gravity field. *Solar System Research*, *54*, 405-419. doi: https://doi.org/10.1134/S0038094620050044

Lemoine, F. G. R., Goossens, S., Sabaka, T. J., Nicholas, J. B., Mazarico, E., Rowlands, D. D., ... Zuber, M. T. (2013). High–degree gravity models from GRAIL primary mission data. *Journal of Geophysical Research: Planets*, *118*(8), 1676-1698. Retrieved from `https://agupubs.onlinelibrary.wiley.com/doi/abs/10.1002/jgre.20118` doi: https://doi.org/10.1002/jgre.20118

Lemoine, F. G. R., Smith, D. E., Zuber, M. T., Neumann, G. A., & Rowlands, D. D. (1997). A 70th degree lunar gravity model (GLGM-2) from Clementine and other tracking data. *Journal of Geophysical Research: Planets*, *102*(E7), 16339-16359. Retrieved from `https://agupubs.onlinelibrary.wiley.com/doi/abs/10.1029/97JE01418` doi: https://doi.org/10.1029/97JE01418

Liu, A. (1974). Range measurements to Pioneer 10 using the digitally cmtrolled oscillator. *The Deep Space Network*, 63.

Mazarico, E., Genova, A., Goossens, S., Lemoine, F., Neumann, G., Zuber, M., ... Solomon, S. (2014). The gravity field, orientation, and ephemeris of Mercury from MESSENGER observations after three years in orbit. *Journal of Geophysical Research: Planets*, *119*, 2417-2436. doi: 10.1002/2014JE004675

McCarthy, J., Rowton, S., Moore, D., Pavlis, D., Luthcke, S., & Tsaoussi, L. (2015). *GEODYN system description volume 1.* NASA GSFC.

McMahon, J., Scheeres, D., Farnocchia, D., & Chesley, S. (2015). Understanding Kaula's rule for small bodies. *American Geophysical Union*.

Meriggiola, R., Iess, L., Stiles, B., Lunine, J., & Mitri, G. (2016). The rotational dynamics of Titan from Cassini RADAR images. *Icarus*, *275*, 183 - 192. Retrieved from `http://www.sciencedirect.com/science/article/pii/S0019103516000300` doi: https://doi.org/10.1016/j.icarus.2016.01.019

Murray, C., & Dermott, S. (1999). *Potential theory in gravity and magnetic applica-*

tions. Cambridge University Press.

NASA PDS, t. P. A. N. (2020). *Planetary Data System.* Retrieved from https://pds-atmospheres.nmsu.edu/data_and_services/atmospheres_data/Cassini/Cassini/DOCS\%20for\%20events\%20&\%20Configuration\%20page/Small\%20Forces/

Niell, A. E. (1996). Global mapping functions for the atmosphere delay at radio wavelengths. *Journal of Geophysical Research: Solid Earth*, *101*(B2), 3227-3246. Retrieved from https://agupubs.onlinelibrary.wiley.com/doi/abs/10.1029/95JB03048 doi: https://doi.org/10.1029/95JB03048

Sohl, F., Hussmann, H., Schwentker, B., & Spohn, T. (2003). Interior structure models and tidal Love numbers of Titan. *Journal of geophysical research*, *108*(E12, 5130). doi: 10.1029/2003JE002044

Tapley, B., Schutz, B., & Born, G. (2004). *Statistical orbit determination*. Elsevier.

Thornton, C. L., & Border, J. S. (2003). *Radiometric tracking techniques for deep-space navigation*. John Wiley & Sons.

Tyler, R. (2014). Comparative estimates of the heat generated by ocean tides on icy satellites in the outer solar system. *Icarus*, *243*, 358-385. doi: 10.1016/j.icarus.2014.08.037

3

Supplementary Materials

These are the supplementary materials belonging to the article "*Titan's gravity field from Cassini Doppler Tracking Data*" by van Noort et al. This document provides an extensive description of the implemented dynamic model (Section 3.1), including, among others, a summary of flyby properties, explanations on implemented forces, estimated parameters, their *a priori* values, the applied constraints on parameters, and the applied arc weights. Section 3.2 provides a summary and conclusions of a sensitivity analysis performed on the parameter constraints. Section 3.3 illustrates the effect of different implemented arc weights, investigating the robustness of the applied arc weights. Finally, Section 3.4 discusses the plots of the observation residuals for every arc, including possible improvements.

3.1. Methodology

The estimation of Titan's gravity field is based upon Doppler radio tracking data from ten flybys with tracking of the satellite at the time of closest approach (C/A). Table 3.1 summarizes these ten flybys during which Doppler tracking is performed at C/A obtained with the SpiceyPy package [Annex et al., 2020]. These properties are valid for the point of C/A of the flyby. The Sun-Earth-Probe (SEP) angle is important for the determination of the Doppler noise in the radio signal caused by solar plasma turbulence [Asmar et al., 2005, Iess et al., 2014]. If the signal would travel close to the Sun, significant solar plasma noise is introduced. This is more relevant for X-band data (analyzed in this article) compared to Ka-band data due to the lower transmission frequency of X-band frequencies [Asmar et al., 2005, Iess et al., 2014]. The indicated RMS of the observation residuals shown in Table 3.1, corresponds to the post-fit of the observations with the baseline dynamic force model.

The program GEODYN II is utilized for the orbit determination of Cassini and gravity analysis of Titan, by performing arc iterations (specified below). This software package was designed and maintained by NASA GSFC and has been used numerous times in the past. It was initially designed for Earth applications, but later

Table 3.1: Summary of all flybys used in the analysis of Titans gravity field. The altitude, longitude and latitude are shown for the point of C/A of the flybys. The Sun-Earth-Probe angle is important to determine the Doppler noise caused by solar plasma turbulence [Asmar et al., 2005, Iess et al., 2014]. Most values are computed with the SpiceyPy toolkit [Annex et al., 2020], similar to Acton et al. [2017].

Flyby	C/A date (UTC) (yy-mm-dd hh:MM)	Altitude (km)	Longitude ($°E$)	Latitude ($°N$)	SEP (°)	Observations (at 10s)	RMS of the residuals (mHz)
T011	06-02-27 08:25	1812	253.7	0.34	147.0	3233	5.462
T022	06-12-28 10:05	1297	4.2	40.9	131.9	4858	4.682
T033	07-06-29 17:00	1933	66.6	9.3	44.6	4075	5.676
T045	08-07-31 02:13	1614	165.3	-42.7	29.4	12736	4.104
T068	10-05-20 03:24	1398	245.0	-49.8	118.8	8674	3.801
T074	11-02-18 16:04	3651	116.3	-0.3	132.9	9162	9.952
T089	13-02-17 01:56	1978	205.5	20.0	107.0	13245	1.833
T099	14-03-06 16:27	1500	182.6	-32.6	112.7	10064	5.117
T110	15-03-16 14:30	2274	268.5	75.1	110.8	7244	4.296
T122	16-08-10 08:31	1698	235.7	11.7	111.7	10163	5.237

on extended to be used for the orbit determination of satellites orbiting other celestial bodies as well [Goossens and Matsumoto, 2008, Mazarico et al., 2014, Mazarico, 2004]. However, the Saturnian system with its many moons with significant masses was the first complex planetary system analyzed with GEODYN II. Calculation of the gravity forces acting on the satellite, arising from the presence of these significantly heavy moons, had to be verified.

The moons Mimas, Enceladus, Tethys, Dione, Rhea, Hyperion, and Iapetus are included as point mass disturbances. The positions of the eight heaviest moons is updated inside GEODYN II by an eighth order Langrange polynomial fit through data generated by SPICE [Acton et al., 2017] and most recent satellite-planet kernel (SPK) from NASA JPL.[1] The position of Saturn is updated through a similar procedure and included as perturbing third body as well. All other planetary systems are included as third body point mass disturbances. For barycentric positions of other planetary systems, the DE432 kernel from NASA JPL is used.

The dynamic model for integration of the orbit of the Cassini spacecraft includes several forces, all of which are listed in the main article. To improve reproducibility, further explanation and information may be necessary on certain forces and estimated parameters, especially those which are not included in previous research (e.g. gravity of Saturn's rings).

The Radioisotope Thermo-electric Generators (RTG) generate a thermal thrust on the Cassini spacecraft. The *a priori* magnitudes of these RTG contributions are taken from Bertotti et al. [2003]. Radio-active decay of the ^{238}Pu source, with a half-life of 87.74 years, is also considered. As a result, the magnitude given in Bertotti et al. [2003] will decay with a half-life of 87.74 years, which has been accounted for when computing the *a priori* conditions of the RTG accelerations. This lead to several different initial conditions given to the RTG accelerations for every arc/flyby. We multiply this force by a scale factor, one for every direction x, y and z. The scale factor is estimated in the orbit determination process, and initialized to be 1.0. The x- and y-direction of the RTG acceleration in the spacecraft body fixed coordinate frame are given an *a priori* uncertainty of 100%, while the z-direction is given an *a priori* uncertainty of 50%, equivalent to the uncertainties in Bertotti et al. [2003].

The solar radiation pressure force is included, estimating a solar radiation coefficient with an *a priori* uncertainty of ∼10% of its initial magnitude. A simple box-wing panel model is used, which approximates the Cassini model as a rectangular box with a slender boom approximating the magnetic boom. The areas in Cassini's body-fixed coordinate frame are 27.49 m^2, 17.49 m^2, and 18.16 m^2 in the x-, y-, and z-direction, respectively. The same model was used to calculate drag on the spacecraft for every arc, subsequently estimating a drag coefficient. The Titan GRAM atmosphere model was used to calculate the drag on the spacecraft (see Duvall et al. [2005]).

Due to attitude corrections and desaturation of the reaction wheels, the Cassini spacecraft consumes fuel during the mission, thereby decreasing in mass. Hence, the spacecraft mass is different for every flyby, and GEODYN II was given the correct mass during a specific flyby.[2]

As noted in the article, gravity accelerations due to the Saturnian A, B and C ring masses are also included in the dynamic force model of the spacecraft. The masses of these rings are 0.15, 0.23, and 0.024 times the mass of Mimas ($\mu_{Mimas} = 2.5026$ km^3/s^2), respectively. The contribution of a ring with gravitational parameter μ_r is:

$$\ddot{\mathbf{r}}_b = 2\mu_r \left(\ddot{\mathbf{r}}_d(2) - \ddot{\mathbf{r}}_d(1)\right) / \left(\pi\left(\rho_2^2 - \rho_1^2\right)\right). \tag{3.1}$$

where the equation for $\ddot{\mathbf{r}}_d(i)$ is found in the article. The parameter R is the magnitude of $\mathbf{r}_b$ equal to $\sqrt{x_b^2 + y_b^2 + z_b^2}$, r is $\sqrt{x_b^2 + y_b^2}$, $K(x)$ and $E(x)$ are the complete elliptic integrals of the first and second kind, respectively. In addition, $F(\theta, k)$ and $E(\theta, k)$ are the incomplete elliptic integrals of the first and second kind (see e.g. Prasolov and Solovyev [1997] for a description of these elliptic integrals). To compute $\ddot{\mathbf{r}}_d(i)$, the following parameters need to be computed for the disk with radius ρ_i:

$$\begin{aligned}
D_i &= \left(R^2 + \rho_i^2 + 2r\rho_i\right)^{1/2} \\
k_i &= \left(4r\rho_i\right)^{1/2} / D_i \\
k_i' &= \left(1 - k_i^2\right)^{1/2} \\
\theta_i &= \tan^{-1}\left(|z_b / (r - \rho_i)|\right) \\
f_{2i} &= \left(1 - 1/2k_i^2\right) K(k_i) - E(k_i) \\
f_{3i} &= \left(E(k_i) - K(k_i)\right) F\left(\theta_i, k_i'\right) + K(k_i)\, E\left(\theta_i, k_i'\right)
\end{aligned}$$

[1] filename 180628RU_SCPSE_04183_17258 from `https://naif.jpl.nasa.gov/pub/naif/CASSINI/kernels/spk/`

[2] see e.g. `https://pds-atmospheres.nmsu.edu/data_and_services/atmospheres_data/Cassini/eng-overview.html` for mass history of the Cassini spacecraft

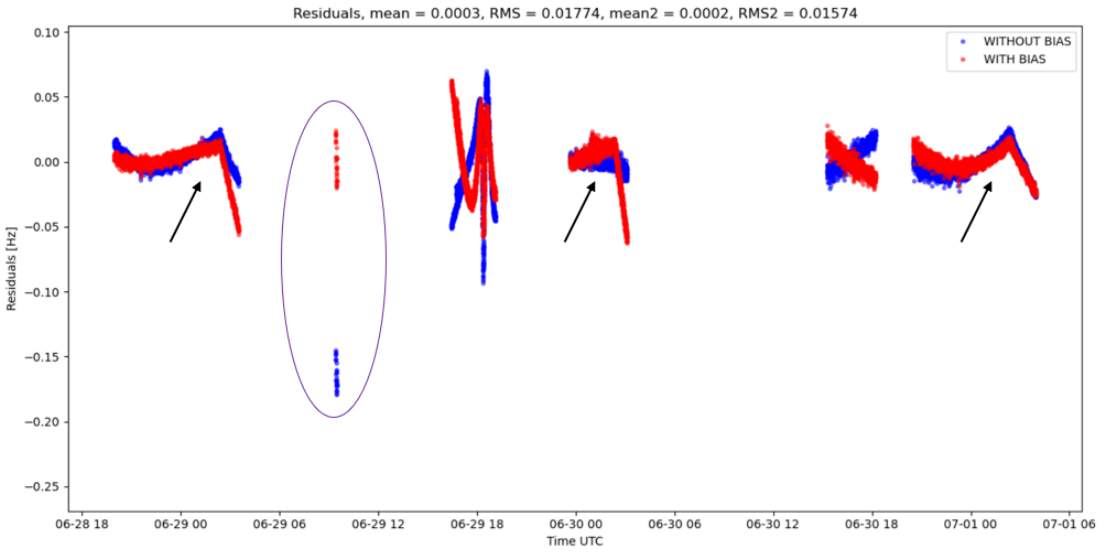

Figure 3.1: The effect of the estimation of observation biases, indicated by the purple ellipse. The observation bias filters out signal from the residuals such that the mean of the residuals lies around zero. Note also that the mean and RMS of the bias solution (mean2 and RMS2 from the title) are lower than the mean and RMS of the solution without observation biases, as expected. The black arrows indicate the start and end times of sets of empirical accelerations. Ending a period of a set of empirical accelerations during a data pass should be avoided as it introduces signal as shown.

Together with the equation for $\ddot{\mathbf{r}}_d(i)$, the acceleration on the spacecraft can be calculated from a ring with mass μ_r using Equation 3.1.

In order to run the GEODYN II orbit determination program, initial conditions of the parameter set and constraints are needed. In Table 3.2, all the initial conditions and applied constraints (if applicable) are shown. Initial conditions for the Cassini state vector are taken from the latest version of the SPK file[1] from the navigation team at NASA/JPL, which differ per flyby. Start and end dates of the arc usually span a period between 1.0 and 2.0 days, as shown in Table 3.3.

Empirical accelerations are estimated in radial, along- and cross-track directions for periods of approximately eight hours. Note that most lengths of the flybys are not divisible by eight hours, resulting in occasionally lower or higher estimation periods. In addition, attention is paid to when these empirical acceleration periods start and end: it is not desirable to end such period in the middle of an observation pass, as this introduces undesired signals in the observation residuals (Figure 3.1). These empirical accelerations are constrained tightly, as applying loose constraints results in a lot of the signal being absorbed by the empirical accelerations, which should be avoided. Magnitudes of these empirical accelerations vary between $10^{-6} - 10^{-9}$ m/s^2.

By comparing converged estimation of the entire parameter set, both with and without the estimation of station observation biases, it was found that these observation biases are necessary in the estimation process. Figure 3.1 illustrates this effect by plotting the residuals of an arc with and without station observation biases. This bias can be caused by several modeling errors, such as frequency offsets, discrepancies in station locations, and mismodeling of the effect of Earth's atmosphere on the observations [Lemoine et al., 1997]. In addition, a bias can be introduced in the residuals by an imprecise position of Titan, an issue resolved in previous research by estimating Titan's initial position at the start of the arc directly [Durante et al., 2019]. The estimated observation bias is expected to mitigate this effect in a similar fashion. Hence, the estimation of station observation biases filters out most undesired signal in the residuals (Figure 3.1). Note that the station observation biases are estimated for every station - satellite combination. Every arc will have a different number of ground station - satellite combinations and this directly influences the number of station observation biases estimated. Additionally, a new observation bias will be estimated for data from the same ground station - satellite combination if the data belong to different passes separated by at least 20 mins, i.e. there is a data gap in the observations of at least 20 mins. The total number of estimated station observation biases is 59 and can be deduced from the residual plots for every arc (Section 3.4). Observation biases are constrained quite severely (Table 3.2), as these could potentially absorb much of the signal in a similar fashion as the empirical accelerations.

Table 3.2: Constraints applied to all parameters in the inversion process during global iterations. Most of these constraints are also used in arc iterations (when utilizing GEODYN II), except for the RTG scale biases and global parameters.

Parameter	**A priori value**	**A priori constraint**
$\mathbf{X}_{Cassini}$ [km]	SPICE[1]	2.0
$\mathbf{V}_{Cassini}$ [cm/s]	SPICE[1]	2.0
C_D [-]	2.4	1.0
C_R [-]	1.15	0.1
Empirical accelerations [m/s^2]	0.0	$1.0 \cdot 10^{-7}$
Observation biases [Hz]	0.0	$1.0 \cdot 10^{-2}$
RTG scale biases [-]	1.0	1.0 (x,y), 0.5 (z)
Antenna offset [m]	(0.0, 0.0, -3.0)	(2.0, 2.0, 2.0)
Global Parameters		
Spherical harmonics [-]	0.0	-
k_2 [-]	0.0	-
μ [km^3/s^2]	8978.138	-

[1] From the most recent SPK file

Table 3.3: Begin and end times of the arcs for all the flybys, including the total length expressed in days. The indicated applied weight is applicable to the baseline solution.

Arc (Flyby)	**Begin (UTC)**	**End (UTC)**	**Length (days)**	**Applied Weight**
T011	27-Feb-06 00:15:00	28-Feb-06 00:00:00	0.99	0.5
T022	27-Dec-06 04:55:00	28-Dec-06 23:00:00	1.75	3.0
T033	29-Jun-07 10:00:00	30-Jun-07 19:00:00	1.38	1.5
T045	30-Jul-08 12:00:00	31-Jul-08 22:00:00	1.42	2.5
T068	19-May-10 16:00:00	20-May-10 22:00:00	1.25	1.5
T074	18-Feb-11 02:00:00	19-Feb-11 10:00:00	1.33	1.0
T089	16-Feb-13 00:30:00	17-Feb-13 18:00:00	1.73	1.5
T099	06-Mar-14 03:00:00	07-Mar-14 08:00:00	1.21	3.5
T110	15-Mar-15 14:00:00	16-Mar-15 21:00:00	1.29	1.5
T122	09-Aug-16 18:00:00	11-Aug-16 10:00:00	1.67	1.5

In arc iterations, the RTG scale bias constraints are a factor of ten smaller than they are in global iterations, as in arc iterations these tend to correlate a lot with empirical accelerations. If a constraint on the RTG scale bias is too loose, the sign of the scale bias could flip, which we know from previous research on the RTG acceleration to be incorrect with high certainty (see for example Benedetto [2010-2011], Bertotti et al. [2003]).

The positions of the antenna with respect to the center of mass are also estimated during all flybys. These estimations are equivalent to estimating a center of mass of the spacecraft. Due to fuel consumption during the mission, the mass decreases and consequently the center of mass changes. Any signal caused by a rotation of the satellite around its center of mass should be filtered out in the Doppler residuals, which is achieved by estimating an antenna position. The initial condition of the antenna position was set to be at -3.0 meters in the body fixed z-direction (and zero in the other two directions), as this is approximately where the High Gain Antenna (HGA) is mounted. Since the offset is estimated, it does not matter where the HGA is located precisely, as long as a good initial estimate is given as initial condition. Flyby T110 was devoted to imaging the North Polar lakes of Titan, with the Doppler measurements being acquired using the omnidirectional Low Gain Antenna (LGA), for which a position needs to be estimated as well, similar to estimating the position of the HGA. The estimation of the LGA position is concurrently included in the estimation of the center of mass/antenna offsets, identical to the center of mass estimations for the other flybys.

Note that for the global parameters, the initial conditions for the determination of the 3x3 gravity field solution (baseline) are obtained by first estimating a converged 2x2 gravity field initialized at zero. For the analysis of the robustness of the solution from previous research (Section 3.2 in the article), we took the initial conditions of the gravity field to be equal to those from Durante et al. [2019]. Note that degree four and five spherical harmonics are included in the estimation process for this stability analysis. In addition, we did not use any constraints on global

parameters. This approach is different from Iess et al. [2012] and Durante et al. [2019]. In Durante et al. [2019] it is mentioned that *all* parameters are given constraints, with constraints on global parameters not influencing (i.e. constraining) the solution. As noted, we refrain from the application of these non-physical global constraints, as we cannot properly determine their validity.

As mentioned in the article, the gravity determination process will be split into two parts: arc and global iterations. First, the GEODYN II program performs an iterative weighted least squares approximation, with constraints on the arc parameters as depicted in Table 3.2, except for the RTG scale bias as explained before (which has ten times tighter constraints), and the global parameters (as these are constrained tightly during these arc iterations). After convergence, GEODYN II calculates the design matrix of every arc, from which it computes a normal matrix for every arc given the observation weight matrix. Applied weights of the observations are 0.028 Hz (∼1.0 mm/s in X-band frequency transmission). Finally, all normal matrices and residual vectors are combined into one large multi-arc normal matrix and residual vector with the applied weights as outlined in the article. The combined normal matrix contains information on all the estimated parameters, which per flyby are: six Cassini state parameters, a C_R and C_D coefficient, three RTG scale biases (x-, y-, and z-direction), and antenna coordinates in the body fixed frame. Empirical accelerations in radial, along- and cross-track direction are estimated for every period of eight hours and depends on the arc-length. Station biases are estimated for every pass with gaps of 20 minutes or longer, and for every different ground station - satellite configuration. A total of 128 empirical accelerations and 59 observation biases are estimated. On top of the arc parameters, 12 spherical harmonic gravity coefficients (degree two and three) and the gravitational parameter, μ, are estimated; the combined normal matrix therefore contains information on the 340 estimated parameters.

3.2. Sensitivity analysis

A sensitivity analysis was performed to determine the sensitivity of a change in the applied constraint for all parameters. We took a set of constraints, either from previous research [Durante et al., 2019], or constraints in the order of the estimated parameter. The solution corresponding to this set of constraints (the reference solution) is calculated. Then, the constraint of one parameter is altered by multiplying it by a factor of ten, after which a new solution is determined with only this constraint altered. This is done for every parameter and all the solutions are compared to the reference solution. The altered solutions are ranked by the norm of their difference from the reference solution. The most sensitive parameters are the ones which have the largest difference with the reference solution. This same procedure is repeated once more, but by decreasing the constraint by a factor of ten. With these two approaches, we can observe which parameters respond most sensitive to a change of the applied constraint.

The sensitivity analysis has given insight into the most sensitive parameters: empirical accelerations and state parameters. From both methods (increasing and decreasing the constraint by a factor of ten), the 30 most sensitive parameters are investigated. If the constraints are decreased, the empirical accelerations become most sensitive (18 of 30 top sensitive parameters are empirical accelerations) and they absorb more signal from the observation residuals. This leads to a substantially different solution of the estimated parameter set. They are generally less correlated with other parameters, than other parameters are. As a result of mismodeled forces, a tight constraint on the empirical acceleration leads to an ill fit of the observation residuals, not yet in the order of the expected noise level. If the constraint is made tighter, the empirical accelerations are underrepresented in the 30 most sensitive parameters (eight parameters are empirical accelerations). Hence, the applied constraints for the empirical accelerations is found to be better for the reference solution, as that constraint lies between a tight and loose constraint (Table 3.2).

A similar result was found for the state parameters. Applying a ten times tighter constraint resulted in seven sensitive state parameters, whereas loosening the constraint resulted in 21 sensitive state parameters (out of 30). The reference constraint was 2.0 km and 2.0 cm/s for the position and velocity of Cassini, respectively, also adopted in Durante et al. [2019]. The *a priori* condition of Cassini is known with a certain accuracy from the ephemeris files from the Navigation team of JPL. This accuracy is better than the applied reference constraints. A constraint ten times smaller than the reference constraint is not preferred as the adjustment to the state would be beyond the expected accuracy of the ephemeris files.

An alternative sensitivity analysis, the principal component analysis (PCA), was performed to determine which parameters explain most variance in the solution of the parameter set. The PCA sheds light on the parameters which influence the solution the most: excluding these parameters from estimation results in a significantly different estimate of the overall solution. In essence, this illustrates which parameters can be estimated quite well given the data. Indeed, if the data do not contain (sufficient) information on the estimation of a certain parameter,

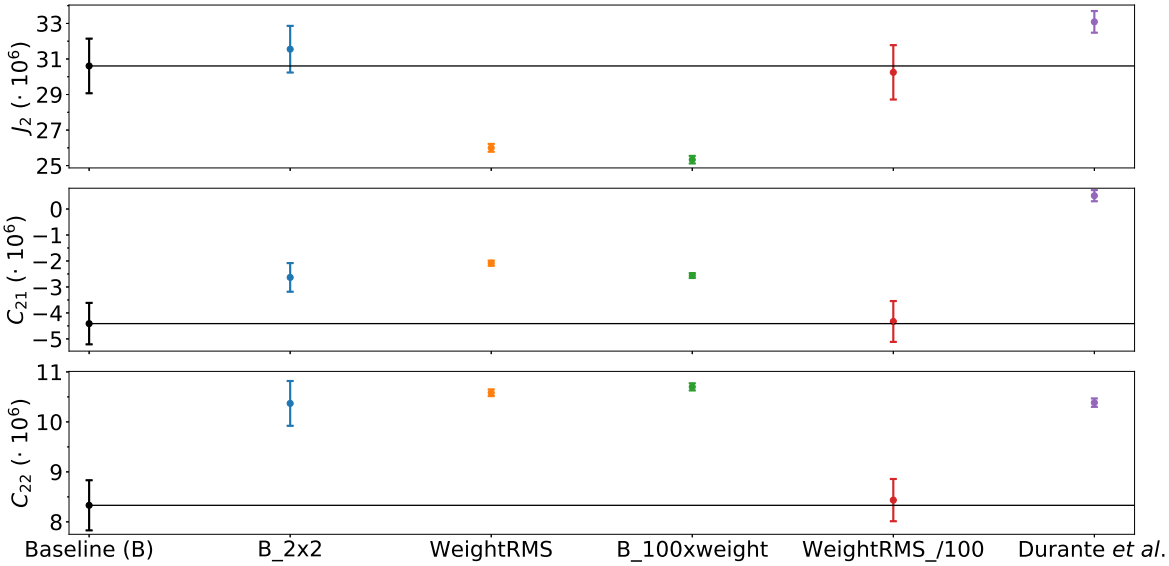

Figure 3.2: Solutions of the unnormalized second degree C coefficients of the gravity field, implementing different models and applying different constraints, see Table 3.4. The solution of Durante et al. [2019] is plotted as well to illustrate which solution most conforms with previous research.

this parameter cannot cause a lot of variance in the solution as, according to the data, the contribution of this parameter is (almost) negligible. For the determination of parameters which cause substantial variance in the solution (PCA), also the spherical harmonic gravity coefficients of degree four and five are included.

The PCA determines the principal components which each cause a certain percentage of the variance in the solution [Jolliffe and Cadima, 2016, Lay, 2012]. In theory, there are as many principal components as there are parameters, though the first ten principal components contribute to 99.99% of the variance in the solution and are hence considered. Within these principal components, the empirical accelerations have the largest contribution as expected: a solution without empirical accelerations was attempted but yielded no feasible solution. Most importantly, several global parameters are found to cause substantial variance in the solution as well. It is expected that global parameters influence the solution most, as these parameters apply to every flyby/arc and influence the estimation of all parameters, including arc-specific parameters. Therefore, it is expected that global parameters cause substantial variance in the solution to the estimated parameter set. As noted, if a parameter is found to cause substantial variance in the solution, the data contain sufficient information on this parameter to allow for its estimation. Global parameters which are found to cause substantial variance in the solution are C_{20}, C_{22}, C_{31}, S_{21}, S_{22}, S_{31}, S_{42}, and S_{52}. Hence, these coefficients are well supported by the data. Note that not a lot of spherical harmonic coefficients from degree four and five are found to cause substantial variance in the solution, supporting our method of estimating only a lower degree field (3x3).

3.3. Comparison with other models

To check the robustness of the solution, the influence of the applied constraints and given weights to flybys, solutions of the C_{2m} coefficients implementing different weights are presented in Figure 3.2. The solution from Durante et al. [2019] for these coefficients is also plotted.

A description of these different models is given in Table 3.4. From Table 3.3, the applied arc weights of the flybys for the baseline solution can be found. These weights are all in the same order of magnitude and between 1 and 5. Commonly in the field of orbit determination, the weights of arcs are applied according to the RMS of the observation residuals, as the RMS is an indication for the noise level of the observations. Durante et al. [2019] also applied weights to the arcs according to their post-fit RMS of the residuals. If we would apply weights accordingly as 1/RMS of the observations (Table 3.1) for every flyby, we would obtain weights in the order of 100-500 (the RMS is in the order of mHz), which is 100 times larger than the weights of the baseline solution (Table 3.3). Of course, this has significant impact on the solution: from the explanation about the inversion process (Equation 5 in the article), it is obvious that this would mean that the normal matrices are weighted a factor of 100 larger compared to the baseline solution. For this reason we also analyse two additional models: one with

Table 3.4: Description of the models in Figure 3.2.

Baseline	Baseline model: discussed in Processing section in the article. Weights are indicated in Table 3.3.
B_2x2	Baseline model with 2x2 spherical harmonic expansion of the gravity field instead of 3x3 expansion.
WeightRMS	Baseline model, instead with applied arc weights based on 1.0/rms of the arc; comparable to Durante et al. [2019].
B_100xweight	Baseline model with weights of the arcs (Table 3.3) multiplied by 100.
WeightRMS_/100	WeightRMS model where weights are divided by 100 to get them in the same order of magnitude as the coverage based weights of the baseline model (Table 3.3)

applied weights based on RMS divided by 100 (WeightRMS_/100), and one with weights of the baseline method multiplied by a factor of 100 (B_100xweight). This is, of course, done to better compare the different solutions of different methodologies of applying weights.

Clear conclusions can be drawn from the plot in Figure 3.2. As pointed out in the article, the applied constraints have tremendous impact on the final solution. For the solutions WeightRMS and B_100xweight, the weights are in the order of 100-500, where we see that their mutual results are close. Applying a larger weight to the arcs, without rescaling the weights of the constraints (1.0 for the baseline solution, see Equation 6 in the article), yields significantly different solutions. Applying such a large weight is equivalent to giving more weight to the observations, and the results in Figure 3.2 further stress the influence of the application of constraints and their respective weights. In addition, there exist significant differences in terms of the formal error for these two models, compared to the other models. The formal errors are calculated with Equation 7 in the article. Immediately, we observe that once the weights G_i (hence N_{tot}) become larger in this equation, the formal error goes down. This is not surprising, as in these models, the constraints (i.e. *a priori* uncertainties) are given a much smaller weight, with observations weighted heavier.

Model B_2x2 shows the solution of the baseline model having implemented a 2x2 gravity field. The estimated parameters J_2 and C_{21} differ insignificantly compared to the baseline solution, whereas C_{22} does not. The coefficient C_{22} is actually very close to the value determined by Durante et al. [2019] with the obtained 2x2 solution. This can be expected to happen: by not estimating higher degree coefficients, signal originating from those higher degrees will have to be absorbed in part by the lower degrees, inevitably leading to a different estimate for the lower degree parameters. Unfortunately, the higher degrees are not sampled equally well as a result of poor orbit geometry and lack of data. Hence, simply including higher degrees leads to over-compensation of these estimated higher degrees, resulting in large estimates of the higher degree coefficients [Kaula, 1966, Mazarico, 2004]. A Kaula constraint is commonly included to mitigate this effect [Kaula, 1966], though not implemented in this analysis as no knowledge on the underlying power distribution of the coefficients per degree is available for Titan yet [Durante et al., 2019].

Comparing the baseline model with the WeightRMS_100 model, two insignificantly different solutions are obtained. This emphasizes the fact that the baseline solution is stable in terms of the applied, respective weights on flybys, given that the order of magnitude of the applied weight remains the same. In other words, if the *a priori* constraints are given weights in the same order of magnitude relative to the observations, the obtained solution is statistically insignificant. This illustrates that the weights for the baseline solution (Table 3.3) give similar gravity solutions compared to solutions where the applied weights would be inversely proportional to the noise RMS of the residuals.

Finally, compared to the solution from previous research [Durante et al., 2019], we observe that the baseline solution with a spherical harmonic expansion of the gravity field of degree two best fits their results. There still exists a large difference in the coefficient C_{21} however, which can be caused by the difference in the applied constraint on this parameter. The calculated formal errors for our baseline 2x2 solution are still substantially larger than their solution, which is directly caused by our lower weights applied to the arcs.

3.4. Fit of the residuals

The residual plots for the post-fit estimation of the gravity field, with the implemented baseline model discussed in Section 2 of the paper, are shown in this section. As indicated in Table 3.1, the RMS of the residuals is in the

order of the noise level. The residual plots in this section show the RMS values of the observation residuals at the top of every plot, together with the mean, for all analyzed flybys.

The residual plots contain all Doppler tracking data analyzed in the gravity determination process (X-band). The time period therefore corresponds with the arc span of every arc. Even though the RMS of the residuals is within the expected noise level (<1.0 mm/s), the residuals still contain some signal. This suggests that the dynamic model is still not entirely complete. Most of the signal happens near the closest approach (Table 3.1), suggesting that particular parameters specific for Titan are not estimated or included in the dynamic model. These could be higher order spherical harmonic coefficients of the gravity field, as well as the k_2 Love number. However, inclusion of the estimation of these parameters did not result in feasible solutions, both for the gravity field and the Love number, due to aforementioned correlations between global parameters. Estimation of these parameters is expected to filter out some of the remaining signal, but that means that the correlations have to be resolved before being able to do so.

For low altitude flybys, the drag plays a significant role as well. For these flybys it might be interesting to investigate the effect of increasing the allowed variance (decreasing the constraint) on the estimated drag coefficient. It is possible that the drag coefficients are constrained too tightly for these flybys. On the other hand, the drag correlates with empirical accelerations in the along-track direction, and it is hence expected that mismodeled drag forces are absorbed by these accelerations. Nevertheless, the effect of decreasing the constraint on the drag coefficient will be further investigated as it could absorb the signal in the residuals.

The DSN-CAS combinations in the legend of every plot indicate the configuration of the satellite and ground station for that particular observation pass. The configuration consists of four numbers separated by a dash. The first two numbers are integer codes indicating which ground stations are used for the signal link. These integer codes are unique for every ground station from the Deep Space Network (DSN). The first integer is the transmitting ground station and the second integer is the receiving ground station. Hence, if the first and second integer codes are the same, the data are two-way data. If these two integer codes are different, then the data are three-way data. The third and fourth numbers are integer codes unique for every satellite. In this case, we are only dealing with one satellite: Cassini with integer code 1997288. The third number in the configuration indicates the receiving satellite which received the signal from the first transmitting ground station. The fourth number indicates the satellite which received the signal from the second ground station. Note that for three-way data, this is always 0 as there is no satellite which received the signal transmitted by the receiving ground station, as that ground station only received the re-transmitted signal by the satellite.

For example, 34-25-1997288-0 corresponds to three-way data first transmitted by DSN station 34, received and re-transmitted by satellite 1997288 (Cassini), and received again by DSN station 25. The signal received at station 25 was not initially transmitted by DSN station 25, hence the fourth number is 0. The configuration 25-25-1997288-1997288 would correspond to two-way data transmitted by DSN station 25, received and re-transmitted by Cassini, and received at DSN station 25 again.

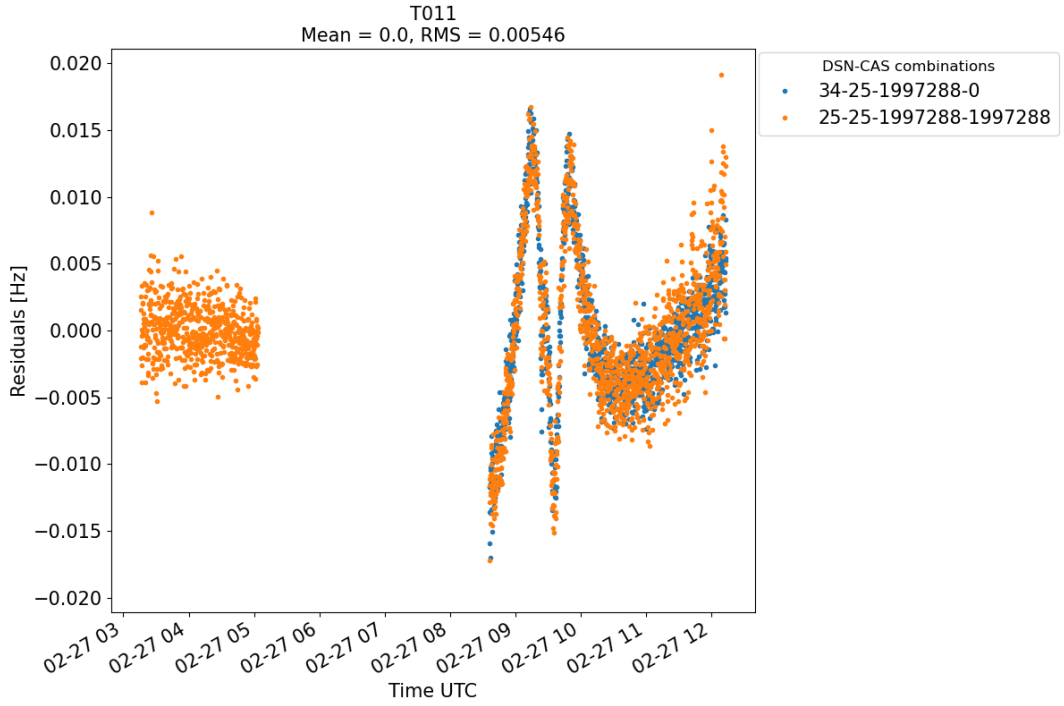

Figure 3.3: Residual plot of T011.

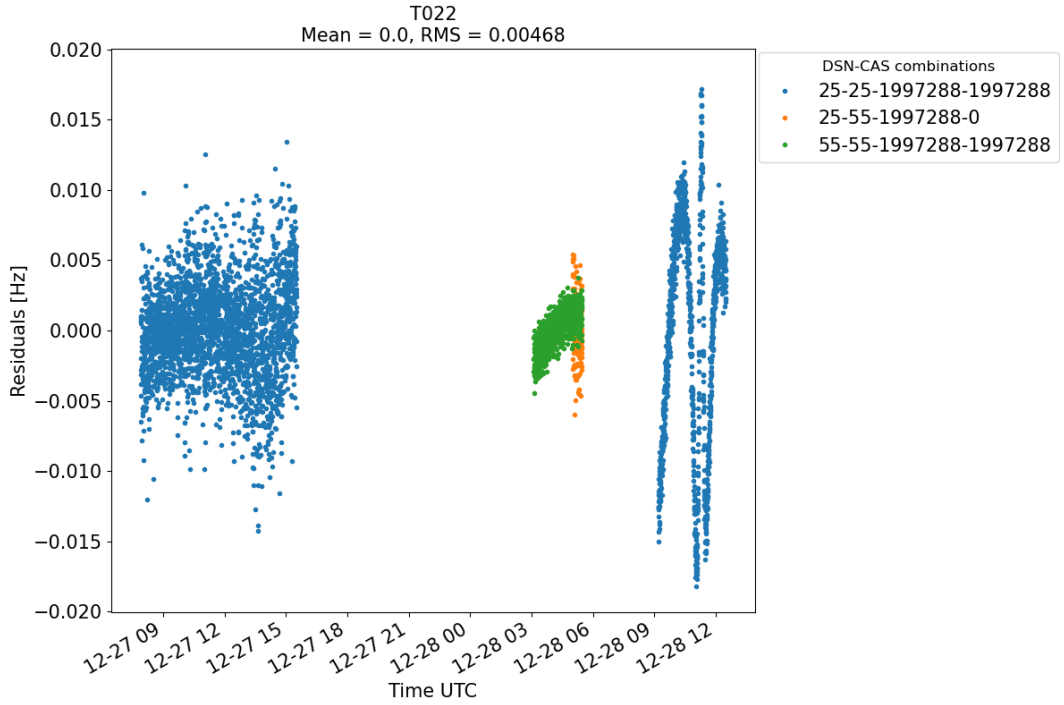

Figure 3.4: Residual plot of T022.

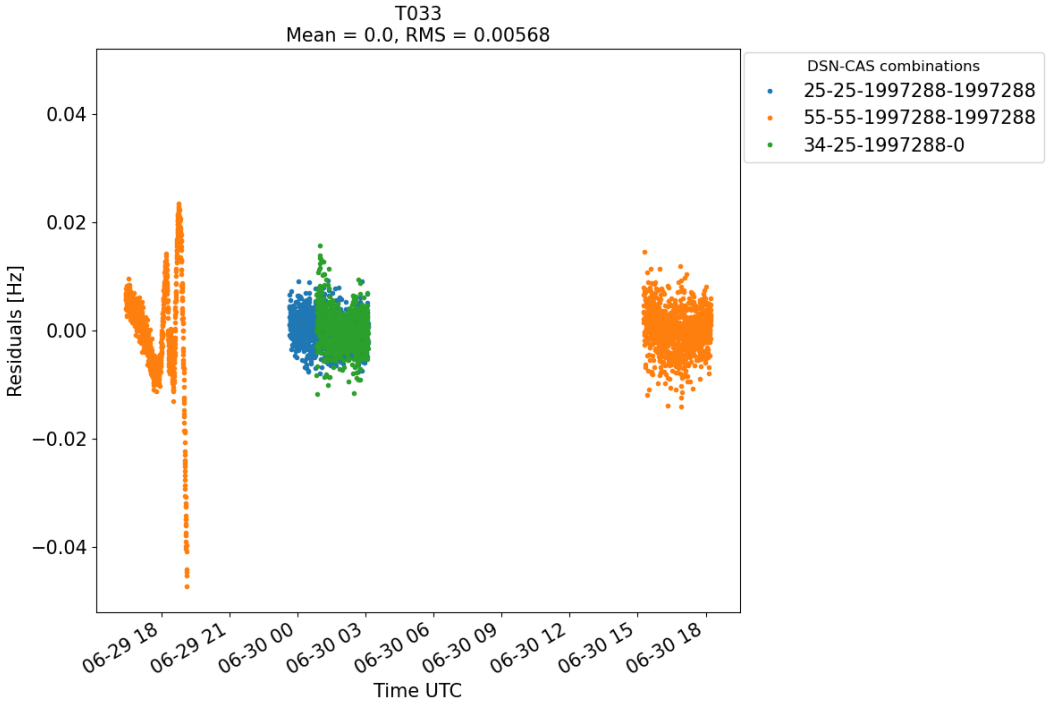

Figure 3.5: Residual plot of T033.

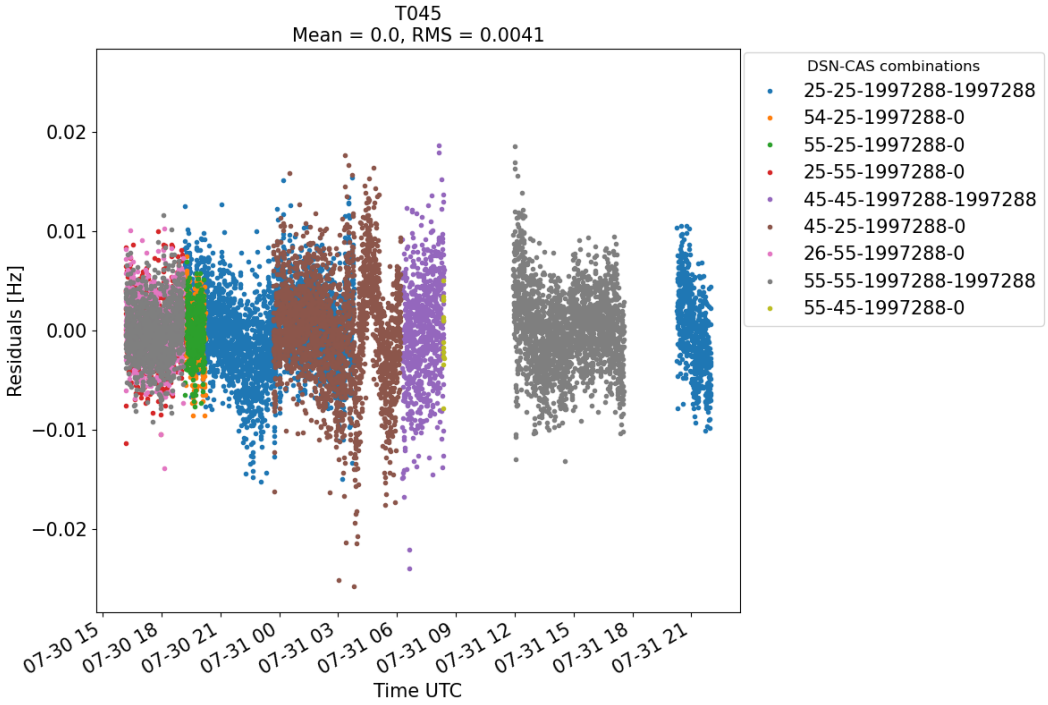

Figure 3.6: Residual plot of T045.

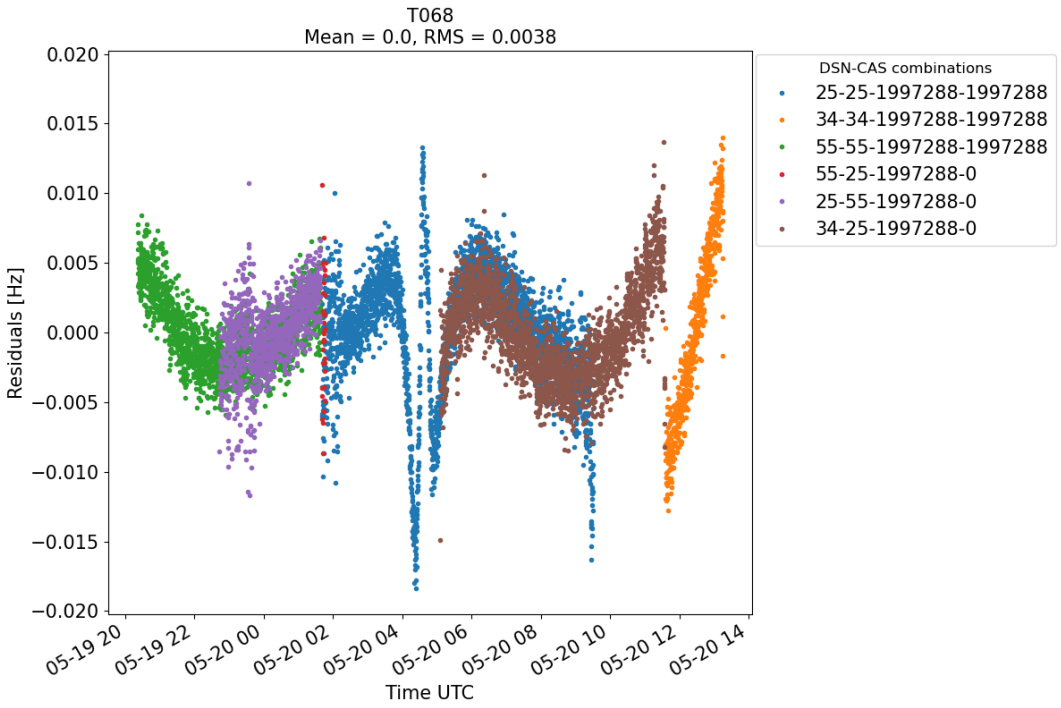

Figure 3.7: Residual plot of T068.

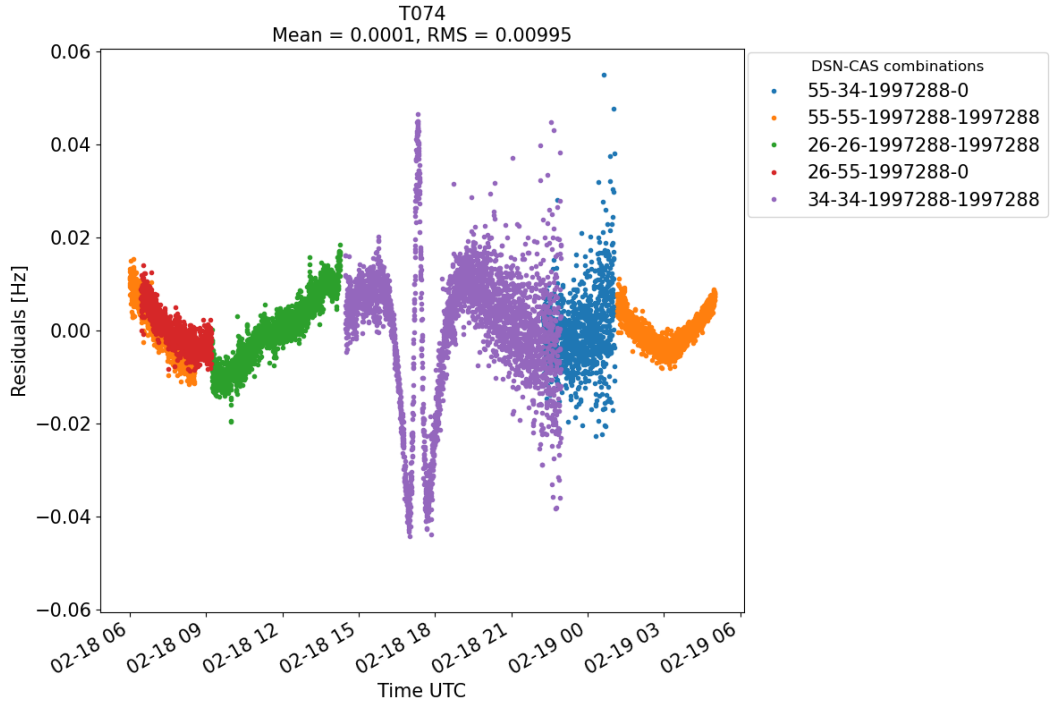

Figure 3.8: Residual plot of T074.

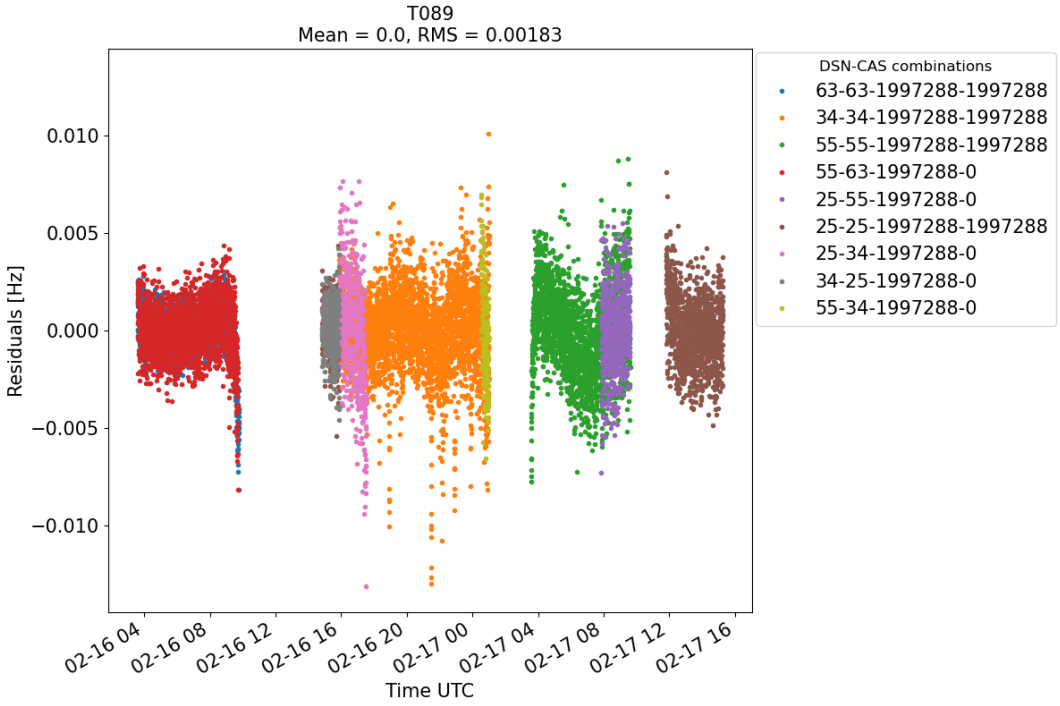

Figure 3.9: Residual plot of T089.

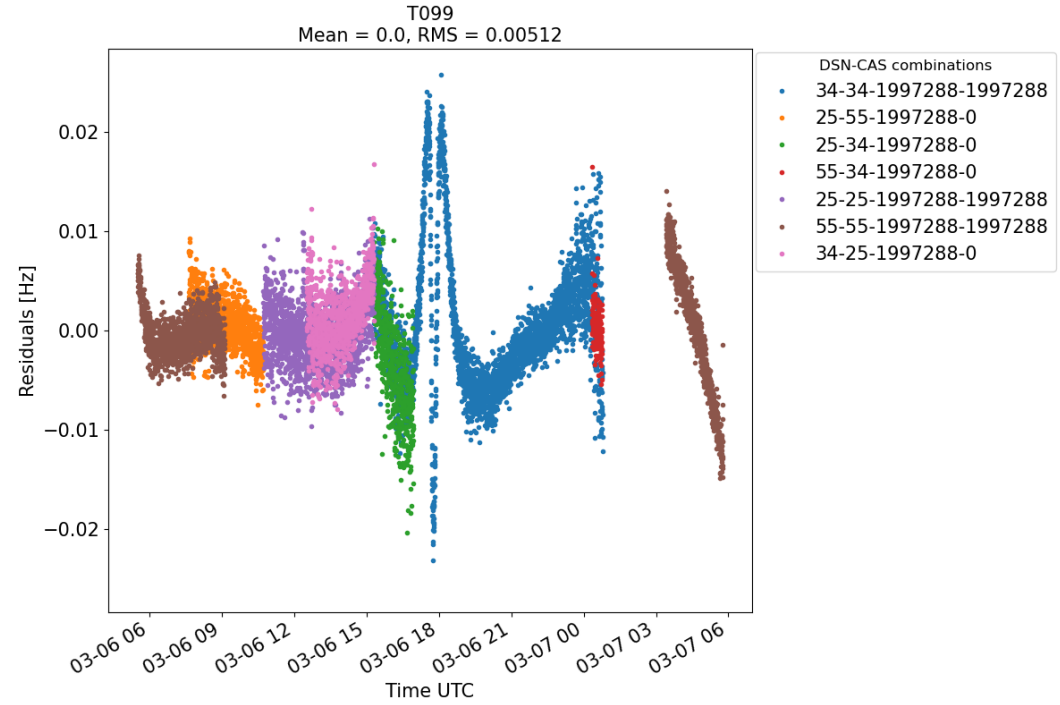

Figure 3.10: Residual plot of T099.

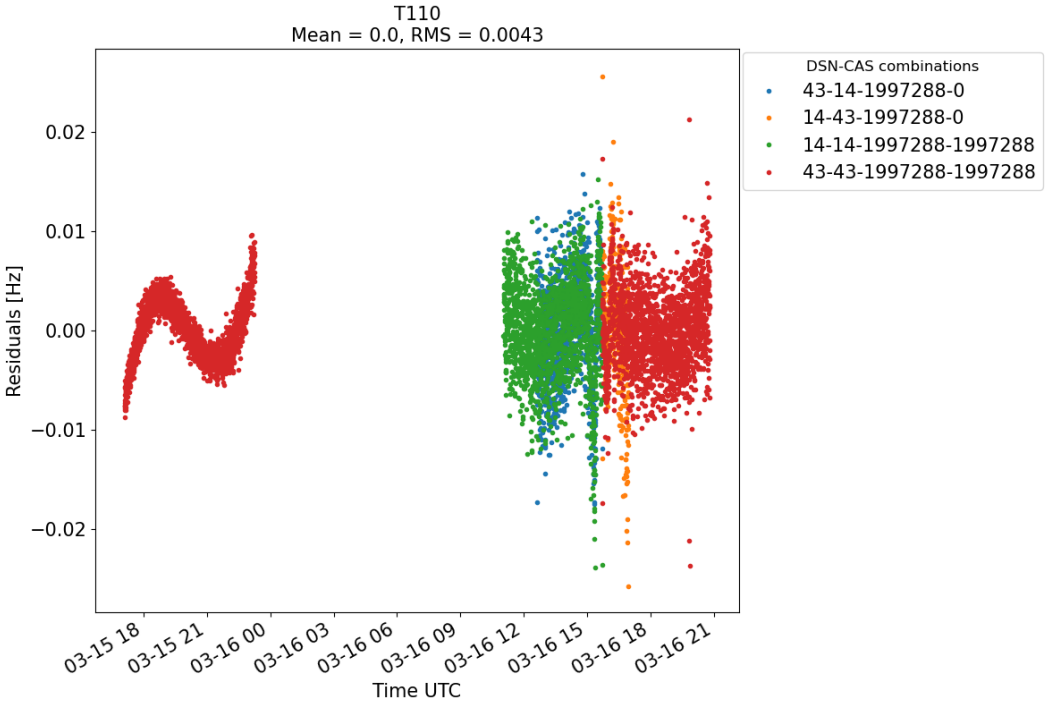

Figure 3.11: Residual plot of T110.

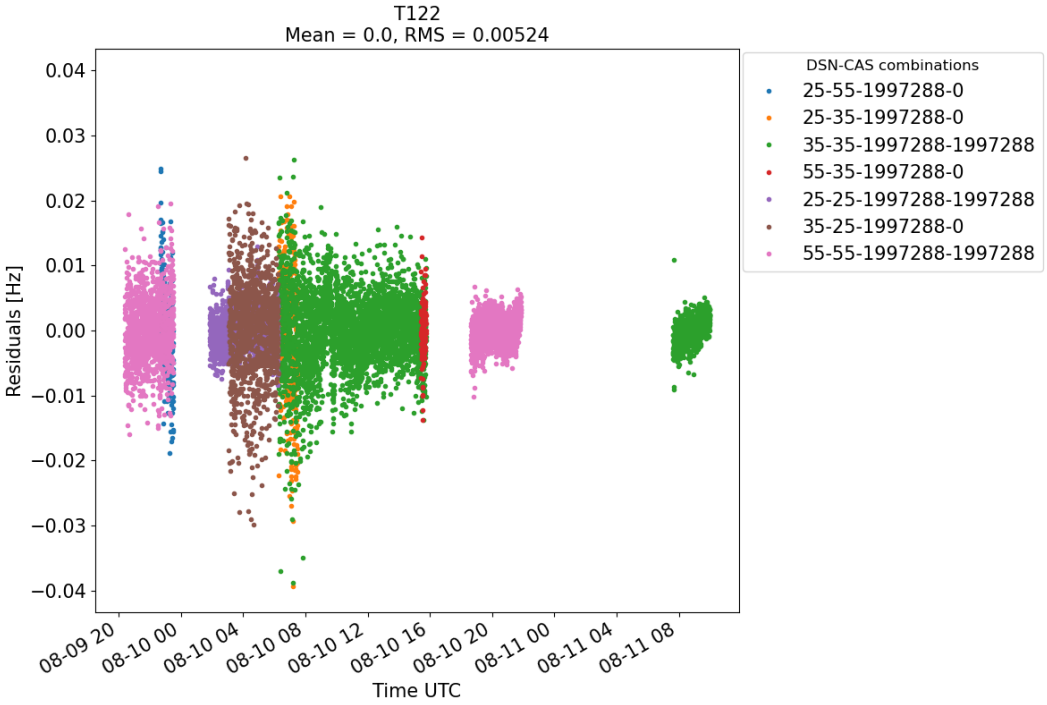

Figure 3.12: Residual plot of T122.

4

Sensitivity Analysis

The solution to the weighted least squares approximation (Equation 1.10) is sensitive to the parameters of the problem setup, such as the applied constraints ($\overline{W}_k$). The sensitivity is caused by the lack of data and severe under-sampling of the Eastern-Hemisphere leading to significant correlations between global parameters. In addition, many uncertainties in the accelerations acting on the satellite, as a result of inaccuracies in masses, mass distributions, positions and rotations of celestial bodies in the Saturnian planetary system, also contribute to this sensitivity. These two conditions can lead to several instabilities in the solution, where any change to the constraints of a certain parameter can impact the overall solution drastically. Given that these two conditions are applicable to the problem at hand, a sensitivity analysis gives insight into which parameters respond strongest to a change in applied constraints. This sheds light on potential instabilities in the orbit determination process. We first describe the applied methodology to determine these sensitive parameters. The results of the analysis will be discussed afterwards.

4.1. Methodology and approach

As noted from Chapter 1, the normal matrix of the system is composed of the design matrix and the observation weight matrix, $B^T W B$ (Equation 1.10). For a system consisting of only flybys, this matrix is very unstable, due to the earlier mentioned poor coverage leading to high correlations between parameters. Certain parameters are not sufficiently captured by the data to allow for a unique solution of these parameters, to which correlations and poor surface sampling (for global parameters) contribute. This will be highlighted in Section 4.2.4.

The multi-arc combined normal matrix has the property of being normal in the linear algebraic sense of the word, meaning that it commutes with its conjugate transpose [Lay, 2012]. From the combined normal matrix, the condition number can be calculated, which is the ratio of the highest and lowest eigenvalue of the matrix. The condition number is found to be about $2.93 \cdot 10^{52}$ - wherein a higher number corresponds to a less stable and ill-conditioned matrix. Note that this condition number applies to the unconstrained normal matrix $B^T W B$ and that it may vary, depending on which parameters are being estimated. It can hence be concluded that this unconstrained normal matrix is ill-conditioned, and constraints on the parameters definitely need to be applied.

Before the analysis, the constraint matrix will be computed, with constraints on arc specific parameters which are believed to be appropriate. Several of the constraints are taken from Durante et al. [2019] and others are rough estimations of what appropriate constraints should be. It is common to take *a priori* constraints on the parameters to be about 10% of its final adjusted value, which is the case for most of the parameters, except for the state parameters. The initial state parameters are usually known with an accuracy better than the allowed variance. Empirical accelerations are always constrained in gravity analysis and orbit determination processes. These parameters are not physically relatable to occurrences in the real word; they are merely added to account for mismodeling errors in the dynamical model [Yue and Yuan, 2015]. Most of them do not correlate significantly with many other parameters, meaning that if no constraints were applied to the empirical accelerations, they would absorb left-over signal more easily than other parameters. This could include the absorption of signal originating from estimated parameters as well, which of course needs to be avoided where possible. We also have to consider the fact that flybys are used: in essence, certain parameters are not well captured by the data, and estimation of these parameters will not always absorb the correct signal due to the poor coverage in some regions of Titan. This stresses the importance of finding a suitable constraint for the empirical accelerations. The applied constraints on

Table 4.1: Constraints used for all the estimated arc and global parameters in the sensitivity analysis. Note that the global parameters do not have an applied constraint, as this thesis estimates global parameters without these global constraints.

Parameter	**Constraint**	**Unit**	**Parameter**	**Constraint**	**Unit**
Position [1]	$2.0 \cdot 10^{3}$	m	Station bias	$1.0 \cdot 10^{-3}$	Hz
Velocity [1]	$2.0 \cdot 10^{-2}$	m/s	RTG scale (x, y) [2]	1.0	-
CD	$1.0 \cdot 10^{1}$	-	RTG scale (z) [2]	$5.0 \cdot 10^{-1}$	-
CR	1.0	-	Grav. coeff.	-	-
Emp. accelerations	$1.0 \cdot 10^{-7}$	m/s^2	k_2	-	-
CoM offset (T110)	$1.0 \cdot 10^{-1}$	m	μ	-	m^3/s^2

[1] From Durante et al. [2019]
[2] From Benedetto [2010-2011]

all parameters are shown in Table 4.1. Uncertainties on several parameters have been taken from previous papers. We stick to applying an allowed variance of 10% of its final value as a rule of thumb for the other parameters. Note that this logically does not apply for parameters which have an *a priori* value of zero. The approach is similar to the one adopted in Chapters 2 and 3, though we only adopt a COM estimation for flyby T110 during this analysis as this flyby uses the LGA instead of the HGA as noted earlier. The difference of this solution with the one where all flybys had estimates for the position of the CoM is statistically insignificant (see Chapter 2).

The constraint matrix corresponding to Table 4.1 ($\overline{W}_k$ in Equation 1.10) will be added to the unconstrained normal matrix. The unconstrained normal matrix is formed by combining all separate arc normal matrices with an applied weight (see Equation 1.11 and Table 3.3) With the now constrained normal matrix, the sensitivity analysis will be performed.

From the constrained normal matrix, we can find a solution by inverting the normal matrix and multiplying it by the right hand side (Equation 1.10):

$$\hat{\mathbf{x}}_k = \left(B^T W B + \overline{W}_k\right)^{-1} \left(B^T W \mathbf{y} + \overline{W}_k \bar{\mathbf{x}}_k\right) \tag{4.1}$$

This will be used as baseline solution throughout this chapter. Due to the instability of the matrix and the problem being poorly conditioned, however, the baseline solution may not be a real or feasible one. This solution will merely be used as reference to obtain and determine sensitivities of certain parameters, by applying different constraints. Depending on what arc specific parameters are being estimated, the normal matrix usually consists of about 350 parameters of which 34 are global parameters.

The sensitivity of the parameters is investigated in this chapter. The sensitivity is analyzed using two different methods. First, the parameters most sensitive to a change in the applied constraints (Table 4.1) are investigated. This will be performed by increasing and decreasing the constraint by a factor of ten per parameter equivalent to increasing or decreasing the parameter variance by a factor of ten, respectively. This will be achieved by looping over the parameters and adjusting the corresponding diagonal matrix element of the constraint matrix to a new value, while leaving the constraints on the other parameters unaltered Then, this constraint matrix with only one element altered compared to the baseline constraint matrix, will be added to the unconstrained normal matrix. A solution of the weighted least squares problem will be obtained in the same manner as before, after which it will be compared to the baseline solution. The difference with the baseline solution will be calculated as follows:

$$d\mathbf{x}_{sol} = \mathbf{x}_{baseline} - \mathbf{x}_{new} \tag{4.2}$$

where $d\mathbf{x}_{sol}$ is the difference between the baseline solution and the solution of the newly applied constraint $\mathbf{x}_{new}$. The aforementioned steps will be executed for every parameter in the normal matrix. The magnitudes of the difference with the baseline solution will be compared to determine which parameters are most influential to the inversion.

Secondly, a different useful method to determine the dominant parameters of a matrix uses Principal Component Analysis (PCA). PCA immediately finds the parameters in the system which cause most of the variance in the solution. A PCA will be performed on the constrained normal matrix. PCA finds new parameters (principal components), with lower principal components explaining most of the variance in the solution. The first principal component explains the most variance in the solution, then comes the second principal component, etcetera. These principal components are linear combinations of the estimated parameters. The principle components are in essence the eigenvectors of the unconstrained normal matrix. The eigenvector with the lowest eigenvalue is the

first principle component. Every principle component is hence a linear combination of the estimated parameters and only the top ten largest linear factors per principle component are considered, as will be explained in Section 4.2.4. Determining which parameters cause most of the variance from the unconstrained normal matrix gives us further knowledge on what the most dominant and sensitive parameters of the initial system are.

In summary, we analyse which parameters respond strongest to a change in the applied *a priori* variance. First, the *a priori* variance is increased by a factor of ten (Section 4.2.2). Based on Equation 4.2 the top 30 most sensitive parameters is determined. Second, the same analysis is performed by decreasing the *a priori* variance by a factor of ten (Section 4.2.3). Note that the *a priori* variance is inversely proportional to the constraint (See Equation 1.10 or Tapley et al. [2004]). Section 4.2.1 provides a description of how the outlined methodology from Section 4.1 is performed for Sections 4.2.2 and 4.2.3. Lastly, a PCA is performed where only the first ten principal components are analyzed, further explained in Section 4.2.4.

4.2. Results

Important to note is which parameters are estimated. First of all, the normal matrix is a combined matrix, where all normal matrices from every arc are combined into one (see Chapter 1). For every arc, a different Cassini state (position and velocity), a C_R and C_D coefficient, as well as RTG accelerometer scale factor, station/observation biases and empirical accelerations are estimated. The number of observation biases vary per arc, as this is related to the different Deep Space Network (DSN) ground stations - satellite observation configurations. Some arcs only have three different passes which each consist of one station-Cassini combination, whereas other flybys may have several passes with a total of ten different station-Cassini combinations. The same holds for the empirical accelerations; not all arcs are equally long, hence longer arcs will have more empirical accelerations. Flybys which are known to have attitude corrections in the signal (such as T022, T045, T074 and T122) have shorter arcs and hence also fewer empirical accelerations, which are estimated over periods of eight hours.

The position of Titan is not accurately known in general. A lot of uncertainties in the Saturnian system remain, in terms of forces acting on satellites due to gravitational attraction of several other bodies in the Saturnian system. Several of these uncertainties could be Saturns entire ring mass, masses of other Saturnian moons, the accurate mass distribution and rotation of Saturn (e.g. Durante et al. [2019]). This leads to an inaccurate position of Titan (discussed also in Chapters 2 and 3). In this analysis, similar to Chapter 2, we estimate station/observation biases which could mitigate the effect of an inaccurate Titan position. Titan's inaccurate position leads to an inaccurately calculated gravity force, which causes a more or less constant bias in the observations. Observation biases could thus mitigate the effect of an inaccurate position of Titan. This is not the main reason to estimate observation biases however: certain noise, such as errors in modeling the Earth's tropospheric effect on the observations, is introduced with the use of different station-satellite combinations, hence the need for estimation of biases is still there.

4.2.1. Computational stability of the solution

The computations from Sections 4.2.2 and 4.2.3 are performed in Python using the Numpy and Scipy libraries. Variables are saved as 64-bit floating point numbers. With the initial constraints and constraint matrix (see Table 4.1), it should be mentioned that the constrained normal matrix is stable and allows for an inversion without warnings. Hence, the baseline solution of the sensitivity analysis can be said to be computationally stable.

If certain constraints are applied, however, it is possible that the normal matrix becomes computationally unstable, due to the matrix becoming ill-conditioned. As a result, the obtained solutions with differently applied constraints could contain inaccuracies introduced due to the inability of the 64-bit floating point number to contain a certain value. Testing for this illustrates that approximately half of the matrices are ill-conditioned, after applying a tighter or looser constraint for a certain variable. A warning is given by the linear algebra library in Python if a matrix is ill-conditioned, which could lead to inaccurate inverses of the matrix or solutions to the problem. This happens for all types of parameters, and not just one type. This stresses again the ill-posedness of this orbit and gravity determination problem.

4.2.2. Increase variance by a factor ten

Below, the results of the analysis are set out, obtained by comparing high variance cases to the baseline solution. The 30 parameters (out of 351) with largest deviations to the baseline solution are 18 empirical accelerations (not from just one arc), 5 state velocities and 2 positions (most velocities are more dominant than the positions, some are from the same arc), 3 RTG accelerometer scale factors and 2 observation biases. In total, approximately 120

empirical accelerations are estimated, which means that the majority of the estimated parameters are empirical accelerations as well.

Generally speaking, the empirical accelerations are by far the most sensitive parameters: decreasing the variance by a factor ten leads to four empirical accelerations having the largest change for all estimated parameters. Additionally, the number of empirical accelerations is over-represented in the top 30 of considered dominant parameters. This is unsurprising; empirical accelerations correlate less with other parameters, hence allowing them to change more easily will most likely result in a solution which differs quite a lot compared to the otherwise obtained solution.

With regards to the Cassini state parameters, three state parameters from flyby T110 occur amongst the 30 most dominant parameters. The dominance of this parameter could be caused by other uncertainties in this flyby, as almost all empirical accelerations in this flyby are also in the top 30 of most dominant parameters, together with one RTG accelerometer scale factor and observation bias. In other words, this indicates that the dynamic model does not fit very well for this flyby. Given the significant addition to the sampling of Titans surface (Figure 1 in Chapter 2), the flyby is considered in the analysis of the overall gravity field in the scientific article. The arc has been adjusted accordingly: the constraint on the center of mass estimation is increased (Table 3.2) and the arc period is shortened. These changes have introduced outliers which are removed if the observations residuals are not consistent with the other observation residuals surrounding that observation. Note that the change in arc setup for T110 is a result of the sensitivity analysis and the modified arc setup is only used for the article.

Interestingly, the three highest ranked empirical accelerations are those from flyby T033. Other parameters from T033 appearing in the dominant parameter list are an RTG bias, and several observation biases. Hence, it appears that T033 also still contains un-modeled or incorrectly modeled forces, where empirical accelerations absorb significant signal if they are not constrained properly.

It is worth finding out how sensitive the different global parameters are, as these are the parameters that we are after. Yet, the aforementioned method does not highlight this very well. In this approach, namely, the influence of a variance of a factor ten times larger is investigated, and compared to the aforementioned baseline solution with the corresponding applied constraints (Table 4.1). For a gravity estimation, the most important parameters, in this work mainly the spherical harmonic expansion coefficients of the gravity field and k_2, are given an infinite variance. In other words, they can become any value that the observation residuals would allow. In this case, increasing or decreasing variance tenfold would not matter as their values would still be allowed to be infinite. For this reason, all the global parameters are found to be least dominant using this method, which in this case is merely due to them not having constraints in the gravity analysis.

4.2.3. Decrease variance by a factor ten

Next, we apply the same procedure with one tenth of the variance. Afterwards, we compare the results of this procedure with results of the previous section.

Something remarkable happens when decreasing the variance; there are no more RTG accelerometer scale factors among the 30 most dominant parameters. Additionally, this top 30 is no longer over-represented by empirical accelerations. The list consists of 8 empirical accelerations, one observation bias, 11 position and 10 velocity parameters. Decreasing the variance results in a list consisting of mainly state parameters. Constraining the state parameters even further thus results in significant changes to the solution, meaning they contribute, to a large extent to the initial baseline solution. It is unsurprising that such a strong dependence on the state parameters is visible: the initial state of the spacecraft determines to a large extent what the trajectory of the spacecraft looks like. Therefore, constraining these parameters tightly results in other parameters having to be disproportionally adjusted accordingly.

The results should be interpreted with caution; it is not always straightforward to compare different types of parameters and their sensitivity to constraints. Even for the tighter constraints, four out of the five most dominant parameters remain empirical accelerations - albeit different ones from before. Empirical accelerations are still the most dominant relative to other types of parameters. An empirical acceleration can have a much larger influence if that empirical acceleration is estimated during a time at which the dynamical model of the spacecraft is poorer. Hence, restricting this empirical acceleration to grow or decrease results in other parameters having to compensate for this poor dynamic model, resulting in substantially different solutions.

The difference between the two sensitivity analyses with less and more variance, sheds light on the importance of the applied constraints. First of all, by decreasing the allowed variance, state parameters become more dominant. Evidently, the variance of the state parameters should not be decreased further than the baseline variance: this parameter does not correlate with other parameters very much and should therefore not be as sensitive

to a change in constraint. Hence, the constraints of the baseline solution for the state parameters are better, than those from the less variance solution. Additionally, with the less variance sensitivity analysis, the empirical accelerations become relatively less dominant compared to the more variance solution. It is good to observe that the empirical accelerations become less dominant with tighter constraints and significantly more dominant with looser constraints. This means that the constraints for the applied baseline solution are a trade-off between dominant and weak constraints. We do not want to constrain the empirical accelerations too tightly, as the dynamic force model will be highly inaccurate. Constraining the empirical accelerations too loosely will result in them absorbing signal in the observation residuals caused by other parameters as the empirical accelerations do not correlate with other parameters substantially. The baseline constraints suffice these criteria. The same reasoning holds for the constraints on state parameters. Similarly to Section 4.2.2, the dominance of the global parameters cannot be determined in this fashion. The initially applied variance is infinite, and would remain infinite after dividing the variance by a factor ten.

In conclusion, comparing the less and more variance solution, results in either a more dominant behaviour of the state parameters or the empirical accelerations. It is expected that empirical accelerations are more dominant and influence the solution significantly in numerous ways. They correlate less with other parameters making them well-defined and easier to estimate uniquely. As a result, they absorb the observation signal very well. For this reason, the constraints should be applied such that the empirical accelerations do not grow too large, which is found to be the case for the baseline solution. Similarly, for the other parameters, the baseline constraints suffice. Other parameters barely appear in the list of 30 most dominant parameters, which means that no real sensitivity to the applied baseline constraints remains, which is in fact the preferred outcome, as ideally we want to apply constraints which influence the solution barely. With this methodology, constraining this parameter more or less does not significantly influence the solution. In practice, also parameters not appearing in the list of 30 most dominant parameters can substantially influence the solution, merely due to the lack of data causing significant correlation between parameters. Uncertainties in the adopted dynamic model also contribute to dominance of certain arc-specific parameters, where tightening/loosening constraints results in over-compensation of other arc parameters.

4.2.4. PCA

Because of instabilities with matrix inversion of previous approaches, and not being able to determine the sensitivity of global parameters, it is interesting to use a different sensitivity estimation method: the principal component analysis (PCA). In this section a PCA is applied to the constrained normal matrix, to find out which linear combination of parameters explains most of the variance in the solution. That is, varying these parameters (i.e. constraining them tighter) results in a larger difference with the initial solution. The difference with the other two approaches in Sections 4.2.2 and 4.2.3 is that the constrained normal matrix remains unaltered in this analysis.

PCA is used in several fields to determine the influence of parameters in the dataset or problem setup. The mathematical definition of PCA is to find a change in variables from $\mathbf{X} = P\mathbf{Y}$ such that the variables $y_1, \ldots, y_p$ are uncorrelated and arranged in order of decreasing variance [Lay, 2012]. In the field of machine learning, for example, one can apply this technique to find different features from the dataset which explain most of the variance, i.e. the most important features (see for example Shalev-Shwartz and Ben-David [2014]). With this method it is possible to reduce dimensionality of the problem, thereby reducing the computational effort necessary to obtain an accurate prediction model.

In the field of orbit determination, PCA can be used to determine important, dominant parameters in the same fashion. Instead of a big dataset, we have a (constrained) normal matrix with each column in this matrix being related to one specific estimated parameter.

For the principal component analysis, the Sklearn toolkit for Python is used [Pedregosa et al., 2011]. This is initially a Machine Learning toolkit, though since this is simply a mathematical approach for a given dataset, the principal component analysis will be identical.

Applying the PCA results in 351 linearly independent combinations of the initial parameters. Higher principal components explain a lower variance in the solution: $\sigma^2(y_p) > \sigma^2(y_q)$ with $q > p$. For this problem, the first principal component explains 43.4% of the total variance, component two 20.2% and component three 16.9%. The tenth principal component only explains 0.0013% of the variance, which is already incredibly small compared to the first three principal components. To put the other principal components in perspective, the last principal component (the 351st) explains a negligible $1.0 \cdot 10^{-36}$% of the variance. As variance drops rapidly with the number of principal components and given the fact that the tenth principal component only contributes to the total variance of the solution by 0.0013%, only the first ten dominant principal components are analyzed.

A principal component consists of a linear combination of the parameter set. For example, the first principal component y_1 is given as $y_1 = w_1x_1 + w_2x_2 + \cdots + w_nx_n$, where x_i for $i = 1, \ldots, n$ are all the n estimated parameters with their corresponding linear contribution w_i. Every parameter x_i is ranked from high to low weight such that $w_i > w_{i+1}\ \forall\ i$. The weights w_i are found from the PCA directly, as the principal components are in essence the eigenvectors of constrained normal matrix. Hence, w_i are the components of the eigenvector corresponding to parameter x_i. Since the parameters x_i are ranked in the principal component by their corresponding contribution w_i, the first parameter x_1 has a large linear contribution w_1. As noted, the first ten principal components explain most variance in the solution (>99.99%). Hence, only the first ten principal components are considered in the PCA for this thesis. For all these principal components, the first ten parameters x_i for $i = 1, \ldots, 10$ contribute substantially to that particular principal component ($w_1 \gg w_{11}$). Therefore, compared to the first ten parameters x_i, the contributions of the other parameters to the principal components can be neglected.

Consequently, it is possible to determine the most dominant parameters for every principal component, and hence for the given orbit determination problem at hand as well. Executing the principal component analysis as described, results in a top ten of principal components, summarized in Table 4.2. The first five principal components only consist of a linear combination of empirical accelerations. In the sixth till the ninth component, a linear combination of empirical accelerations together with several (or one) global parameters combine a principal component and the tenth component is again a component with the ten dominant parameters being empirical accelerations. Hence, the PCA finds that the only dominant arc parameters are the empirical accelerations.

The PCA better predicts the influence of global parameters. Empirical accelerations and certain global parameters can be considered as the dominant parameters explaining most variance in the solution of the estimated parameters. The global parameters which explain considerable amounts of the total variance of the principal components are C_{20}, C_{22}, C_{31}, S_{21}, S_{22}, S_{31}, S_{42}, and S_{52} (see Table 4.2). Of course, it is expected that spherical harmonic gravity coefficients of lower degrees (2-3) have a considerable effect on the overall gravity solution, and this principal component analysis confirms that. Some higher order tesseral coefficients also explain much of the variance in the solution. An explanation for this might be that these specific higher order coefficients are well captured by the data due to the reasonable coverage of the flybys in regions of Titan's surface described by these coefficients. In general, the total surface coverage is poor and unevenly distributed however (Figure 1 in Chapter 2), which is why not all higher order coefficients are found to be dominant parameters (Table 4.2). Hence, it could be argued whether the data contain sufficient information on the degree four and five spherical harmonics of the gravity field, given the absence of most of these gravity coefficients in Table 4.2 and generally poor sampling of Titan's surface.

Analyzing different principal components has given us insight in which flybys may have an important effect. Some principal components only contain[1] empirical accelerations from one certain flyby. From this analysis it can be concluded that giving a lower (or higher) weight to that particular flyby will result in a significantly different solution. Furthermore, one can take different actions to make the flyby as influential as other flybys by putting a tighter constraint on empirical accelerations from the dominant flyby. This information is valuable; it gives an indication of influences of flybys to determine appropriate arc weights. In addition, dominant empirical accelerations from these arcs can be constrained tighter to limit their influence on the overall solution.

The sensitivity analysis has given us insight into sensitive parameters which respond to changes in the applied constraints (Sections 4.2.2 and 4.2.3), as well as parameters explaining most variance in the solution (Section 4.2.4). The arc of flyby T110 has been shortened before use in Chapter 2 as a result of this analysis. Features of satellite rotation were still visible in the residuals of T110, which indicates that GEODYN II uses a wrong CoM position for the spacecraft during T110. Note that also a different antenna was used for radio tracking during this flyby. Hence, the constraint for the CoM offset was made less tight (see Chapter 3).

Some constraints of the baseline solution (Table 4.1) have been modified for the analysis in Chapter 2. The constraint on C_D has been modified to 1.0 instead of 10.0, which resulted in a statistically insignificant difference in the estimated parameter set ($\hat{\mathbf{x}}_k$ in Equation 1.10). The constraint on C_R is altered to 0.1 instead of 1.0 to conform with the constraint being 10% of the *a priori* value; a criteria outlined in Chapter 3. Most importantly, the constraint on C_R was modified as otherwise solutions of C_R were found to be negative. This implies an SRP force in the direction of the Sun: something we know cannot be true. All other applied constraints to the parameters are left unchanged with respect to the baseline constraints in Table 4.1 (see also Table 3.2).

Table 4.2 contains only low degree spherical harmonic coefficients of the gravity field apart from S_{42} and S_{52}. The tidal Love number k_2 is also absent in this table, implying that this Love number does not explain most

[1] in general of course not true, as principal components are linear combination of all the initial parameters. Though in this work, only the first ten parameters are considered per principal component

Table 4.2: Summary of the first ten principal components (PC) from the PCA. Each principal component consists of 10 parameters: global parameters or arc-specific empirical accelerations. The Flybys column indicates which flyby these empirical accelerations belong to, and the number in brackets indicates the number of empirical accelerations belonging to that flyby. Note that ten parameter contributions per principal component are considered and y_2 therefore has eight empirical accelerations belonging to T022.

PC	Flybys	Global Parameters	PC	Flybys	Global Parameters
y_1	T089	-	y_6	T045, T122(1), T068(1), T022(1)	C_{30}, S_{22}, C_{22}
y_2	T022, T099(1), T089(1)	-	y_7	T110, T074(2), T033(1), T068(1), T045(1)	S_{52}, S_{42}
y_3	T099, T022(3)	-	y_8	T033	C_{21}
y_4	T068, T022(1), T089(1), T122(1)	-	y_9	T074, T033(1), T099(1), T045(1), T110(1)	C_{20}, S_{31}, S_{22}
y_5	T122, T068(4)	-	y_{10}	T068, T099(1), T074(1)	-

variance in the solution of the estimated parameter set ($\hat{\mathbf{x}}_k$ in Equation 1.10). k_2 correlates well with several parameters. The same is true for other higher order spherical harmonic gravity coefficients. This can make it difficult to estimate these parameters separately, supported by the discussions in Chapter 2 and 3. The absence of higher order parameters in Table 4.2 strongly supports the hypothesis that the data do not capture higher order spherical harmonic degrees (> 3) sufficiently, as claimed in Chapter 2. This is also one of the reasons why we do not estimate Titan's gravity field with a spherical harmonic expansion beyond degree three.

5

Solar Radiation Pressure Model

In recent analyses of the gravity field and tides of Titan, a simplistic spacecraft model is adopted in the orbit determination process. Such a model is necessary to, amongst others, calculate the solar radiation pressure (SRP) and drag on the spacecraft. Simply put, this simplistic model is a rectangular box with a slender rod representing the large boom on the spacecraft with the magnetometer at the tip. Implementing such a simple model is a first order approximation of the SRP and drag. This simple model is only accurate to first order: it can be further improved by implementing a more accurate spacecraft model, leading to an improved dynamic force model of the spacecraft in the orbit determination process. In this chapter, the design of a more sophisticated SRP model is outlined, using a more detailed spacecraft model. An extensive description of the program code behind the SRP calculation model can be found at the end of this chapter.

Due to differences in the dynamic force model of this thesis and the dynamic model from previous research [Durante et al., 2019], this SRP model is not yet implemented in the orbit and gravity determination analysis in Chapters 2 and 3. The dynamic force models from Chapter 2 and Durante et al. [2019] differ significantly, where our force model emphasizes the need for empirical accelerations whilst Durante et al. [2019] does not mention these accelerations. These discrepancies in dynamic force models do not allow a proper application of this SRP model, as it is highly unlikely that its effect will be visible in the results at all; the SRP force is orders of magnitudes smaller than the empirical accelerations in Chapter 2 for example. Before applying the SRP model, these discrepancies in the dynamic force model need to be decreased further. Nevertheless, this accurate SRP model contributes to the literature as it calculates the SRP on the Cassini spacecraft at different times during the mission.

5.1. Detailed spacecraft model

The implemented simple spacecraft panel model from previous research is shown in Figure 5.1 [Durante et al., 2019, Iess et al., 2010, 2012]. This simplified model is a box-wing model which roughly approximates the contour of the spacecraft by one box with one wing (the magnetometer boom). The details of the surface contour are missing, as is usually the case with a box-wing model, which leads to an inaccurate estimation of the SRP. Starting from the sophisticated 3D spacecraft model on the right in Figure 5.1, an SRP tool is developed, explained and verified in this chapter.

A discretized 3D version of the spacecraft model is available from the NASA website as an .obj file [NASA, 2019]. The original 3D model consists of 25736 triangular surfaces. This model has to be down-sampled, such that it consists of less surfaces; the designed SRP calculation program takes too long to obtain an estimation of the SRP force otherwise, explained in detail in Section 5.3. Obtaining the vertices corresponding to every surface is straightforward, using the Python module Open3d [Zhou et al., 2018]. This module has a lot of features including creating and down-sampling certain meshes, which are discretized surfaces of 3D objects as shown in Figure 5.1 for example. To obtain a mesh consisting of less triangles/surfaces, the technique called simplify quadric decimation is used [Garland and Heckbert, 1997]. This technique modifies the original mesh to a mesh containing X surfaces. In Figure 5.2, the differences between the more accurate model (a) and the model consisting of 1500 surfaces (b) are quite clearly visible; some very detailed features are absent in the simplified model such as the long radio and plasma wave science instruments. The 1500 surfaces model is shown to be a suitable replacement for the most accurate model, as the contour and most details of the spacecraft are still intact, as explained in Section

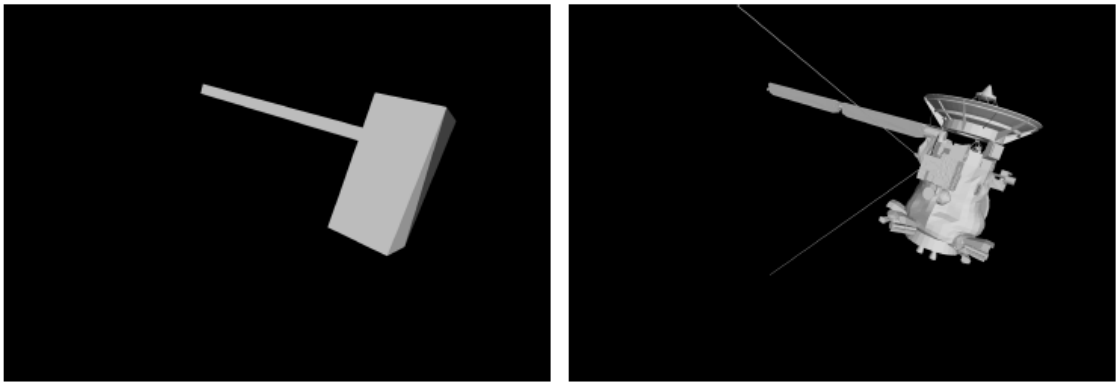

(a) Simple box-wing model for Cassini (b) Detailed model for Cassini

Figure 5.1: Different models for Cassini used in previous (a) and future (b) analysis of Cassini tracking data. [Credit: E. Mazarico/NASA GSFC]

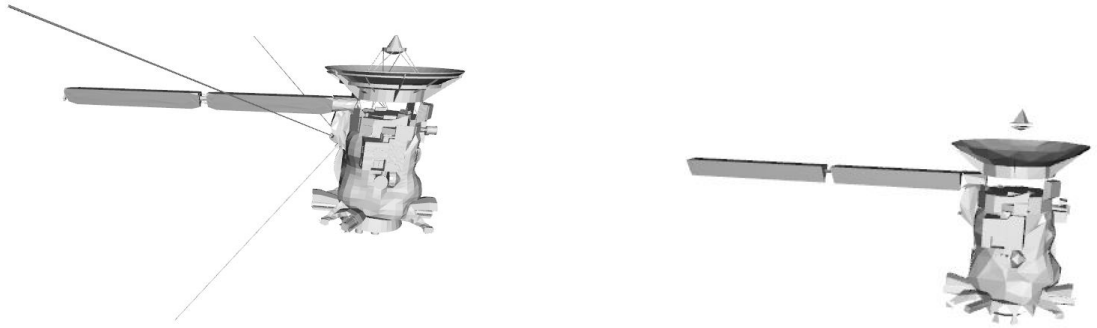

(a) Cassini model consisting of 25376 surfaces (b) Cassini model consisting of 1500 surfaces

Figure 5.2: Detailed Cassini spacecraft model with 25736 triangles (a) and less detailed Cassini spacecraft model with ∼1500 triangles (b).

5.3. In addition, this model is already a visible improvement compared to the old box-wing model (Figure 5.1, see also Section 5.3).

5.2. Methodology of SRP model

From the 3D Cassini model, which consists of triangular surfaces expressed in vertex coordinates and face-combinations, the entire SRP acceleration on the spacecraft can be calculated. The main task will be to find out which of these surfaces are in direct sunlight, given the positions of these triangle vertices and the Sun. If a surface is classified as being in direct sunlight, the SRP acceleration is calculated on that surface. The SRP can be calculated using the following equation [Tapley et al., 2004]:

$$\mathbf{a_R} = -\nu C_R \frac{A_S}{m_s} P_s \mathbf{r}_s \tag{5.1}$$

where ν is the eclipse factor (1 when in direct sunlight, 0 otherwise), C_R is the reflectivity coefficient of the satellite, A_s is the cross sectional area of the surface (perpendicular to the vector pointing to the Sun), m_s is the mass of the satellite, P_s is the momentum flux at the position of the satellite, and $\mathbf{r_s}$ is the unit vector from the satellite to the Sun. In the program, ν will be calculated given the time at which the SRP is to be obtained. In addition, the mass of the satellite and the area of the surface are known quantities[1]. $P_s = 4.56 \cdot 10^{-6}$ N/m^2 at the Earth and scales as $1/d^2$ where d is the distance to the Sun in AU, $d = 9.5$ AU for Saturn [Tapley et al., 2004]. An appropriate value of the solar radiation coefficient is determined by approximating the reflectivity parameters of the spacecraft. The solar radiation coefficient relates to the reflectivity and absorption coefficient as follows:

[1] see e.g. `https://pds-atmospheres.nmsu.edu/data_and_services/atmospheres_data/Cassini/eng-overview.html` for mass history of the Cassini spacecraft

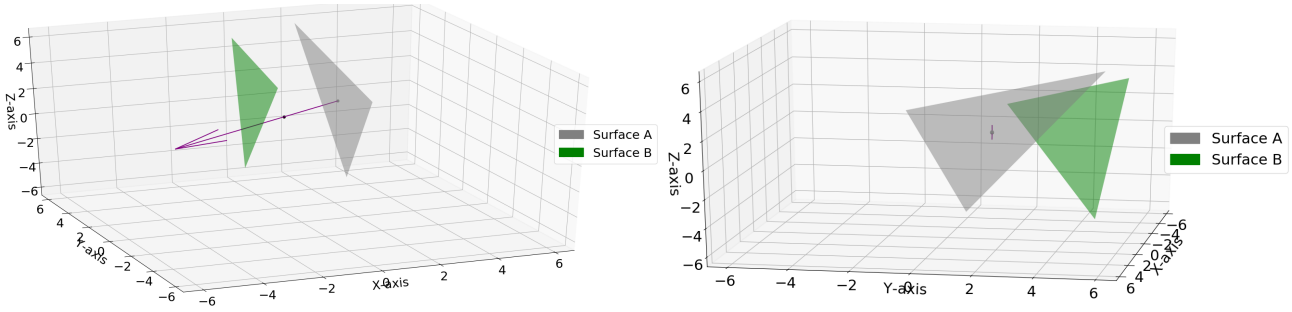

Figure 5.3: Illustration of surface A not covering surface B. The purple arrow is a vector from the centroid of surface A pointing away from the Sun. The projection of the centroid of surface A (indicated by a purple point) lies outside the perimeter of surface B. The two sub-figures are the same plot, shown from different angles. The right plot illustrates the orientation of the surfaces from the Sun's perspective (surface A is closer to the Sun). We conclude that surface B is not covered for the most part, hence it will be classified as being exposed.

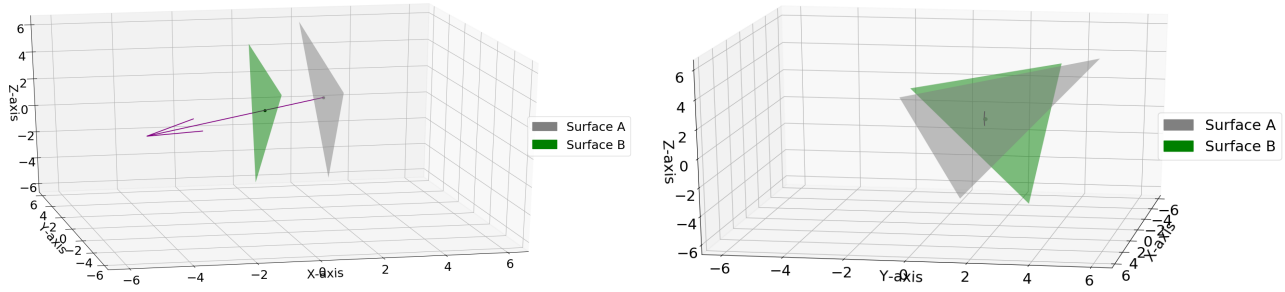

Figure 5.4: Illustration of surface A shading surface B. The purple arrow is a vector from the centroid of surface A pointing away from the Sun. The two sub-figures show the same plot from different angles. The right plot illustrates the orientation of the surfaces from the Sun's perspective (surface A is closer to the Sun). The projection of the centroid of surface A (indicated by a purple point) lies inside of surface B. Hence, surface B is not exposed.

$$C_R = 1 + \rho \tag{5.2}$$

$$\rho = 1 - \alpha \tag{5.3}$$

where ρ is the reflectivity of the surface area, and α is the absorption coefficient. It makes sense that the absorption coefficient and reflectivity add up to 1; all incoming radiation not absorbed has to be reflected. The surface area of the spacecraft consists of different materials. Surfaces of the model that belong to the HGA are given the absorption coefficient of the HGA and faces belonging to the rest of the spacecraft are given the absorption coefficient of the multi-layer insulation (MLI) blankets. The HGA of Cassini is coated with PCBZ paint, having an absorption coefficient of 0.2 (BOL) and 0.4 (EOL) [Fabiani and Costabile, 1997]. It is assumed that the rest of the model is covered in MLI, as the spacecraft is covered with this material for the most part. Most of the MLI on the Cassini spacecraft has aluminized Indian Tin Oxide (ITO) Kapton-Nomex Scrim on the space side [Lin et al., 1995], which has an absorption coefficient of about 0.10 BOL [Sheldahl: A Multek Brand]. An EOL value of 0.20 is assumed for this MLI blanket, as the EOL value for the PCBZ paint is also twice as large. It is assumed these material properties degrade linearly in time, starting at launch in October 1997 and ending in September 2017.

Using Figure 5.3 and 5.4, the method of determining which surfaces are in direct sunlight (surface exposure classification) will be illustrated and explained. A surface (A) has to be in front of another surface (B) from the point of view of the Sun to generate a shadow. Several strategies can be applied to determine whether a surface from the 3D model is in direct sunlight, which generally includes a trade-off between accuracy and required computing power.

The applied methodology on surface exposure classification relies on centroids of surfaces. Consider, for example, only two surfaces of which a shade classification has to be performed (see Figure 5.4 for clarification). Determining whether a surface lies behind another surface seen from the point of view of the Sun, is performed by projecting the centroid of a surface onto the plane wherein the other surface lies. Surface A is considered in front of surface B (and thus unexposed) if the projection of A's centroid onto the plane of surface B is away from the Sun, and this projection lies within (or close to) the perimeter of surface B. The projection of the centroid

of surface A is obtained by extending the vector from the Sun to centroid A, such that it intersects the plane in which surface B lies. Figure 5.3 and 5.4 illustrate this methodology using figures of two surfaces A and B. This methodology hence classifies a surface B as not being exposed to the Sun, if the centroid of surface A is in front of surface B from the Sun's perspective (Figure 5.4). Surface A covers surface B for the largest part with this method, as the surfaces are all approximately the same size. Inspecting Figure 5.3, it is clear that surface A only causes a small shadow onto surface B, which partly covers surface B. Surface B is still exposed to the Sun for the largest part. Hence, it is better to classify surface B as exposed to the Sun, rather than unexposed, as a much larger error will be introduced otherwise. Furthermore, this is a direct consequence of having to discretize the contour and surface area of the spacecraft and this applied methodology. The error can be minimized by selecting a model with sufficiently small surfaces with equal sizes and shapes, such that the error of misclassification is negligibly small. In Section 5.3, it is shown that the selected model meets these requirements.

It is possible to determine how much of a surface is in the shadow and how much is in direct sunlight. For that, the shade of a surface (surface A) should be projected onto the other surface (surface B). If the projection partly overlaps with surface B, the percentage of exposed area can be calculated. Calculating this percentage of area visible from the point of view of the Sun is very complex and hence requires considerable computation power. Not only do we need to calculate whether a surface is in front of another surface; the percentage of shaded surface (surface B in the example above) also has to be calculated.

However, it is not necessary to determine which surfaces are in direct sunlight this accurately, as the number of surfaces of the model has a significant impact on this. With a more accurate spacecraft model (i.e. more surfaces), incorrectly classifying a surface as shaded does not have a large impact on the final result of the calculated SRP, as the SRP on one surface contributes less to the total SRP compared to a model with less surfaces. To maximize performance though, the number of incorrect classifications has to be minimized. Certain approximations and simplifications are made to be able to tell whether a surface is unexposed or in direct sunlight. This methodology introduces small, justified inaccuracies given their small impact on the calculated SRP force. Observing Figure 5.3, a small error is made by classifying it entirely as exposed. As noted however, the error would be larger if this area would be classified otherwise. In addition, this 'misclassification' only happens at boundaries of the spacecraft and self-shadowing due to e.g. the magnetometer boom. In Section 5.3, it is elaborately shown that the introduced error as a result of these assumptions is negligible. Hence, it is indeed better to apply the surface exposure classification methodology based on the projection of centroids, rather than determining which fraction of all surfaces are in direct sunlight.

For this method, it is necessary to consider more or less every possible combination of surfaces. In other words, it should be checked whether surface A lies in front of any of the other surfaces. This depends on the positions of surface A, the other surfaces, and the Sun. Surface A will be considered first, and for the remainder of the surfaces (B) it will be determined which lie behind surface A (see Section 5.4 for more details). Given the three vertices of a surface B and the projection of the centroid of surface A, the area of the three triangles connecting the vertices of B with the projection of the centroid of A are calculated, as illustrated in Figure 5.5: the sum of the colored smaller triangles sums up to the total area of surface B, only if the projection of A's centroid lies within the perimeter of surface B. If the projection of the centroid of A is within the perimeter of surface B, surface B is unexposed to the Sun. Of course, if surface B is found to be behind some surface A, then the program does not check whether it is behind some other surface as that is not relevant.

This methodology carries a small weakness: there are certain scenarios where the projection of surface A lies within surface B, but that does not necessarily mean that surface B would be in the shadow for a large part. One example to visualize this is by considering a small surface A in front of and close to a big surface B, where the centroid of A would be projected inside B. Even though the area of A would generate a shadow which could be entirely inside the perimeter of surface B, the largest part of the surface would be visible (as the shadow of A is small). In this scenario and with this methodology, surface B will be classified as unexposed. Another example would be when one slender surface A causes a shadow on a regular surface B. In that case, surface B would be classified as being in the shadow, whereas the largest part of its surface would be visible as the shadow from surface A is also slender. Alternatively, the slender surface A could generate a shadow onto multiple neighboring surfaces, whereas surface A will only classify one of those surfaces as being in the shadow, as surface A only has one centroid. These examples would only occur when there exist significant differences between the sizes and dimensions of the different surfaces. However, all surfaces are approximately the same size and shape. Additionally, the entire spacecraft model contour is still smooth, even though it is discretized with different triangular surfaces. As a result, if a surface B would be incorrectly classified as covered by surface A, surface B will partly be covered by surfaces neighboring to surface A as well, making the misclassification less severe. The only critical case will be when the boom causes self-shadowing on the satellite; a situation which is investigated

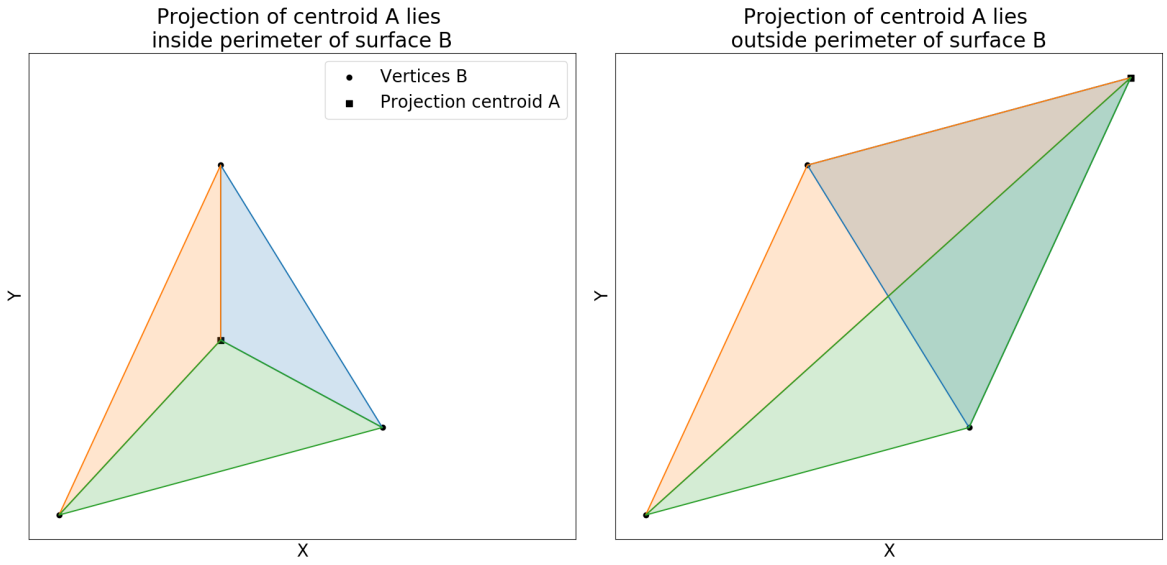

Figure 5.5: Illustration of the projection of the centroid of surface A onto the plane in which surface B lies. The projection of surface A lies within the perimeter of surface B on the left, and outside of it on the right. Clearly, the sum of the colored triangles is equal to the area of surface B on the left: surface B is classified as not exposed. On the right, the colored triangles clearly do not add up to the area of surface B: surface B will be exposed to the Sun.

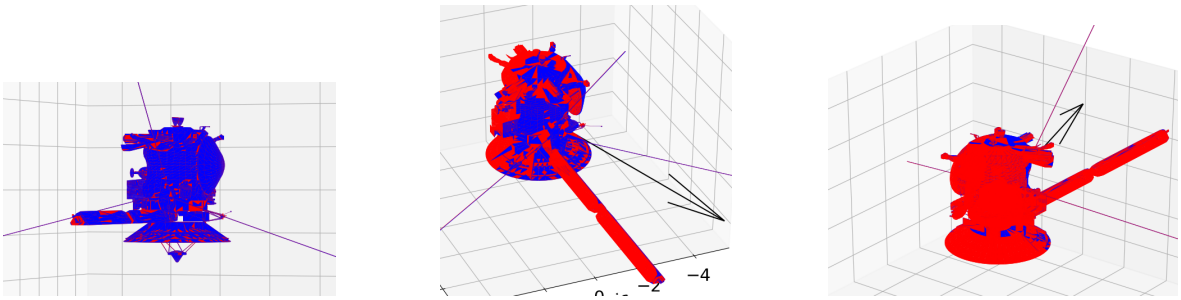

Figure 5.6: Performance of the surface classification method using the most accurate model (25376 surfaces), plotted from three different angles. The black vector is the vector pointing towards the Sun, coming out of the plane in the left figure. Visible surfaces are indicated with the blue color, red surfaces are unexposed surfaces.

in Section 5.3. Therefore, the above examples on misclassification are unlikely to occur in the analysis and the projected centroid approach is a valid assumption for surface exposure classification.

5.3. Performance of models

The performance of the chosen methodology has to be assessed. All surfaces will be plotted to show and see which surfaces will be selected as visible and which will not, from the Sun's perspective. Results are shown for the most accurate 25376 surfaces model in Figure 5.6. The results are promising: only a couple of surfaces are selected to be visible where they should not be and a couple of them are not visible where they should be in direct sunlight (Figure 5.6). Visual inspection thus suggests that the introduced error from the assumptions made in Section 5.2 is low, given the small percentage of incorrect classifications.

In order to determine how accurate the spacecraft model needs to be, different models need to be compared to the most accurate solution. Since real time accurate measurements of the SRP on the Cassini spacecraft are non-existent, the best model at hand is the proposed SRP model with the most accurate 3D model of the Cassini spacecraft consisting of 25376 surfaces. The magnitude of the calculated SRP force conforms with earlier estimations on the magnitude of the SRP force (e.g. Bertotti et al. [2003]). One major disadvantage of using the most accurate spacecraft model, is the computing time of one epoch in the flyby: determining the SRP at a certain point in time during a flyby takes about a day to compute, using one core. Even with all available computing power at the University of Technology Delft (60 available cores at maximum), it would take approximately 288 days to

Table 5.1: Difference for two spacecraft models (500 and 1500 surfaces) with respect to the most accurate spacecraft model (25376 surfaces). The CPU time is based on the time that one core takes to perform the calculation. The directional error (in arc-sec) is shown in brackets behind the percentage error in magnitude.

Model [faces]	Force (x, y, z) [N]			CPU time	Error [%]
25376	$9.854 \cdot 10^{-11}$	$-3.065 \cdot 10^{-10}$	$-5.784 \cdot 10^{-14}$	$\sim$ 1 day	-
1500	$9.357 \cdot 10^{-11}$	$-2.911 \cdot 10^{-10}$	$-4.231 \cdot 10^{-14}$	$\sim$100 s	5.0 (14.82″)
500	$8.2725 \cdot 10^{-11}$	$-2.573 \cdot 10^{-10}$	$-4.855 \cdot 10^{-14}$	$\sim$12 s	16.1 (2.06″)

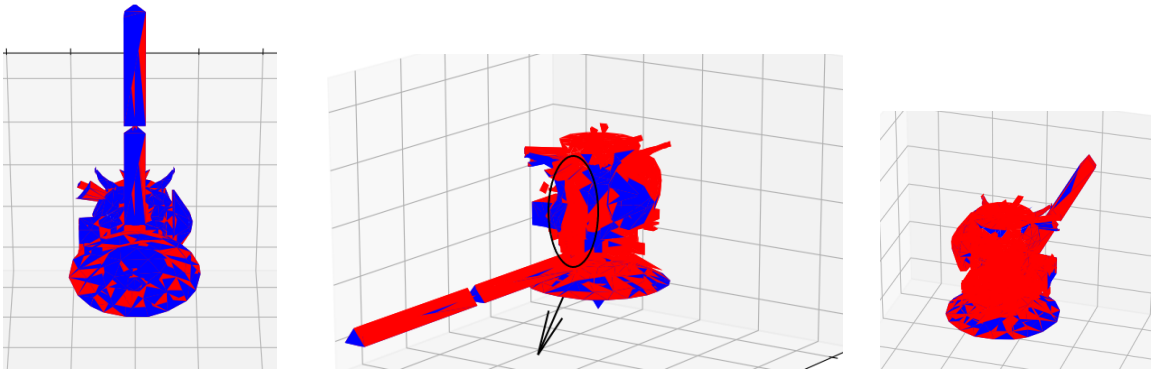

(a) From Sun's perspective (b) Substantial self-shadowing of the magnetometer boom (c) Sun is approximately behind spacecraft

Figure 5.7: Performance of the method using a model of 1500 surfaces in its most critical position; the magnetometer boom introduces substantial self-shadowing indicated in sub-figure b). The arrow points to the position of the Sun. Red surfaces are not exposed to the Sun, whereas blue surfaces are.

compute the SRP force during a flyby with an arc spanning two days at 10s increment. Hence, a less complex spacecraft model needs to be selected. Two spacecraft models will be compared to the most accurate (25376 faces) solution: 500 and 1500 faces.

These models are compared with the calculated SRP for the most accurate model from an epoch during flyby T011 (see Figure 5.6). In the same way, the SRP force for these two models are calculated. Other parameters of the calculation, such as computing time, have been monitored as well. In table 5.1, the calculated SRP forces, as well as other parameters on which the model will be chosen, are shown. The error is based on the difference in absolute magnitude of the SRP force from the 25376 faces model, therefore the error for that model is not indicated.

From Table 5.1, it can be concluded that the model for 500 surfaces is relatively fast, yet it estimates the magnitude of the force quite inaccurately. The 1500 surfaces model performs significantly better on the accuracy of the magnitude. The directional error is shown in brackets behind the error in magnitude, and is negligible for both models. The 1500 surfaces model is significantly slower compared to the 500 surfaces model. The CPU time is monitored based on the performance of a core from the servers at TU Delft. To calculate the SRP for ten flybys spanning a time period of a maximum of three days, all the calculations take a combined total of several weeks. Given that the computed data are not to be used immediately, the increase in accuracy obtained with the 1500 surfaces model is worth the extra processing time. Hence, the 1500 surfaces model is used for the SRP acceleration calculations. The majority ($\sim$1100) of the surfaces have a surface area below 0.1 m^2 and about 300 surfaces have an area below 0.2 m^2. The largest area is 1.5 m^2, which belongs to the magnetometer boom. Most surfaces have small and approximately equal sizes, therefore the assumption that a surface is unexposed if a centroid from another surface lies in front of it from the Sun's perspective (Section 5.4) are well justified.

This assumption could be violated if the magnetometer boom causes self-shadowing on the spacecraft, which had to be verified as well. Figure 5.7 illustrates the performance of the model in the most critical Sun-Cassini orientation, where the magnetometer boom introduces self-shadowing onto the spacecraft. We conclude that the model properly captures self-shadowing of the magnetometer boom, even though the discretized surfaces of the magnetometer boom are on average larger than the other discretized surfaces. Therefore, the results are accurate in this position as the SRP model selects the right surfaces to be classified as exposed. Note that several of these surfaces in the plot seem to be incorrectly classified, though this is more a flaw of the visualisation rather than the actual implemented model: both sides of a (2D) surface will be highlighted with blue or red, depending on

whether the surface is visible or not.

It has been shown that the SRP model can be severely improved by implementing a more accurate spacecraft surface model. The simple box-wing method introduces substantial errors due to the inaccurate representation of the actual spacecraft. The 1500 surfaces model proposed for implementation estimates the SRP significantly better, with the implementation of self-shadowing (Figure 5.7), well captured by the methodology and the developed SRP model proposed in this chapter.

5.4. Program to determine SRP

The methodology from Section 5.2 has to be translated to code. As noted, the most difficult task is to classify the surfaces as exposed and not exposed to the Sun. In essence, the projected centroid methodology involves mainly vector algebra and deducing trigonometric relations between the triangles. Once a surface is classified as exposed, it is straightforward to calculate the SRP on that surface with Equation 5.1. The SRP force is calculated at epoch intervals of 10 seconds during an arc, with the arc boundaries being extended by four hours.

Given the time at which the SRP needs to be calculated, the position of the Sun and the spacecraft orientation can be determined with the SPICE toolkit [Acton et al., 2017]. The positions of celestial bodies can be determined by loading spk kernels in SPICE, and the orientation of spacecraft coordinate frames can be loaded and found by loading coordinate frame kernels.[2] Unfortunately, these coordinate frame kernels do not contain data for the entire span of the flybys, hence gaps occur in the coordinate frame file. In total, there are 46 gaps for all flybys combined, where it happens only six times that these gaps are longer than five minutes, with the majority being smaller than two minutes. Cassini can perform a 180 degree slew around the Z-axis in ∼16 minutes and ∼25-30 minutes around the X- and Y-axis [Brown, 2016]. The spacecraft hence does not spin very rapidly and its orientation will not change drastically with respect to the Sun. Besides, the actual SRP calculated for a specific time (eventually to be implemented in GEODYN II) will be executed based on an eighth order Lagrange interpolation. In other words, if the SRP force at a time is requested with no explicit information on the orientation of the spacecraft, this information is implicitly included in the calculated SRP force right before and after these gaps. Hence, the SRP force can still be adequately estimated during these time gaps.

From the position of the Sun and orientation of the spacecraft, the code first calculates which surfaces are in direct sunlight. It starts with a surface (A) and checks for every other surface, whether that surface lies behind surface A, thus looping over all the other surfaces (see Section 5.2). This is monitored by a simple list of booleans, which is initialized by all surfaces being in direct sunlight. Exposed surfaces are given boolean True. Thus, the boolean in this list will change to False if the surface is found to be behind another surface. After it is checked for every surface whether surface A lies in front of it, surface A should be changed to another surface with the procedure being repeated. In that way, it is determined which surfaces lie behind that other surface A. In essence, we have to loop over all the surfaces in the spacecraft model for surface A as well, such that it is checked that a certain surface is not behind *any* other surface. However, if somewhere during this process the surface is already found to be behind a different surface (i.e. the boolean from the list is False), then it is not relevant to check whether it is also behind another surface. Therefore, this determination process is skipped if the surface is already unexposed. In summary, this determination process consists of an outer and an inner loop. The outer loop being dedicated to surface A, with the inner loop going over all the other surfaces except A (A cannot be behind or in front of itself).

Having obtained the complete list of visibility booleans, the actual SRP force is calculated, utilizing Equation 5.1. The individual force exerted on every surface area is calculated and added to the total SRP force. The total SRP force has been verified: the direction of this force is opposite to the position of the Sun, hence in the direction pointing directly away from the Sun. The calculated SRP force will be stored with the corresponding ephemeris time. This is done for every 10 second epoch during the flyby to be able to perform a Lagrange interpolation when finally implementing the SRP force into the orbit determination process, such as GEODYN II.

The table files which save these SRP forces at different times, are in the following format. The first column is the ephemeris time, and the other three columns denote the x, y, and z component of the calculated SRP in that order, respectively. Most importantly, the calculated SRP force is in units of m/s^2; thus it is a force per unit mass, visible from Equation 5.1 as well. The force is calculated and stored in the table files in the spacecraft body fixed coordinate system (in SPICE: CASINI_SC_COORD).

[2]For these kernels, see `https://naif.jpl.nasa.gov/pub/naif/CASSINI/kernels/`

5.5. Conclusion

This chapter proposes an accurate SRP model based on a detailed spacecraft model consisting of 1500 surfaces in total. For all these surfaces, the SRP calculation program from this chapter calculates which surfaces are classified as exposed to the Sun. The methodology of surface exposure classification is based on the projection of the centroids of all the surfaces, yielding good results as illustrated in Figure 5.6. The detailed SRP model from this chapter results in an accurate representation of the SRP force, which models the SRP force better than the adopted SRP models from previous research, since the implemented spacecraft model is significantly more detailed and realistic (Figure 5.1).

The current dynamic force model from Chapter 2 and the dynamic force model from Durante et al. [2019] differ significantly. As noted, our dynamic model contains empirical accelerations in three directions (radial, along- and cross-track) whilst Durante et al. [2019] does not mention applying empirical accelerations. Yet, our research from Chapter 2 argues that empirical accelerations are necessary for the analysis of Titan's gravity field with our dynamic model. The different dynamic models (Chapter 2 and Durante et al. [2019]) lead to discrepancies between several important parameters of Titan's gravity field. Consensus on the magnitude of several important gravity and tidal parameters (J_2, C_{22} and k_2) should first be reached, before the estimates of the parameters can be further improved by increasing accuracy of forces with small orders of magnitudes, such as the SRP. Hence, the implementation of this SRP model is left for future research.

6

Verification and Validation

Verification and validation is necessary to determine the validity of the utilized and designed programs. The need for verification is especially high in this field, as it is not always possible to validate the programs given that there are not always available data from the real world. Two programs, which were not specifically designed for this thesis, but slightly altered, have to be verified. In the first section, the orbit determination software GEODYN II is partly verified; this software has been in use for decades now, and has been applied in the orbit determination process of several satellites (see e.g. Goossens and Matsumoto [2008], Mazarico et al. [2014], Mazarico [2004]). The fundamental difference of the dynamic model in the Saturnian system and that of other analyzed planetary systems so far, are the addition of several more third bodies: the other moons of Saturn. The verification is about investigating the third body perturbation forces, as in the Saturnian system with a lot of moons, this is significantly different from the Mercury planetary system for example [Mazarico et al., 2014]. The other program to be verified is the actual parameter estimation program, written and maintained by P.N.A.M. Visser at the University of Technology Delft. This program takes all the normal matrices from the different arcs, combines them, and estimates the parameter adjustments. The latter comes down to solving a linear matrix equation. Further explanation on the methodology of the inversion software is also given, as the literature does not provide one clear method of applying constraints to the estimated parameters ($\overline{W}_k$ in Equation 1.10).

6.1. Third body forces

During the internship, it was found that some perturbing bodies were placed incorrectly in the environment of GEODYN II, resulting in wrong calculations of the third-body perturbation forces. Hence, before starting the analysis and estimating least squares orbit solutions for the Cassini spacecraft around Titan, it is necessary to verify if all the perturbing bodies are placed inside GEODYN II correctly. Third body forces are calculated using the following equation [Tapley et al., 2004]:

$$\mathbf{f}_{3B} = \sum_{j=1}^{n_p} \mu_j \left(\frac{\boldsymbol{\Delta}_j}{\Delta_j^3} - \frac{\mathbf{r}_j}{r_j^3} \right) \tag{6.1}$$

where n_p is the total number of third bodies taken into account (18 for Titan, see Chapter 3), μ_j is the gravitational parameter of body j, $\boldsymbol{\Delta}_j$ is the position vector of the body j with respect to Cassini, and $\mathbf{r}_j$ is the position vector of the body j with respect to Titan. It is crucial that these forces are applied correctly, because in this work an improved spacecraft model for a more accurate calculation of the SRP force is proposed. The SRP force in itself is small ($\sim 10^{-10}$ m/s^2), [Benedetto, 2010-2011]. Hence small discrepancies in other forces acting on the spacecraft could lead to incorrect conclusions on the more detailed SRP model to be applied in future analyses.

During the internship at NASA GSFC, with the most recent version of GEODYN II, errors were found in the position of Saturn. GEODYN II took Saturn's position to be equal to the position of Saturn's barycenter, which leads to a significantly mismodeled gravity acceleration due to Saturn on the Cassini spacecraft. Consequently, the iterations for the different orbit determinations for every flyby did not converge properly, or converged to an insufficiently high RMS of the observation residuals. To resolve this issue, Saturn's position is interpolated using an eight order Lagrange polynomial from known Saturn positions at different ephemeris times, similar to the approach of updating positions of Saturn's moons as explained below.

The positions of the eight heaviest moons of Saturn were loaded and approximated using Chebyshev polynomials, adopted from the most recent ephemeris kernels provided by the navigation team of NASA JPL and stored inside an external ephemeris file. During the internship, the external ephemeris files contained Chebyshev coefficients valid for only one day. The approximated positions using these coefficients were accurate within several cms. Later on during the internship, the period of the external ephemeris files had to be increased such that the coefficients were valid for at least the entire duration of the arc-length of the flyby. GEODYN II positioned Titan incorrectly during twice the light-time (round trip time from Titan-Earth) at a discontinuous boundary in the external ephemeris file, hence the need for the period extension. Periods of the Chebyshev coefficients have to be the same for all the loaded body inside the external ephemeris, and therefore the periods of the coefficients was increased to six days. It was no longer checked whether the positions of the other moons (and hence the calculated third body forces) remained correct. In fact, it was found during this thesis, that positions of these moons did not agree with their actual positions. The period of the Chebyshev coefficients corresponding to Titan had to be at least three days to prevent discontinuities; a period too long to approximate the position of inner Saturnian moons (orbiting Saturn in 30 hours). Therefore, a different solution was developed to update the positions of the Saturnian moons.

The state vector of the eight heaviest moons of Saturn are interpolated inside the GEODYN II program with data generated from ephemeris kernels provided by the Navigation team of NASA JPL.[1] The top eight heaviest moons of Saturn are Mimas, Enceladus, Tethys, Dione, Rhea, Titan and Hyperion. For every moon, a table with state vectors of the moon with respect to the Sun at different times in the J2000 reference frame is made from these ephemeris kernels and the SPICE toolkit [Acton et al., 2017]. The table spans the arc-length of the flyby including a four hour extension of the start and end boundaries. Finally, GEODYN II calculates the position of a moon by fitting an eight order Langrange polynomial through the data in the table. The position of Saturn is also calculated with this methodology.

For determining whether a third body force is calculated correctly, we use the SPICE toolbox created by the NASA JPL Navigation and Ancillary Information Facility [Acton et al., 2017]. This toolbox consists of several functions which allow the user to obtain positions of bodies with respect to other bodies or satellites from loaded ephemeris files. Using SPICE, it is possible to calculate the third body forces manually, knowing the gravitational parameter of the perturbing body and its position with respect to Titan and Cassini. Third body forces in GEODYN II are directly printed to a file to be able to compare them to SPICE at a certain epoch in the flyby. To allow for comparison, GEODYN II and SPICE are given the same trajectory for Cassini; GEODYN II determines Cassini's orbit, which in turn is loaded by SPICE through the use of a satellite and planet (SPK) kernel. In essence, we will verify whether GEODYN II has implemented the correct position of the different Saturnian moons as well as other third bodies, by comparing calculated third body perturbation forces from GEODYN II and SPICE.

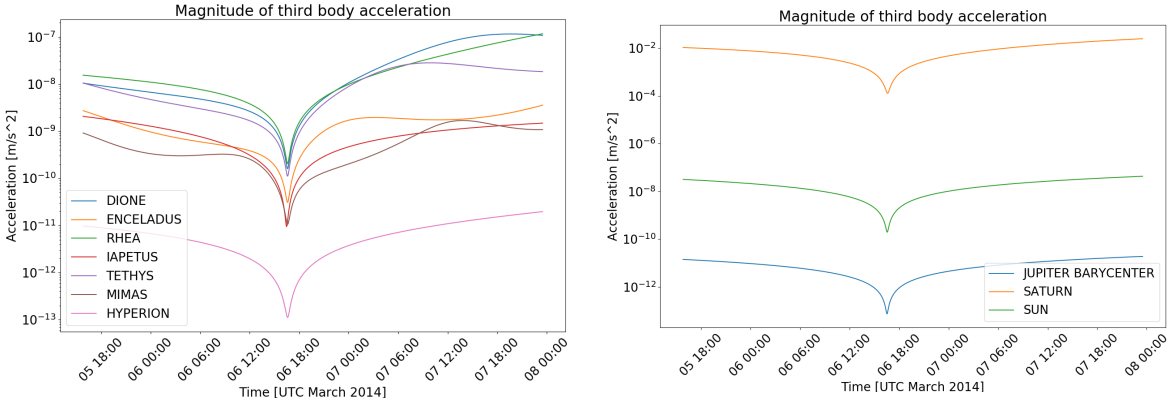

(a) (b)

Figure 6.1: Magnitude of the third body forces of a) several moons of Saturn and b) Jupiter's barycenter, Saturn and the Sun.

The comparison of the third body forces during a flyby in GEODYN II and SPICE is done for multiple randomly picked flybys, with the idea that if the third body forces are correct for several flybys, they are correct for all flybys. Most importantly, the largest third body forces are those from Saturn, the Sun, Jupiter, and all moons of Saturn with substantial mass (top eight heaviest moons). In Figure 6.1, the third body acceleration is plotted

[1] These are taken from the NAIF website `https://naif.jpl.nasa.gov/pub/naif/CASSINI/`

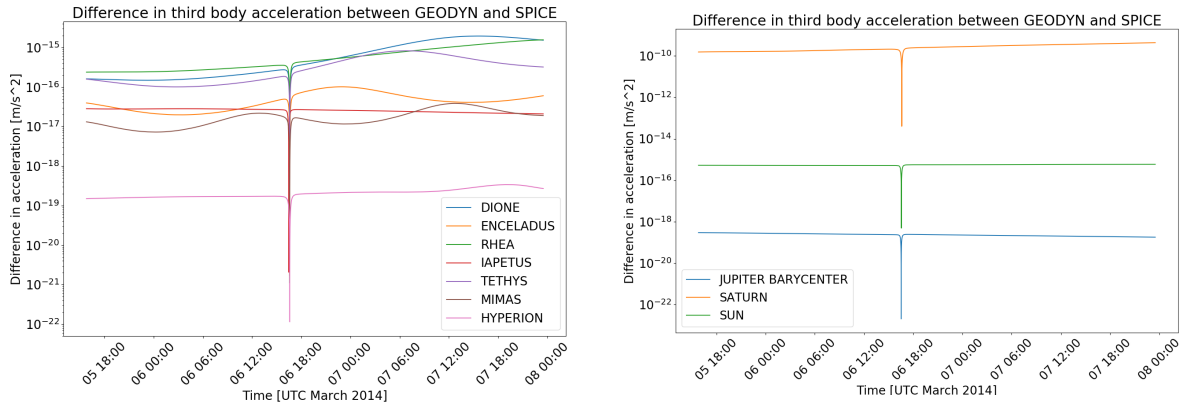

(a) (b)

Figure 6.2: Difference of third body accelerations between GEODYN II and SPICE of a) several moons of Saturn and b) Jupiter's barycenter, Saturn and the Sun.

for the aforementioned, most important bodies during flyby T099. In Figure 6.2, the differences between what GEODYN II and SPICE calculated as third body accelerations is plotted against time for the different celestial bodies.

Figure 6.1 illustrates that Saturn contributes most to the sum of third body perturbation forces acting on Cassini. Note that Saturn is in fact a third body perturbation force, as the satellite performed flybys of (orbited) Titan, hence Titan is the main body. Comparing third body force differences between SPICE and GEODYN II, the differences of forces from Saturnian moons are insignificant (Figure 6.2a). For Saturn (Figure 6.2b), the differences between GEODYN II and SPICE are in the order of 10^{-10} m/s^2. The SRP force is in the order of 10^{-10} m/s^2 and one could say that this relatively large difference between SPICE and GEODYN II for Saturn's third body force could be problematic, especially if the influence of a more accurate SRP model is to be investigated. Yet, the adopted dynamic force model for the Cassini spacecraft inevitably contains uncertainty which cannot always be resolved.

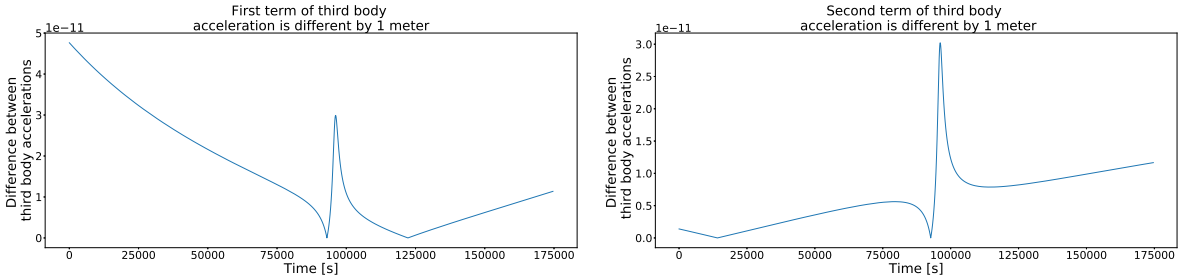

(a) (b)

Figure 6.3: Calculated difference in third body acceleration for Saturn if the vector in the first term of Equation 6.1 has a one meter offset (a) and if the second term would have a one meter offset (b).

For example, the kernels from the Navigation Team of NASA JPL contain uncertainties as the positions of celestial bodies are monitored and propagated based on observations and models. Many of the models contain uncertainties due to absence of accurate knowledge on tidal dissipation [Fuller et al., 2016, Tyler, 2011], Saturn's frequency dependent tides, and Saturn's pole motion [Durante et al., 2019]. Whilst it is difficult to know Saturn's position with complete accuracy this fact has consequences; a one meter difference in position of Saturn, could result in a calculated difference in third body acceleration of order 10^{-11} m/s^2, see Figure 6.3. Hence, even small inaccuracies in Saturns position could cause an inaccurate calculation of the third body perturbing acceleration.

The position of Saturn in GEODYN II is, however, almost identical to the one from SPICE (Figure 6.2b) due to the interpolation of Saturn's position. Likewise, positions of moons at different epochs from SPICE are used for interpolation to determine the position of a certain moon at a certain epoch. This leads to sufficiently accurate position coordinates for the moons of Saturn in GEODYN II. Since inaccuracy of positions of third bodies inside the Saturnian system remains in the order of several meters at least, inaccuracies are introduced inevitably. In

addition, SPICE also interpolates the state of the third bodies, usually through the use of Chebyshev coefficients, which in itself introduce small inaccuracies in the order of centimeters as well.

Additionally, part of these differences could be caused by floating point errors in Python, which is used to compare the third body forces between SPICE and GEODYN II. Both terms in Equation 6.1 (before being multiplied by μ) are of the order of $1.0 \cdot 10^{-19}$, and computer inaccuracy could occur at these small numbers.

6.2. Inversion software

Inversion software estimates adjustments of the estimated parameters, such as satellite states, gravity coefficients and empirical accelerations. In reality, the orbit problem is a non-linear problem, involving non-linear equations for the dynamics of the satellite as well as the observations of the instruments on the satellite. These equations need to be linearized at a certain reference position: the initial conditions of the problem [Tapley et al., 2004]. See Chapter 1 or Tapley et al. [2004] for a more detailed explanation. The fundamental equation after linearization of the dynamical and observation equations is [McCarthy et al., 2015]:

$$d\mathbf{x}^{(n+1)} = \left[B^T W B + V_A^{-1}\right]^{-1} \left[B^T W \mathbf{y} + V_A^{-1}\left[\mathbf{x}_A - \hat{\mathbf{x}}^{(n)}\right]\right] \tag{6.2}$$

where

$d\mathbf{x}^{(n+1)}$	is the change of the estimated parameters ($\hat{\mathbf{x}}_k$ in Equation 1.10)
B	is the matrix of partial derivatives of the observations to the estimated parameters (design matrix);
W	is the weight matrix of the observations;
V_A^{-1}	is the *a priori* covariance matrix, consisting of the constraints put on $\mathbf{x}_A$ ($\overline{W}_k$ in Equation 1.10);
$\mathbf{y}$	is the vector of residuals of the observations from the n^{th} iteration;
$\mathbf{x}_A$	are the *a priori* estimates of the parameters and;
$\hat{\mathbf{x}}^{(n)}$	is the n^{th} solution of the parameters from the iteration process.

This equation is similar to Equation 1.10, though note that here $\mathbf{x}$ denotes the actual state, rather than the change in the actual state as in Equation 1.10. The estimated parameters $\hat{\mathbf{x}}^{(n)}$ at iteration n consist of both common and arc parameters (Equation 6.2). Whilst common parameters are valid for every arc, arc parameters are unique for every arc. Gravity and rotational elements of the primary body (Titan) are common for example, as they influence every arc similarly. Satellite states, SRP coefficients, and empirical accelerations are arc specific (as these differ per flyby). Prior to the inversion process, an independent orbit determination for every arc is executed: no global parameters are estimated. GEODYN II calculates optimal/converged solutions of the arc parameters for every arc. Then, GEODYN II is given these calculated converged arc parameters of the previous run with which it does a next orbit determination. This immediately confirms the previous optimal solution - or illustrates that this was only a local minimum; flybys are very unstable, hence it could very well be the case that GEODYN II only finds a local optimum at the first run. Additionally, the orbit determination of this arc is now done with improved *a priori* values of the estimated parameters. Inaccurate *a priori* values are given to the empirical accelerations and observation biases during the first set of arc iterations, as their magnitude and sign is unknown *a priori*. The converged values of the parameters after the first set of arc iterations can now also be used for $\mathbf{x}_A$ in Equation 6.2, instead of the much less accurate *a priori* values in the first run, making this term in the equation less dominant.

As a result of these separate orbit determinations for every arc, GEODYN II outputs the normal matrices of every arc ($B^T W B$ in Equation 6.2). This inversion software has been used for a very long time within the TU Delft. Yet, small changes had to be made in order for it to be applied to this system of flybys, hence the need for verification.

Verifying the results of the inversion software will be done by comparing the results of software used at NASA Goddard using the same setup of the problem, i.e. the same constraints on the parameters and weights for normal matrices and residuals. Directly comparing the outcome of Goddard's software and the software used at the TU Delft has led to significant differences in the solution. As such, we have to verify that the underlying implemented equations are equivalent to allow for comparison. The inversion process generally is a simple matrix inversion, where weights for every arc and parameter constraints are applied differently in different inversion software programs. Therefore, a separate Python program was made in order to find out how the equations (such as Equation 6.2) are applied. The results of Goddard's software were reproduced with this Python program.

Slight differences exist between these two programs, regarding the processing of the normal matrices. Goddard's software uses a batch approach which makes one large normal matrix ($B^T W B$ in Equation 6.2) for the entire system of flybys/arcs, and performs the inversion from the vantage point of this large matrix, consisting of

both arc parameters and global parameters. The software from the TU Delft uses partitioning; a procedure where the inversion is split into a global parameter part and an arc-specific part [Pavlis et al., 2006]. The partitioning and batch schemes are small differences and should not affect the final solution of the problem (apart from rounding errors/computer accuracy).

One fundamental difference between the programs exists. In Goddard's software the normal matrices (and residuals) of every arc are multiplied by the respective weight of the arc before they are combined in big normal matrix (and vector). Hereafter, the *a priori* covariance matrix is added to this large normal matrix with a weight of unity. The fundamental difference with TU Delft's software is that this software also weights the corresponding covariance matrix of every flyby/arc with the weight given to that flyby/arc. Although, neither of these approaches is by definition false, the covariance matrix is usually weighted with a weight of unity. The covariance matrix consists of the different constraints applied to the parameters. These constraints should be equivalent for the same type of parameters irrespective of which arc they belong to. Specifically, the constraint should prevent a type of parameter from growing or shrinking to unrealistic high or low values. A perfect example would be the empirical accelerations, which are always constrained, as they otherwise will absorb most (if not all) of the signal (Chapter 4). Furthermore, by setting a constraint of for example 1000 meters for the state position, we do not want the solution of the inversion to give us a state deviation that is orders of magnitudes smaller (or larger) due to the fact that the constraint is weighted according to the importance of the flyby. A low weight on the constraint would then mean that the applied constraint is tighter than initially intended, and vice versa for a large weight.

The *a priori* state $\mathbf{x}_A$

Further attention should be paid to the term on the right hand side, $V_A^{-1}\left[\mathbf{x}_A - \hat{\mathbf{x}}^{(n)}\right]$. Here $\mathbf{x}_A$, according to the definition in McCarthy et al. [2015], is the *a priori* condition of the state $\mathbf{x}$. However, it is a common misconception that this is per definition the starting value of the state. Looking at it from a statistical perspective, $\mathbf{x}_A$ should be a preferred state, which does not necessarily have to be equal to the values that $\mathbf{x}$ started with. GEODYN II does make use of this last term in equation 6.2, but with the inversion software we chose not to use this last term: $\mathbf{x}^{(n)}$ is a 'better' state because the converged solution/state is the state at which the residuals are minimized. Hence, then it is appropriate to say that $\mathbf{x}_A = \hat{\mathbf{x}}^{(n)}$, because $\mathbf{x}^{(n)}$ is commonly a much better representation of the true value of the state than its initial values would be, especially considering that non-physical parameters, such as empirical accelerations, can never be known beforehand as these parameters basically absorb subsequent errors made in the dynamical model. Of course, the estimate $\mathbf{x}^{(n)}$ is only a much better representation of the *a priori* state $\mathbf{x}_A$ if the implemented dynamic force model is correct. If the dynamic model is inaccurate, the solution $\mathbf{x}^{(n)}$ at which the residuals are minimized, is most likely not equal to the true value of the state. However, we expect the implemented dynamic model to be correct, justifying the assumption that $\mathbf{x}_A = \hat{\mathbf{x}}^{(n)}$.

Yet, this reasoning does not apply if a Kaula constraint is applied. In gravity field determination and analysis, an empirical Kaula constraint could be applied to constrain the higher spherical harmonic degrees of the gravity field, as not to absorb a disproportional amount of the signal [Kaula, 1966]. The Kaula rule constraints the total power of a spherical harmonic degree. The power can be calculated as:

$$\sigma_l = \frac{\sqrt{\sum_{m=0}^{l}\left(C_{lm}^2 + S_{lm}^2\right)}}{\sqrt{2l+1}} \tag{6.3}$$

where C_{lm} and S_{lm} are the normalized spherical harmonic coefficients and σ_l is the power of the spherical harmonic coefficients of degree l. The Kaula rule then constraints the power of degree l as follows:

$$\sigma_l = \frac{K}{l^2} \tag{6.4}$$

where K is called the Kaula factor which is usually a small number. For Earth, this value is found to be 10^{-5}, consistent with the determined gravity of Earth from satellite tracking and gravimeters [Kaula, 1966]. The Kaula constraint (Equation 6.4) is used as an *a priori* estimate for the power of spherical harmonic gravity coefficients of celestial bodies and is hence added to the *a priori* covariance matrix V_A from Equation 6.2. The gravity field from other celestial bodies is not determined from gravimeters directly, as they do not have gravimeters on the surface. Kaula factors for other celestial bodies should hence be scaled and estimated accordingly. McMahon et al. [2015] proposes a method to apply the Kaula constraint to other celestial bodies in the solar system, by scaling the Kaula factor by the ratio of the surface gravity of the celestial body and the Earth squared. This does

not apply to unusually small bodies, and one can also argue whether this scaling rule is applicable to icy bodies such as Titan and Enceladus [Durante et al., 2019].

What a Kaula constraint essentially does, is forcing the solution for the spherical harmonic coefficients to their *a priori* value $\mathbf{x}_A$, depending on the strength/magnitude of the Kaula factor. A stronger constraint is one which forces the power of (higher) degrees to be lower, corresponding to a smaller Kaula factor. A strong Kaula constraint hence forces the solutions of the spherical harmonic coefficients to their *a priori* values, which are usually zero. In order for the Kaula constraint to be applied the way it was intended to, the term $V_A^{-1}\left[\mathbf{x}_A - \hat{\mathbf{x}}^{(n)}\right]$ in Equation 6.2 cannot be absent. In the TU Delft software, this term is absent, making the correct application of a Kaula constraint impossible with the program as it is. Hence, to apply the Kaula constraint correctly, $d\mathbf{x}^{(n+1)}$ needs to come down to $\mathbf{x}_A - \hat{\mathbf{x}}^{(n)}$, such that $\mathbf{x}^{(n+1)} = \mathbf{x}^{(n)} + d\mathbf{x}^{(n+1)} = \mathbf{x}_A$ with $\mathbf{x}_A$ usually being equal to zero for the spherical harmonic coefficients (Equation 6.2). If a very strong Kaula constraint is applied, the dominant matrix is the covariance matrix (V_A in 6.2). We immediately note the importance of the term $V_A^{-1}\left[\mathbf{x}_A - \hat{\mathbf{x}}^{(n)}\right]$: without this term, $d\mathbf{x}^{(n+1)}$ would become zero.

The discrepancy between the software at TU Delft and NASA GSFC was found to be due to a difference in applied weights. The partitioning methodology has been dropped, and the TU Delft software now performs a batch weighted least squares approximation of all the normal matrices from all the arcs combined, similar to the software at NASA GSFC. The constraint matrix is added to this combined normal matrix with a weight of unity, see Equation 1.13.

7

Conclusion

The objectives of this work are to determine the gravity field of Titan with Doppler tracking data from the Cassini mission, investigate the effects of global constraints on the overall gravity solution, and obtain a more detailed solar radiation pressure (SRP) model. In Chapter 2 and 3, a converged solution of the 3x3 gravity field of Titan has been proposed. Both differences and similarities are found when comparing this solution with previous research. In addition, the design of a more sophisticated SRP model is explained in Chapter 5, which implements a more detailed version of the spacecraft model rather than the simpler box-wing panel model implemented in previous studies on the gravity field of Titan [Durante et al., 2019, Iess et al., 2012]. Several improvements are possible in both the analysis and the stability of the proposed gravity field solution of Titan. These are outlined at the end of this chapter.

7.1. Conclusions

Determining the gravity field and tides of a celestial body is of interest for two reasons. Firstly, they provide information on the history and formation of the celestial body. Secondly, information on the distribution of mass and raised tides can aid in determining the interior structure of the celestial body in general. For the class of icy moons, this is especially interesting, given the fact that several of these celestial bodies could harbour a sub-surface ocean habitable for extra-terrestrial life. Titan is one such icy moon, hence determining its gravity field yields valuable constraints on interior structures leading to a correct assessment of likely interior models. As such, we estimate Titan's gravity field up to spherical harmonic degree three, implementing different processing and estimation strategies, different forces and measurement models, and different orbit determination software compared to earlier estimations of Titan's gravity field.

It is important to highlight the ill-posedness of this orbit and gravity determination problem. Only ten short-arc flybys with Doppler tracking data are considered in the data analysis. Besides this lack of data, Titan's surface is not sampled optimally. High latitudes are poorly sampled, specifically the North-Eastern Hemisphere. Both of these factors lead to the aforementioned significant correlations between gravity parameters and the tidal Love number k_2. As a result, it is difficult to determine these parameters uniquely, if the correlations are not resolved in any way.

Durante et al. [2019] has estimated a 5x5 gravity field including k_2 Love number by implementing small constraints on all parameters, including global parameters. A valuable finding of this study is the estimation of a stable 3x3 gravity field without applying global constraints, answering one of the research questions. We did not include the estimation of the k_2 Love number as the aforementioned correlations make it difficult to estimate a feasible value. The difficulty of estimating k_2 was also experienced by Anderson and Schubert [2013], who have not been able to determine the Love number from analyzing six flybys. Durante et al. [2019] states that the applied global constraints do not constrain the estimate. In this work we apply no global constraints as there exists no *a priori* information on these parameters to allow for physical global constraints. An analysis of the robustness of the 5x5 gravity field from Durante et al. [2019] with our dynamic model yielded solutions which differed only insignificantly (2σ). Since we found no feasible k_2 Love number whilst initializing global parameters (except μ) at zero, we can conclude that the application of (loose) constraints seems to influence the solution.

An important conclusion from our 3x3 gravity solution is our predicted lower value for the coefficient C_{22}. We propose two reasons for this. Firstly, k_2 and C_{22} have a strong positive correlation, thus including the estimation

of k_2 could increase the value of C_{22}, as $k_2 \geq 0$. Due to high correlation with other parameters however, the estimation of k_2 does not lead to a feasible solution ($k_2 \leq 0$). The application of global constraints, as done in Durante et al. [2019], could reduce this correlation. Secondly, Durante et al. [2019] applied a non-zero initial condition and constraint to the parameter C_{22}, whereas we start from a 2x2 gravity field initialized at zero and, after convergence, expand it to a 3x3 gravity field. These different approaches could lead to discrepancies as well. Additional differences in the results are represented in the formal errors, which for previous analysis are very low compared to this research; a direct consequence of the significant difference in applying weights for every arc. We determined appropriate weights (in the order of 1) for arcs based on their respective ground coverage of Titan, whereas previous research applied significantly higher weights inversely proportional to the RMS of the observation residuals.

Several similarities with previous research were found as well. An important finding is our statistically insignificant value of J_2, a crucial parameter for inferring several interior properties of Titan. In addition, we found a ratio of $J_2/C_{22} = 3.674 \pm 0.288$, which conforms to hydrostatic equilibrium ($J_2/C_{22} = 10/3$). Hydrostatic equilibrium implies that Titan's interior is fully differentiated, aiding in determining likely interior structures. This work found a moment of inertia factor of 0.342 using the Radau-Darwin equation, close to previous research [Durante et al., 2019]. The moment of inertia constraints the interior layers of Titan and thus help in determining likely interior structures. The third degree coefficients of the spherical harmonic gravity field are not directly influenced by tidal forces, rotation, and tidal heating, and can consequently be used for determination of thickness variations of Titan's ice shell at the surface [Hemmingway et al., 2013]. Formal errors on J_3 are larger than its magnitude in both this and previous research, not allowing us to make definite conclusions on its sign.

An additional valuable finding is the robustness analysis and verification of the solution from previous research, also performed in Chapter 2. Different dynamic models (with and without CoM estimations or observation biases) have shown that the solution from previous research [Durante et al., 2019] is stable after one global iteration, which indirectly also verifies our implemented dynamic model. The values of C_{22} did decrease beyond one times the formal error however. A possible explanation is that no global constraints are applied, even in the stability analysis; a fundamental difference from the approach in Durante et al. [2019].

The implemented dynamic models and strategies to process the data are different from previous research. This analysis used a different orbit determination program, GEODYN II. Small parameters, such as elevation cutoff angle, differed but were found not to make a significant difference. Previous studies have not mentioned implementing the estimation of empirical accelerations, which is remarkable given the fact that we do not find feasible solutions without them. The empirical accelerations in this analysis span a period of eight hours and were found to be quite large ($\sim 10^{-6}$ m/s^2, compared to the SRP with $\sim 10^{-10}$ m/s^2). Additionally, observation biases are estimated in our analysis for every possible combination of ground station (DSN) and satellite separately. These are usually in the order of tens of mHz. Lastly, previous research estimates Titan's state at the start of the arc. Estimating this state vector is not possible with the current version of GEODYN II in use.

For most flybys, the estimation of empirical accelerations and observation biases are necessary to fit the observation residual to the expected noise level. Observation biases can very well absorb a mismodeling of Titan's position, as this error could cause an approximately constant bias. In addition, empirical accelerations can absorb any errors in the dynamic model (depending on their period length), and are hence constrained tightly.

In Chapter 5, the design of an SRP model is outlined and explained. This design could improve the dynamic model implemented in previous and current analyses, to increase the accuracy of the estimate of the gravitational parameters and tides of Titan. This model uses a 3D Cassini panel model consisting of triangular surfaces, which together make up the surface area of the original spacecraft. It determines the SRP on each surface separately, at every ten seconds during the span of every flyby ($\pm$4hrs). The SRP force acting on the spacecraft is calculated by adding contributions from each separate triangle. Finally, the results at every ten seconds are saved, after which an interpolation in GEODYN II can determine the solar radiation pressure force at any specific time inside the flyby. Selection of the most suitable model (500, 1500 or 25376 surfaces) was a trade-off between computation time and accuracy; the model with 1500 surfaces differs by $\sim$5% from the most detailed model, whereas the 500 surface models differs by 15%. The tool is computationally expensive, hence it is not feasible to use the most detailed model. Yet, the slightly simplified model of 1500 surfaces is computationally feasible - whilst greatly improving upon the relatively simplistic model used in previous research. Implementing the SRP model could have a beneficial effect on the estimation of the gravity field of Titan, though first consensus should be reached on (all) the gravity and tidal parameters as well as the applied dynamic model. For now, the estimated empirical accelerations are still orders of magnitudes larger than the SRP force, which could make it difficult to observe the effect of the accurate SRP model.

7.2. Recommendations

The analyzed radio tracking data in this work contain X-band uplink and X-band downlink data (7.2 GHz and 8.4 GHz, respectively). There are higher frequency Ka-band downlink tracking data available with a frequency of 32.0 GHz. The uplink Ka-band data are unavailable due to malfunctioning of the Ka-band frequency translator aboard the Cassini spacecraft. X-band data have a lower frequency and are more sensitive to noise effects caused by the turbulence of solar plasma, especially for obtained data with a small Sun-Earth-Probe angle where the signal travels relatively close to the Sun. It would be valuable to include this Ka-band data and prioritize this data over the available X-band downlink data if both Ka-band and X-band data are available at the same time.

Some of the residual plots from the supplementary materials (Chapter 3) still show some remaining signal, usually around the time of C/A. Ideally, the residual plots should show a white noise like behaviour, i.e. flat residuals. It would not be difficult to get the residual plots flat: adding more empirical accelerations with small periods, with a sufficiently open constraint, will lead to absorption of signal left in the residuals. Estimating too many empirical accelerations does not benefit the validity of the implemented dynamic model as, unfortunately, the empirical accelerations also absorb signal originating from other estimated parameters. In short, estimating more empirical accelerations could result in a flat residual plot, but should be done with caution. Given the resemblance with Durante et al. [2019] for some estimated parameters and the robustness of their solution (Chapter 2), we have reason to believe that our implemented dynamic model predicts the trajectory of Cassini accurately for the entire duration of the arc. Judging from the signal present near C/A, the dynamic model can be further improved during the point of C/A however. It would hence be best to check the effect of more empirical accelerations with a lower period only near the point of C/A (where there is still signal in the residuals). For the same reason, the influence of the constraint on the drag coefficient can be further investigated as the drag force is only important near C/A.

A lot is unknown about positions and forces of objects orbiting the Saturnian system. Previous research justified estimating Titan's position based on not knowing accurately where certain bodies are within this system (accurate enough for what the data suggest). The estimation of Titan's position allows the orbit of Titan to be discontinuous. For example, estimating Titan's state vector at the start of two flybys, results in different Titan positions and velocities. Based on the implemented dynamic models (e.g. our dynamic model or the models implemented for several JPL ephemeris files), integrating the orbit of Titan from the start of one flyby to the start of the other flyby later in time will not result in the same state vector for Titan as the one estimated for the flyby later in time. The same is true for the estimation of Cassini's state vector. A method to decrease these discontinuities, or to improve the estimates of the parameters, is by implementing optical images of Titan from Cassini (e.g. Li et al. [2017]). Several studies have demonstrated the possibility of including optical images from which observed landmarks are used to estimate the satellite state vector with greater accuracy [Markley, 1987]. Other studies have shown that orbit determination can be performed with optical images and the tracking of known landmarks alone [Christian, 2019]. Although, the estimation of Titan's gravity field and tides cannot be performed merely on landmarks and optical images due to insensitivity of these parameters to the data, it can aid in performing a more accurate orbit determination of Cassini as a whole. Flyby T110 can be improved in particular, as optical imagery was performed during that flyby as well. This flyby contains a lot of relevant information on the gravity field, given its ground track. Additionally, flybys used to take optical images of Titan (and other celestial bodies) can be used to smooth the orbit of Cassini, by determining Cassini's trajectory from these images, and propagating it to the start of the arc for radio-tracking, thereby constraining and initialising Cassini's state with more knowledge and certainty.

Chapter 4 has given us valuable information on which parameters are most dominant in the orbit determination process: empirical accelerations and state parameters. Ideally, the empirical accelerations should be as low as possible as they directly describe the accuracy of the adopted dynamic model. The magnitudes of these empirical accelerations are significant however, especially when compared to influences of other forces. Hence for future research, the main focus should be on these parameters, especially since they are not at all mentioned in previous research. In this work however, they are found to be necessary. Two approaches will be proposed, where one will try to decrease the magnitude of the empirical accelerations and the other disregards the empirical accelerations completely.

First, the effect of the periods of empirical accelerations could be investigated more thoroughly. Decreasing the period of an empirical acceleration is expected to result in a smaller estimate for the empirical acceleration. This is similar to the earlier recommendation to add more empirical accelerations to the point of C/A, yet now decreasing the periods of empirical accelerations applies to all empirical accelerations. Second, the estimation of Titan's gravity and tides can be performed without implementing empirical accelerations, under the condition that an equivalent dynamic model from previous research is adopted. As a result, no observation biases and empirical

accelerations are estimated, yet Titan's state vector will be estimated. Unfortunately, this cannot be done with the older version of GEODYN II utilized for this work. It might be possible to request the newest version of GEODYN II which does have the ability to estimate and integrate Titan's orbit, however this requires NASA's consent. Alternatively, different orbit determination software (other than Monte used in Durante et al. [2019]) can be used for this; e.g. TUDAT from the University of Technology Delft.

As noted, this work obtained gravity solutions without giving *a priori* variances to the global parameters. Although in this thesis we refrain from applying global constraints, a brief analysis with the implementation of global constraints clearly large enough to not constrain the solution (applying constraints ~4 orders of magnitude larger) has not resulted in feasible estimated gravity fields including tidal Love number yet. Further analysis on globally constraining parameters is necessary to determine suitable global constraints, applicable for the gravity determination at hand. One of such suitable global constraints could also involve applying a Kaula constraint. Several Kaula constraints for Titan have been proposed in other studies [McMahon et al., 2015]. Caution has to be paid when applying a Kaula constraint however. No Kaula constraint has been verified for icy moons yet, in contrast to rocky planets for which a Kaula constraint has been verified for the Earth, based on gravimeters and gravity determination data.

A

Programs

This appendix provides an overview of all the different programs used in the analysis of the gravity field of Titan. Explanations on how to use certain programs will be provided as well, including inputs and outputs to a program.

The estimation process is roughly done in the following order. Firstly, the setups for GEODYN II are made, which consist of setting a start and end time and date for the arc, selecting which parameters to estimate (both global and arc-specific) and setting *a priori* values of not estimated parameters. Additionally, GEODYN II can be told which datapoints it should take into consideration, and which it should not (outliers). Datapoints can also be disregarded automatically (the 'EDIT' card for example, see the GEODYN II documentation for further explanations on all the available input cards[1] [Pavlis et al., 2006]). If the setups are complete and final, GEODYN II will be executed with, among others, this setup as input. After convergence, GEODYN II will output several files containing observation residuals, trajectories, normal matrices, design matrices as well as several log files telling the user what it is doing. Several subprograms have been designed to enable analysis of these outputs, such as the observation residuals. After convergence in GEODYN II, the gravity inversion can be performed by combining the normal/design matrices from the arc convergences into a multi-arc weighted least squares approximation (Equation 1.11) and solving Equation 1.13. For this, inversion software from P.N.A.M. Visser (TU Delft) will be used, though slightly modified to be compatible with this particular system of flybys. Several subprograms are designed to also analyse outputs from that software.

A.1. GEODYN II

GEODYN II consists of two parts: IIS and IIE. The subprogram IIS reads the input file, called the setup, and will read this file several times. It will read all types of data, such as tracking data, station coordinate data, and planetary ephemeris files, selects all the data to be analysed and formats it accordingly, such that the subprogram IIE can perform the actual analysis and computation. The program IIE performs all the computations, including the least squares orbit and geodetic parameter estimation.[2]

All subroutines corresponding to either subprogram, can be found in a separate folder on the TU Delft server (aristarchos/hipparchos). These subroutines are present in .f (Fortran) files, and all these are combined to make one executable: *geodyn2s* and *geodyn2e* for the subprograms IIS and IIE, respectively. In the respective IIS and IIE directories, one can find a "Makefile" which consists of code that links subroutines and dependencies of these subroutines together. Simply by typing "make" into the directory of IIS and IIE, the executables will be made.

After the executable has been made, GEODYN II can be run and the analysis of a given setup can start. Running GEODYN II is not very straight forward however, as many input files (besides the arc-setup) have to be given to GEODYN II in order for it to run correctly. For example, the gravitational coefficients of a main body potential, supplementary ephemeris, planetary ephemeris files and many more. Hence, a c-shell (.csh) script will be utilized for running GEODYN II. This c-shell script will need three inputs: IIS-setup file, flyby number (for example T068) and the directory in which the results should be printed and stored. The script itself consists of several lines, with many variables. These variables should be given the correct paths to the right input files for GEODYN II. Most of them speak for themselves, but a short summary will be given.

[1] see also `http://www.deos.tudelft.nl/AS/pieter/Local/Geodyn/index.html`

[2] For an extensive description of the GEODYN IIS/IIE interface, see GEODYN Documentation volume 5 at `https://earth.gsfc.nasa.gov/geo/data/geodyn-documentation`

- GEODYN2S / GEODYN2E: the *geodyn2s* and *geodyn2e* executables. For example, '/home/bob/bin/geodyn2s';
- SATURN_SHA_FILE: Saturn's spherical harmonics file (modification of GEODYN II specifically for the analysis of Titan);
- X_STATE_FILE: file consisting of positions and velocities at a certain ephemeris time of body X, explained below;
- EPHEM: ephemeris file of the planetary systems;
- EXTACC: external acceleration file of the Cassini satellite;
- GRAVFIELD: the gravity field of the main body
- EXTEPH: the external/supplementary ephemeris, necessary for any additional third bodies to be taken into consideration. For the Saturnian system, these include Saturns top eight heaviest moons. The order of the third bodies in this file is extremely important, explained below;
- GDNTABLE: table consisting of different values of the flux, polar motion and UT1 at different values of internal GEODYN time/ephemeris time.;
- G2B: the tracking data of the satellite (any type) to be analyzed;
- tmpexat: external attitude (quaternion) files of the spacecraft as .Z file.

After defining all these variables, these files will be linked such that they are present in the current working directory, which for the executables is the directory in which the executable writes the results. Finally, the executables *geodyn2s* and *geodyn2e* are executed. After execution, any irrelevant files will be removed.

Modifications for Cassini

The GEODYN IIE subprogram had to be modified slightly to determine the orbit of Cassini correctly. GEODYN IIE normally takes the third body planetary positions, such as Mars, Mercury and Venus, to be at the position of their respective barycenter with the total mass of that planetary system centered at that position. This would be a good approximation to the third body force contribution of Saturn on a particular satellite orbiting Earth; taking the moons of Saturn to contribute as third bodies separately, would have a negligible difference. For a satellite orbiting the Saturnian system however, this is very relevant and far from negligible, hence the moons of Saturn had to be considered separately as well. As a result, Saturn should also be placed at its actual position, rather than the barycentric position of the Saturnian system. For that process, the 'X_STATE_FILE' variables are used. These table files should consist of positions of the third body X (also Saturn is a third body) at a certain ephemeris time. The format of the files is the ephemeris time, followed by the state vector of the body X, all consisting of a total of 25 characters. GEODYN IIE will use an eight order Lagrange interpolation for determining the position of a third body at a certain time. This time should be in between the maximum and the minimum ephemeris time present in the table.

In addition, the order of the bodies in the external ephemeris file play an important role in the third body analysis. The same holds for the SCBODY cards in the IIS setup: the order is key and should not be interchanged. The SCBODY cards in GEODYN IIS setup are used to include certain third bodies, while also assigning values to certain parameters of these third bodies, such as the gravitational parameter. The order of the SCBODY cards should be matched with the order of the bodies in the external ephemeris file. Furthermore, the external ephemeris file is fixed to a definite order. This order is: Titan - Dione - Enceladus - Rhea - Iapetus - Tethys - Mimas - Hyperion. The position of these bodies is updated in GEODYN IIE, using a hard-coded index. In other words, interchanging the positions of Dione and Enceladus, will result in Dione being given Enceladus' position and vice versa. Note that also the SCBODY cards should have this same order.

Modifications for SRP

A slight modification had to be made in order for GEODYN II to take the calculated SRP from the SRP model in Chapter 5 into account. The SRP at a certain time is calculated by interpolating the SRP from the tables generated by the SRP model using an eight order Lagrange polynomial, in a similar fashion as has been done for the positions of the moons of Saturn. The magnitude of these forces has been verified, hence the interpolation goes smoothly. However, this version has to be used with caution for a couple of reasons.

Firstly, Titan's position will not be updated using the same methodology as the other moons, using an eight order interpolation and the state tables. This still has to be implemented in the code. Secondly, the partial derivatives with respect to the scaling factor usually estimated (the SOLRAD card in GEODYN II) is not verified yet. This parameter is estimated to account for a mismodeled SRP acceleration. The derivative of the acceleration with respect to this parameter is simply equal to the initial acceleration itself:

$$\mathbf{f}_{SRP,act} = C_R \mathbf{f}_{SRP,pred} \qquad \frac{\partial \mathbf{f}_{SRP,act}}{\partial C_R} = \mathbf{f}_{SRP,pred}$$

where the subscripts $pred$ and act indicate the predicted value of the SRP with the SRP model in Chapter 5, and the actual value of the SRP calculated by GEODYN II after estimation of the scaling factor C_R, respectively. Note that this C_R should not be confused with the C_R in Equation 5.2, as that represents the SRP coefficient of the spacecraft.

Utility programs

Output from GEODYN II usually only consists of binary formatted files. Therefore, several programs are necessary to transform this data to an ascii format. The following programs are used to transform certain files to an ascii format, or vice versa.

- emat2asc.x: transforms an emat file (normal matrix file) to ascii format;
- emat2bin: transforms an emat file to binary format;
- parfil2asc.x: transforms parfil file (design matrix file) to ascii format;
- reform_res_full: transforms resid file (fort.19) containing the observation residuals to ascii format. This ascii format will be used as input for several other analysis programs. (Developed by Sander Goossens)
- g2tinertial: transforms a binary orbit trajectory file to ascii format

More programs to transform between binary and ascii format are available in the GEODYN directory on the TU Delft computers (/home/pieter/Geodyn/Tools).

A number of programs have been developed to modify the IIS setup of GEODYN II as well as analyse its outputs. All of them will be listed below. Most of them are designed during this thesis, but several are merely modifications of previous programs. They can be found in /home/bob/bin/ and any sub-directory therein.

- add_accel_time: makes ACCEL9 cards for GEODYN IIS setup and stores them in file 'accelcards.inp'. If this file exists in the working directory, the program will take this file and insert these cards in the IIS setup. It requests user input: input (IIS) file, length of empiricals, and which empiricals to estimate (see GEODYN II documentation volume 3);
- add_delete: takes an old setup file, file containing DELETE cards, and new setup filename as arguments, making a new IIS setup with the added new DELETE cards;
- add_mbias: comparable to 'add_delete', instead for observation bias cards;
- add_obsWeight.py: takes an old setup, new observation weight, and new setup file name as arguments, and modifies the applied observation weight (of ramped Doppler) in the setup;
- add_offadj.py: takes old and new setup as arguments and adds an OFFADJ card to the setup;
- add_radialaccel.py: takes an old and new setup file name as arguments, and adds radial empirical accelerations to a new IIS setup;
- add_small_forces.py: takes an old setup, .amd file, and new setup as arguments, after which it modifies the new IIS setup to have either differential state change estimations (one in the middle of a period, or one at the start and one at the end) or empirical acceleration estimations during "small forces" (attitude corrections/thruster firings). This program takes an acc.inp file from the working directory if present, and otherwise makes one at the end of calling the program;

- calc_lighttime.py: takes a string of formatted date and time as argument after which it calculates the light-time from Titan to the Earth. This is convenient to know as this can be used in analysing the residual plots further: modifications to the IIS setups (such as empirical accelerations or differential state changes) are visible in the residuals one light-time later;
- change_sigmas.py: takes and old and new IIS input, and modifies *a priori* sigmas on estimated parameters such as empirical accelerations and observation biases (the sigmas on the RTG scale biases are hard-coded);
- compare_resids.py: takes two optional arguments as legend labels. It requests two directory paths, which should contain a "resid_ascii" file. The residual ascii files will be plotted together for comparison, and statistical values will be calculated;
- make_mbias.py: calculates observation biases for all station-satellite combinations. It takes a file 'resid_ascii', and requests the time in seconds after which a new observation bias should be calculated for certain passes of observations. For example, if 1200 s is given as input, then for any station-satellite combination, a new observation bias will be calculated if the gap between observations is larger than 1200 s;
- plot_residuals.py: takes a "resid_ascii" file from the working directory and plots all the observation residuals. In the plot, different colors indicate different DSN station-satellite combinations;
- refsys1it.py: takes an old and new IIS setup as arguments. It modifies the REFSYS card on the IIS input file to change the global and arc iterations to 1. If new data is added, this is usually done to be able to remove large/significant outliers from the observations. Otherwise, GEODYN II might not converge to a solution.
- refsys.py: takes an old and new IIS setup as arguments, modifies the REFSYS card to 'REFSYS39591'
- remove_<CARD>: several of these programs were developed, and their function is straightforward. They remove the <CARD> from the the IIS setup file. Some of these programs take two arguments (old and new IIS setup file names) and some do not take an argument. If they do not take an argument, then the file "giis.input" is taken from the current working directory and modified;
- turn_around.py: makes a so-called turnaround of the given IIS setup which is a requested user input. It re-iterates a converged GEODYN II execution to check if the previous GEODYN II run has converged to a global optimum rather than a local one. Hence, the obtained values for the estimated parameters of the previous run are the *a priori* values of the turnaround run. In the working directory, a file named "converged_par" has to be present, consisting of the converged values (last iteration) of the previous run. In the "iieout" file (output of IIE), the lines starting from "1ARC ..." up until the last value of the estimated parameters should be in the 'converged_par' file. Attention has to be paid however: this program matches the first estimated parameter to the first IIS setup card that it finds in the setup for said parameter. GEODYN IIE will not estimate an observation bias for example, if data for those observations is not present or analysed for any reason, and it will therefore not appear in the iieout file. Consequently, it will not be present in the converged_par file and this program will match the estimated parameters and IIS setup observation bias cards incorrectly. The same could happen for empirical accelerations.
- calc_state_setup.py: calculates the state at a given time and makes a file containing the EPOCHS, ELEMS and VARCOV cards. VARCOV is hard-coded, and the EPOCH and ELEMS cards depend on the given input. Required arguments for the program are begin time of the arc, end time of the arc, and path to the SPICE kernel;

A.2. Inversion software

This software is used after the arc-iterations have been performed by GEODYN II. This program performs a multi-arc weighted least squares approximation of the arc and global parameters all together. Therefore, this software needs the normal matrices from the output of GEODYN II (emat files). These emat files should be in a directory "Data". Before the analysis, these emat files have to be modified slightly, such that the first parameter labels are modified by adding a constant times a flyby factor to all these parameter labels. The flyby factor is simply an integer, ranging from 0 to 9 (10 flybys in total). All that will be performed automatically when running change_labels_arc.csh in the Data directory, explained below.

Additionally, the inputs to the inversion program are the constraints of the parameters, the weights of the arcs, and the Kaula factor. The constraints are applied to parameters based on their first label from GEODYN II. The

weights of the parameters consist of a weight given to the arc, with the path to the file of the corresponding normal matrix. Lastly, the Kaula factor (K) is a factor which multiplies 10^{-5}, such that the Kaula constraint

$$\sigma_l = \frac{K \cdot 10^{-5}}{l^2}$$

is applied to the global spherical harmonic coefficients [Kaula, 1966].

Below, several programs are described, in terms of how to use them, as well as the outputs they generate. These are mainly necessary for, or before the execution of the actual least squares analysis.

- run.solve: main program which is called to estimate the gravity coefficients, explanation of inputs and outputs can be found in the header of the program;
- solvepa-titan2: calculates the estimated parameters, given the constraints and weights of the flybys/arcs.
- emat_label: modifies the labels of the estimated arc-parameters, such that unique constraints can be applied on all arc-specific parameters. Note that this should be done before obtaining certain parameters, such as empirical accelerations with the program constraint_smallforce.py (see below). Labels are changed by adding a constant multiplied by a factor depending on the flyby number, to the first labels of all the parameters. T011 has factor 0 and T122 has factor 9, constants differ per parameter;
- change_labels_arc.csh: changes all the labels of the parameters from every arc, by calling emat_label. Does so by modifying ematrix file emat.T068 to emat.new.T068, where emat.new.T068 only contains different first labels for the arc-parameters.
- inverse_combiMod.x: takes the combined normal matrix as input, the constraint file, output file names of the inverse matrix and formal error, and the Kaula factor ($K \times 10^{-5}$). This program hence calculates the formal errors on the parameters and inverse of the normal matrices;

After obtaining the estimations for the parameters, several tools can be used to analyse the results, or obtain certain types of parameters from the estimated parameter set to constrain tighter (empirical accelerations for example). These tools are listed below.

- change_lovenumber.py: takes an old IIS setup, new Love number (k_2, max 20 characters), new gravitational constant (max 20 characters), and new IIS setup filename as inputs. It changes the Love number and gravitational parameter in the IIS setup, which is useful for performing global iterations;
- emat_correl.x: takes an input emat file and output emat file, and makes a correlation matrix from given input emat file and writes it to the output file;
- RMS_calc.py: takes a flybynr (Txxx) and a directory as input. It calculates the rms of the residuals from a "resid_ascii" file in the current working directory. It appends the flybynr, the rms and 1.0/rms to a file "RMS_list", to be able to use the fit of the residuals as a weight for the arcs/flybys. The number of observations in the resid_ascii file will be appended to a "nrObs" file. If these files do not exist in the directory yet, they will be made;
- constraint_smallforce.py: takes "arc.param" file and *a priori* sigma on the small forces. It takes the empirical accelerations belonging to a small force and constraints them according to the *a priori* sigma given. Caution should be paid, as it takes any empirical radial acceleration to be a "small force", in addition to cross- and along-track empirical accelerations during the same time period.
- mk_readable.py: takes "common.param" file containing all estimated parameters of which it makes and prints out a short summary. It makes three files:
  1. table_params: short summary of several degree two coefficients, μ, and k_2;
  2. overview_common: a more user friendly overview of the estimated parameter, containing the same information as "common.param";
  3. arc.param: file consisting of the final values of the arc-specific parameters. The final values are at the top of the file and the increments are printed beneath;

- multiplyArcWeights.py: takes an input file, containing the weights of the arcs, and a multiplication factor. It returns a 'weights.inMultiplied' file where the weights of the input file are multiplied with the multiplication factor;
- normalize_weights.py: takes an "RMS_list" file and makes a copy "RMS_listNormalized" of "RMS_list" with a normalized factor to be used as weight for the corresponding arcs, such that all arc weights add up to one;
- plot_powerspectrum.py: takes a "common.param" file as input and plots the power spectrum of the spherical harmonic coefficients. A Kaula power law of 10^{-5} is plotted for reference;
- rad_accel_labels.py: similar program to constraint_smallforce.py. Instead, this program takes all and only radial empirical accelerations. Additionally, it makes a file "radial_accel_constraints" with constraints in the right format, such that they can be implemented in the constraints file needed as input for the actual inversion program (solvepa-titan2);
- summary_arc.py: takes "arc.param" as input and prints out an extensive summary, with magnitudes of the minimum and maximum of several types of parameters (empirical accelerations, observation biases etcetera). For the state it prints the maximum and minimum adjustments;

A.3. Miscellaneous programs

Several other tools have been used and developed during the span of this thesis. These range from programs making certain files that other programs listed above need, or making the state table files necessary for interpolation of the third body moons of Saturn. Their purpose and usage is explained as well.

- modify_dvfiles.py: takes a file "all_DV_files.dv"[3], consisting of the logs of all the small forces/attitude corrections of the Cassini spacecraft, to modify and change it to a file "all.amd" with a format interpretable by several other Python programs
- rd_scbodyeph.x: reads a binary external ephemeris file and prints out a summary of the supplementary bodies in it;
- check_cassini_spk.py: plots difference in position of Cassini with respect to Titan from GEODYN and SPICE. SPICE obtained this position after having loaded an spk file consisting of the orbit of Cassini calculated by GEODYN II, hence merely verification that the spk is correctly loaded and made. In addition, this program makes a "cassini_geod_<flybynr>" file containing Cassini's state at a certain time (UTC). Paths to different files have to be changed manually.
- make_state_file_moons.py: makes state files for the moons of Saturn, necessary for the modified GEODYN IIE version, which interpolates the position. Increment is hard-coded. Output table file named <moon>.<flybynr>, and the epochs of the flybys are extended with a 2-day boundary to avoid interpolation issues. The epochs are taken from a file (path hard-coded) consisting of the concatenated EPOCH cards of the IIS setups of the flybys and should be in chronological order. Make sure the epochs order matches the list flybys hard-coded in this program;
- length_flyby.py: takes an epochs file (see make_state_file_moons.py) and prints the C/A altitude of Cassini with respect to Titan. In addition, the middle of the flyby is printed.

General comment

A general comment about all of the listed programs in this appendix: in the code, usually hard-coded paths and filenames exist. These paths and file names have to be changed to their correct names, which are user dependent, before they can be utilized. Usually, these path or file names are the epochs file or SPICE load kernel file.

[3]For the files, see `https://pds-atmospheres.nmsu.edu/data_and_services/atmospheres_data/Cassini/Cassini/DOCS%20for%20events%20&%20Configuration%20page/Small%20Forces/`

Bibliography

C. Acton, N. Bachman, B. Semenov, and E. Wrigth. A look toward the future in the handling of space science mission geometry. *Planetary and Space Science*, 2017. doi: 10.1016/j.pss.2017.02.013.

J.D. Anderson and G. Schubert. Titan's gravitational field inferred from six Cassini flybys. *American Geophysical Union*, 2013.

Andrew Annex, Ben Pearson, Benoît Seignovert, Brian T. Carcich, Helge Eichhorn, Jesse A. Mapel, Johan L. Freiherr von Forstner, Jonathan McAuliffe, Jorge Diaz del Rio, Kristin L. Berry, K.-Michael Aye, Marcel Stefko, Miguel de Val-Borro, Shankar Kulumani, Shin ya Murakami, Kyle Niemeyer, and Gavin Medley. Andrewannex/spiceypy: Spiceypy 3.1.1, May 2020. URL https://doi.org/10.5281/zenodo.3850089.

S. W. Asmar, J. W. Armstrong, L. Iess, and P. Tortora. Spacecraft Doppler tracking: Noise budget and accuracy achievable in precision radio science observations. *Radio Science*, 40(2), 2005. doi: https://doi.org/10.1029/2004RS003101. URL https://agupubs.onlinelibrary.wiley.com/doi/abs/10.1029/2004RS003101.

R.-M. Baland, T. Van Hoolst, M. Yseboodt, and Ö. Karatekin. Titan's obliquity as evidence of a subsurface ocean? *A&A*, 530:A141, 2011. doi: 10.1051/0004-6361/201116578. URL https://doi.org/10.1051/0004-6361/201116578.

M. Di Benedetto. *The Non-Gravitational Accelerations of the Cassini Spacecraft and the nature of the Pioneer anomaly*. PhD thesis, University of Rome, 2010-2011.

B. Bertotti, L. Iess, and P . Tortora. A test of general relativity using radio links with the Cassini spacecraft. *Nature*, 425:374–376, 2003.

Todd S. Brown. The Cassini reaction wheels: Drag and spin-rate trends from an aging interplanetary spacecraft at Saturn. pages 2016–2085, 2016. doi: 10.2514/6.2016-2085. URL https://arc.aiaa.org/doi/abs/10.2514/6.2016-2085.

Brent Buffington, Nathan Strange, and John Smith. *Overview of the Cassini Extended Mission Trajectory*. 2008. doi: 10.2514/6.2008-6752. URL https://arc.aiaa.org/doi/abs/10.2514/6.2008-6752.

John A. Christian. Autonomous initial orbit determination with optical observations of unknown planetary landmarks. *Journal of Spacecraft and Rockets*, 56(1):211–220, 2019. doi: 10.2514/1.A34259. URL https://doi.org/10.2514/1.A34259.

D. Durante, D.J. Hemingway, P. Racioppa, L. Iess, and D.J. Stevenson. Titan's gravity field and interior structure after Cassini. *Icarus*, 326:123–132, 2019. doi: https://doi.org/10.1016/j.icarus.2019.03.003.

Aleta Duvall, C. Justus, and Vernon Keller. *Global Reference Atmospheric Model (GRAM) Series for Aeroassist Applications*. 2005. doi: 10.2514/6.2005-1239. URL https://arc.aiaa.org/doi/abs/10.2514/6.2005-1239.

G.P. Fabiani and V. Costabile. Cassini HGA/LGA antenna: When thermal design is a project driver. *Sixth European Symposium on Space Environmental Control Systems*, 1997.

Jim Fuller, Jing Luan, and Eliot Quataert. Resonance locking as the source of rapid tidal migration in the Jupiter and Saturn moon systems. *Monthly Notices of the Royal Astronomical Society*, 458(4):3867–3879, 03 2016. ISSN 0035-8711. doi: 10.1093/mnras/stw609. URL https://doi.org/10.1093/mnras/stw609.

Michael Garland and Paul Heckbert. Surface simplification using quadric error metrics. *Proceedings of the ACM SIGGRAPH Conference on Computer Graphics*, July 1997. doi: 10.1145/258734.258849.

S. Goossens and K. Matsumoto. Lunar degree 2 potential Love number determination from satellite tracking data. *Geophysical Research Letters*, 35(2), 2008. doi: https://doi.org/10.1029/2007GL031960. URL https://agupubs.onlinelibrary.wiley.com/doi/abs/10.1029/2007GL031960.

D. Hemmingway, F. Nimmo, H. Zebker, and L. Iess. A rigid and weathered ice shell on Titan. *Nature*, 500: 550–552, 2013. doi: https://doi.org/10.1038/nature12400.

Amanda R. Hendrix, Terry A. Hurford, Laura M. Barge, Michael T. Bland, Jeff S. Bowman, William Brinckerhoff, Bonnie J. Buratti, Morgan L. Cable, Julie Castillo-Rogez, Geoffrey C. Collins, Serina Diniega, Christopher R. German, Alexander G. Hayes, Tori Hoehler, Sona Hosseini, Carly J.A. Howett, Alfred S. McEwen, Catherine D. Neish, Marc Neveu, Tom A. Nordheim, G. Wesley Patterson, D. Alex Patthoff, Cynthia Phillips, Alyssa Rhoden, Britney E. Schmidt, Kelsi N. Singer, Jason M. Soderblom, and Steven D. Vance. The NASA roadmap to ocean worlds. *Astrobiology*, 19(1):1–27, 2019. doi: 10.1089/ast.2018.1955. URL https://doi.org/10.1089/ast.2018.1955. PMID: 30346215.

L. Iess, N.J. Rappaport, R.A. Jacobson, P. Racioppa, D.J. Stevenson, P. Tortora, J.W. Armstrong, and S.W. Asmar. Gravity field, shape, and moment of inertia of Titan. *Science*, 327:1367–1369, 2010. doi: 10.1126/science.1182583.

L. Iess, R. Jacobson, M. Ducci, D. J. Stevenson, J. I. Lunine, J. W. Armstrong, S. Asmar, P. Racioppa, N. J. Rappaport, and P. Tortora. Titan's Eccentricity Tides. In *AGU Fall Meeting Abstracts*, volume 2011, pages P33F–03, December 2011.

L. Iess, R.A. Jacobson, M. Ducci, D.J. Stevenson, J.I. Lunine, J.W. Armstrong, S.W. Asmar, P. Racioppa, N.J. Rappaport, and P. Tortora. The tides of Titan. *Science*, 337(6093):457–459, 2012. doi: 10.1126/science.1219631.

Luciano Iess, Mauro Di Benedetto, Nick James, Mattia Mercolino, Lorenzo Simone, and Paolo Tortora. Astra: Interdisciplinary study on enhancement of the end-to-end accuracy for spacecraft tracking techniques. *Acta Astronautica*, 94(2):699 – 707, 2014. ISSN 0094-5765. doi: https://doi.org/10.1016/j.actaastro.2013.06.011. URL http://www.sciencedirect.com/science/article/pii/S0094576513002014.

H. M. Jara Orué. *Rotational Dynamics of Icy Satellites*. PhD thesis, Delft University of Technology, 2016.

Ian T. Jolliffe and Jofge Cadima. Principal component analysis: a review and recent developments. *Phil. Trans. R. Soc. A.*, 374, 2016. doi: http://doi.org/10.1098/rsta.2015.0202. URL https://royalsocietypublishing.org/doi/10.1098/rsta.2015.0202.

W.M. Kaula. *Theory of Satellite Geodesy*. Blaisdell Publishing Company, A, 1966. Waltham, MA, US.

David C. Lay. *Linear Algebra and Its Applications*. Addison-Wesley, fourth edition edition, 2012. University of Maryland-College Park.

J.-P. Lebreton and D.L. Matson. An overview of the Cassini mission. *Il Nuovo Cimento*, 15(6), July 1992. doi: 10.1145/258734.258849.

Frank G. R. Lemoine, David E. Smith, Maria T. Zuber, Gregory A. Neumann, and David D. Rowlands. A 70th degree lunar gravity model (glgm-2) from clementine and other tracking data. *Journal of Geophysical Research: Planets*, 102(E7):16339–16359, 1997. doi: https://doi.org/10.1029/97JE01418. URL https://agupubs.onlinelibrary.wiley.com/doi/abs/10.1029/97JE01418.

Muzi Li, Bo Xu, and Lei Zhang. Orbit determination for remote-sensing satellites using only optical imagery. *International Journal of Remote Sensing*, 38(5):1350–1364, 2017. doi: 10.1080/01431161.2017.1280626. URL https://doi.org/10.1080/01431161.2017.1280626.

E.I. Lin, J.W. Stultz, and R.T. Reeve. Test-derived effective emittance for Cassini MLI blankets and heat loss characteristics in the vicinity of seams. *San Diego, CA*, 1995.

F.L. Markley. Autonomous navigation using landmark and intersatellite data. *Research laboratory Washington DC*, 1987.

E. Mazarico, A. Genova, S. Goossens, F.G. Lemoine, G.A. Neumann, M.T. Zuber, D.E. Smith, and S.C. Solomon. The gravity field, orientation, and ephemeris of Mercury from MESSENGER observations after three years in orbit. *Journal of Geophysical Research: Planets*, 119:2417–2436, 2014. doi: 10.1002/2014JE004675.

E.M.A. Mazarico. *Precise Orbit Determination of the Mars Odyssey spacecraft and geodetic inversion for the Martian gravity field*. PhD thesis, Massachusetts Institute of Technology, 2004.

J.J. McCarthy, S. Rowton, D. Moore, D.E. Pavlis, S.B. Luthcke, and L.S. Tsaoussi. *GEODYN II System Description Volume 1*. NASA GSFC, February 2015.

J. McMahon, D.J. Scheeres, D. Farnocchia, and S. Chesley. Understanding Kaula's rule for small bodies. *American Geophysical Union*, 2015.

NASA. Cassini 3d model, 2019. URL https://solarsystem.nasa.gov/resources/2401/cassini-3d-model/.

D.E. Pavlis, S.G. Poulose, and J.J. McCarthy. GEODYN II operations manual. *SGT Inc.*, 2006. Greenbelt, MD, USA.

F. Pedregosa, G. Varoquaux, A. Gramfort, V. Michel, B. Thirion, O. Grisel, M. Blondel, P. Prettenhofer, R. Weiss, V. Dubourg, J. Vanderplas, A. Passos, D. Cournapeau, M. Brucher, M. Perrot, and E. Duchesnay. Scikit-learn: Machine learning in Python. *Journal of Machine Learning Research*, 12:2825–2830, 2011.

Viktor Vasil'evich Prasolov and Yuri Pavlovich Solovyev. *Elliptic functions and elliptic integrals*, volume 170. American Mathematical Soc., 1997.

Anna Franziska Pukhauser. On the use of Doppler measurements for dynamic orbit computation. case study: GRAIL. Master's thesis, Graz University of Technology, 2015.

Nicole J. Rappaport, Luciano Iess, John Wahr, Jonathan I. Lunine, J.W. Armstrong, Sami W. Asmar, Paolo Tortora, Mauro Di Benedetto, and Paolo Racioppa. Can Cassini detect a subsurface ocean in Titan from gravity measurements? *Icarus*, 194(2):711 – 720, 2008. ISSN 0019-1035. doi: https://doi.org/10.1016/j.icarus.2007.11.024. URL http://www.sciencedirect.com/science/article/pii/S0019103507005532.

François Raulin and Tobias Owen. *Organic Chemistry and Exobiology on Titan*, pages 377–394. Springer Netherlands, Dordrecht, 2003. ISBN 978-94-017-3251-2. doi: 10.1007/978-94-017-3251-2_10. URL https://doi.org/10.1007/978-94-017-3251-2_10.

R. Sabadini and B. Vermeersen. *Global Dynamics of the Earth*. Springer, 2nd edition, 2016.

Shai Shalev-Shwartz and Shai Ben-David. *Understanding Machine Learning*. Cambridge University Press, 2014. University of Cambridge.

Sheldahl: A Multek Brand. Aluminum coated (two sides) polyimide, 2020. URL https://www.sheldahl.com/sites/default/files/2017-09/MLI%20Blankets.pdf. Sheldahl, Northfield, MI, USA.

F. Sohl, H. Hussmann, B. Schwentker, and T. Spohn. Interior structure models and tidal Love numbers of Titan. *Journal of geophysical research*, 108(E12, 5130), 2003. doi: 10.1029/2003JE002044.

B.D. Tapley, B.E. Schutz, and G.H. Born. *Statistical Orbit Determination*. Elsevier, 2004.

Catherine L Thornton and James S Border. *Radiometric tracking techniques for deep-space navigation*. John Wiley & Sons, 2003.

R.H. Tyler. Tidal dynamical considerations constrain the state of an ocean on Enceladus. *Icarus*, 211:770–779, 2011. doi: 10.1016/j.icarus.2010.10.007.

X. Yue and J. Yuan. Gps based reduced-dynamic orbit determination for low earth orbiters with ambiguity fixing. *Hindawi*, 2015, 2015. doi: https://doi.org/10.1155/2015/723414.

Qian-Yi Zhou, Jaesik Park, and Vladlen Koltun. Open3D: A modern library for 3D data processing. *arXiv:1801.09847*, 2018.